ASSESSMENT OF TI-6AL-4V LASER CLAD REPAIR

by

Paul Gardner

A Thesis

Submitted to the Faculty of Purdue University

In Partial Fulfillment of the Requirements for the degree of

Master of Science in Aeronautics and Astronautics

School of Aeronautics and Astronautics

West Lafayette, Indiana

May 2022

THE PURDUE UNIVERSITY GRADUATE SCHOOL
STATEMENT OF COMMITTEE APPROVAL

Dr. Michael Sangid, Chair

School of Aeronautics and Astronautics

Dr. Alten Grandt

School of Aeronautics and Astronautics

Dr. Tyler N. Tallman

School of Aeronautics and Astronautics

Approved by:

Dr. Gregory A. Blaisdell

ACKNOWLEDGMENTS

The successful undertaking of a Masters research program would not be possible without the guidance and support of many. I wish to pass on my thanks to Dr Michael Sangid for his guidance and direction during this period. The lessons I have learned from my time around Dr Sangid and other members from the Advanced Computational Materials and Experimental Evaluation ($ACME^2$) laboratory will remain with me for the rest of my career. Many thanks also go to Dr Kevin Walker, from the Australian Defence Science and Technology Organisation for his invaluable guidance, feedback and support for this project. A special thanks to Dr Jun-Sang Park for his efforts conducting experiments at the Advanced Photon Source (APS), Argonne National Laboratory and guidance in interpretation of this experimental data. Use of the Advanced Photon Source was supported by the US Department of Energy, Office of Science, Office of Basic Energy Sciences, under contract No. DE-AC02-06CH11357. Members of the $ACME^2$ laboratory, Dr Ritwik Bandyopadhyay and Priya Ravi, were instrumental in supporting the processing of synchrotron data that is utilised within this research. Thank you to Yi-Rye Choi, Royal Melbourne Institute of Technology, for her aid in the manufacture of of these specimens and for Dr. Igor Switala who worked tirelessly with Dr Kevin Walker to quickly modify the specimens and send them back to the $ACME^2$ laboratory. My thanks also goes to Dr. Simon Barter for his advice on fatigue crack growth and marker band techniques. Special thanks should go to the Royal Australian Air Force for funding this endeavour, and to the Defence Aviation Safety Authority for providing funding for this research. Thank you to Dr Alten Grandt and Dr Tyler Tallman for their support and role as my committee members alongside Dr Sangid. Finally, to Amy Syme-Ross, for her continued love and support.

TABLE OF CONTENTS

LIST OF TABLES 7

LIST OF FIGURES 8

ABSTRACT 10

1 INTRODUCTION 12

1.1 Need for Additive Manufacturing 12

1.1.1 Capability Requirements 12

1.1.2 Ageing Aircraft 12

1.1.3 Supply 13

1.1.4 Additive Manufacturing and Applications 14

1.1.5 Certification Requirements 15

1.2 Aim and Research Questions 17

1.3 Thesis Overview 17

2 LITERATURE REVIEW 19

2.1 Laser Cladding 19

2.1.1 Titanium 19

2.1.2 Laser Cladding Benefits 19

2.1.3 Laser Cladding 20

2.1.4 Effect of Clad Parameters on Microstructure 21

2.1.5 Laser Clad Challenges 22

2.1.6 Previous Work 23

2.2 Residual Stress 23

2.2.1 Nature of Residual Stress 23

2.2.2 X-ray Diffraction 25

Measurement of Lattice Strain 26

Measurement of Stress from Lattice Strain 27

2.2.3 Slitting 27

2.2.4 Contour Method . . . 28
2.2.5 Comparison and Application of Methods . . . 28
2.3 Fatigue Crack Growth . . . 32
2.4 Marker Band Technique and Ti-6Al-4V Fractography . . . 37
2.4.1 Quantitative Fractography . . . 37
2.4.2 Automated Quantitative Fractography . . . 39

3 SPECIMEN DESIGN . . . 41
3.1 Specimen Configurations . . . 41
3.2 Laser Clad . . . 46
3.3 Notches . . . 48
3.4 Heat Treatment . . . 49

4 RESIDUAL STRESS . . . 53
4.1 X-ray Diffraction . . . 53
4.1.1 Background and Objectives . . . 53
4.1.2 Experiment Setup . . . 55
4.1.3 Post-experiment Analysis . . . 56
4.1.4 Lattice Strain Calculations . . . 61
4.2 Slitting . . . 64
4.2.1 Experiment Setup . . . 64
4.2.2 Slitting Results . . . 65

5 FATIGUE TESTING . . . 67
5.1 Experimental Setup . . . 67
5.2 Specimen Design Revisions . . . 71
5.3 Fatigue Testing Results . . . 74

6 FRACTOGRAPHY . . . 77
6.1 Equipment . . . 77
6.2 Fractography Surface Features . . . 79
6.3 Marker Band Technique . . . 83

6.4 Fractography Results 85

7 DISCUSSION 88

8 RECOMMENDATIONS 95

REFERENCES 97

LIST OF TABLES

3.1 Specimen configuration 42

3.2 Laser clad parameters 48

4.1 Description of Ti-6AL-4V alpha peaks 60

5.1 Fatigue test equipment 67

5.2 Baseline specimen loading sequence 69

5.3 Clad repaired specimen loading sequence 69

6.1 SEM equipment settings 79

LIST OF FIGURES

2.1 Measurement penetration vs. spatial resolution for various residual stress measurement methods [29] . . . 24

2.2 Diffraction of x-rays by planes of atoms [33] . . . 26

2.3 The incremental slitting method for measuring residual stress [36] . . . 28

2.4 Comparison of residual stress results within specimen depth [29] . . . 29

2.5 Neutron diffraction residual stress results for as-clad and as-clad PHT [28] . . . 30

2.6 Residual stress cross section map measured using contour method for LMD-1 and LMD-2 [10] . . . 31

2.7 Inconsistent lattice strains for EDD application [40] . . . 32

2.8 Behavior of fatigue crack growth rate [44] . . . 33

2.9 Fracture surface comparison between aluminum and titanium [52] . . . 38

2.10 Ti-6Al-4V Marker band measurement [40] . . . 39

3.1 Specimen design 1 . . . 43

3.2 Specimen design 3 . . . 44

3.3 Specimen design 3.1 . . . 45

3.4 Specimen design 3.2 . . . 47

3.5 Deposition pattern [40] . . . 48

3.6 Deposition pattern . . . 50

3.7 Original notch [40] . . . 51

3.8 Specimen design 3.1 notches . . . 51

3.9 Specimen design 3.2 notches . . . 52

4.1 XRD method . . . 54

4.2 XRD scan method . . . 55

4.3 Intensity from As-clad specimen . . . 57

4.4 Sample Ti-6AL-4V lineout . . . 58

4.5 Ti-6AL-4V lineout featuring peak ID . . . 59

4.6 Residual example from As-clad specimen . . . 61

4.7 Lattice strain for As-clad specimen . . . 62

4.8 Lattice strain for PHT specimen . . . 63

4.9 Slitting orientation 64
4.10 Slitting results 66
5.1 Example marker band loading sequence [40] 68
5.2 MPE software for clad specimens 71
5.3 Camera configuration with 10x optical lens 72
5.4 Failure of design 3.1 73
5.5 Failure of design 3.2 73
5.6 7B baseline crack progression 75
5.7 Fatigue comparison of baseline, As-clad and PHT samples 76
6.1 Optical microscope with a short focal length 78
6.2 (a) live optical image (b) 100 images stacked [40] 78
6.3 Fractography orientation 80
6.4 Clad, HAZ and substrate regions [40] 81
6.5 Fracture surface features 82
6.6 Marker band features 84
6.7 Surface semi-elliptical crack 85
7.1 da/dN vs Δ K and MMPDS comparison 89
7.2 Residual stress and desired crack growth direction overlaid on the fracture surface 93
7.3 da/dN vs Δ Keff with residual stress 94

ABSTRACT

Damaged components and a lack of spare components are issues which are currently affecting military aircraft capability. Laser Cladding is an additive manufacturing technique which shows promise in repairing damaged aviation components. However, there are considerable certification requirements for critical components which stand to gain the most benefits from laser clad repair methodologies. These requirements involve establishing crack growth rate data for the laser clad material to gain confidence in the reliability of the repair's performance on in-service aircraft. This research seeks to understand the fatigue behavior of Ti-6Al-4V that has undergone a simulated laser clad repair, with unrepaired specimens also tested to allow for comparison. Half of the clad repaired specimens were subjected to a heat treatment process with the intention of relaxing the residual stress within the clad repair and underlying substrate. Firstly, the residual stress was measured utilising the non-destructive High Energy X-ray Diffraction (HEXD) and destructive slitting techniques. Whilst the HEXD method was able to successfully identify lattice strain within the material, a significant amount of scatter was present in the results. The slitting method was able to quantify the residual stress within each clad repair category, however this method is unable to identify the entire residual stress field within the material. Fatigue testing was conducted on the samples with significant challenges experienced in initiating crack growth within the area of interest, which required specimen redesigns. Quantitative fractography was next conducted on the failed fracture surfaces, with the marker band technique utilized to determine fatigue crack growth rate. Marker band detection was challenging, with only a small number of specimens exhibiting observable marker bands due to the tortuous nature of the Ti-6Al-4V fracture surfaces. The baseline material correlated well to reference Ti-6Al-4V material data from the Metallic Materials Properties Development and Standardization database. Both of the laser clad repairs experienced faster fatigue crack growth rate in comparison to the baseline case, which was attributed to the microstructural changes due to the clad process. The application of heat treatment improved the repair performance; however heat treatment may not be available for all aircraft repair applications. Whilst this research presents material data that would assist in establishing a damage tolerance methodology for

laser clad repaired materials, a significant amount of data is required to enable any successful certification for application to in-service aircraft.

1. INTRODUCTION

1.1 Need for Additive Manufacturing

1.1.1 Capability Requirements

Military aviation seeks to utilize aircraft as a means to provide capability to military commanders as a projection of national airpower in support of government objectives [1]. A fundamental requirement for this projection of national air power is the generation and sustainment of serviceable aircraft for flying operations. With the exception of extreme circumstances, whenever an aircraft or associated critical mission system is defective or unserviceable, the aircraft is unable to carry out these flying operations.

Each military aircraft fleet requires a certain amount of serviceable aircraft to meet military capability requirements. These performance requirements can vary depending on the aircraft role, age and operator. Meeting this performance requirement can be extremely challenging. A recent U.S Government Accountability Office (GAO) report identified that 24 of 46 types of U.S military aircraft did not meet their annual serviceability performance requirements from 2011 to 2019 [2]. Additionally, during the 2019 fiscal year only three of these 46 aircraft met the required mission capable goals. The reasons for this poor performance include ageing aircraft, issues with supply of aircraft components and aircraft maintenance challenges.

1.1.2 Ageing Aircraft

Ageing aircraft can be considered as an aircraft that has reached or exceeded its design life in flying hours or calendar years which can experience widespread fatigue or corrosion damage [3]. The implications of this milestone in the aircraft's lifecycle feature a significant increase in cost and other resources that are required to maintain the aircraft at the required levels of safety for safe flight.

Aircraft repairs are conducted when a component or structure is beyond pre-determined wear or crack limits. When these limits are reached, the aircraft is declared unserviceable and is no longer available for flight operations. The repair can be deferred for a short period of

time which requires approval from the engineering organization responsible for the aircraft's safety.

The large cost and resource requirements to maintain an ageing aircraft are due to increased wear and degradation of aircraft structural components. This leads to a greater number of aircraft structural repairs that are required to maintain the aircraft serviceability. The compounding effects of this age are due to increasing fatigue damage to the aircraft structure and increasing the scope of inspections required to ensure the aircraft is capable of safe flight. Within the ageing aircraft category listed in the GAO report, the unexpected replacement of parts or repair requirements are by far the most common listed amongst U.S military aircraft. This trend is concerning, as modern aircraft designs feature light-weight components with tighter design tolerances then previous generations, particularly with critical aircraft structure. This means there is less material for common blended repair methods. The use of Additive Manufacturing (AM) for the repair of critical structural components, including high strength steel and titanium, allows for a reduction of repair completion times and quicker re-introduction of a component back into service, improving the serviceability rate of the aircraft fleet.

1.1.3 Supply

Aircraft procurement does not simply end with the airframe itself. Support equipment, simulators, tools and logistics systems are required to be established at acquisition in support of aircraft operations. There is a significant cost impact of both storing and transporting components for operational use [4]. Despite this large cost, parts shortages and delays are listed amongst the most common reason for supply challenges contributing to poor aircraft serviceability rates [2]. New military aircraft from smaller nations, like the Royal Australian Air Force (RAAF), are sustained through a global supply chain, which means they may not have component locally available. This is especially apparent with components that are not regularly replaced such as engines and primary structure. Replacement parts can take time to arrive, particularly if sourced or manufactured in different countries. However, the repair

of damaged components can allow them to re-enter the spares pool or allow installation onto other affected aircraft, increasing the spares pool and increasing aircraft availability [5].

1.1.4 Additive Manufacturing and Applications

There are many opportunities that AM can provide to improve military aircraft capability. The AM process features the building or repair of a component through additive layers instead of subtractive manufacturing or repair methods [6][7]. In this manner, AM offers two benefits to military aircraft applications, the fabrication of replacement components and repair of in-service components.

AM has been used in multiple applications across all aircraft types. A simple fabrication application features the manufacture of an E-3 leading edge bleed air duct bracket by a U.S. military maintenance facility. A lack of replacement components across the entire fleet was initially solved with a local manufacture featuring conventional methods. However, this was costly in terms of manpower, with a significant effect on unit morale. Utilization of AM for the manufactured brackets reduced the manpower cost significantly whilst allowing the unit to not only meet their component replacement needs, but to also gain a surplus of available components [8].

The application of a cold spray repair, Supersonic Particle Deposition (SPD) has been utilized as a corrosion repair method for Royal Australian Navy (RAN) Seahawk helicopter gearboxes [9]. These repairs prevented the gearboxes from being scrapped or entering a lengthy repair process in the U.S. The application of this repair provided significant cost saving measures to the operator and enhanced the RAN helicopter capability.

Finally, the application of a laser clad repair is starting to see use on military aircraft, which offers both geometrical and structural restoration for repair applications due to a thicker deposition layer [10]. An example of this application features a laser clad repair applied to a tailhook of a RAAF F/A-18 fighter aircraft to restore worn material [11].

Due to the significant amount of materials qualification required to assure AM materials for critical structural repairs, the majority of AM component fabrication and repair use, as identified above, has occurred on non-critical components. This is due to the low consequence

of their failure, as the aircraft and personnel would not be lost by non-critical component failure. Additionally, AM component substitution or repair for non-critical components would also not require regulator oversight and approval, allowing the process to occur in a shorter time frame. This is done to gain the benefits of AM repair and allows an evaluation of repair performance in the field without significantly affecting the safety of personnel or the aircraft. It stands to reason that the capability and cost savings for AM applications would be greater for critical structures due to their high cost and limited supply. However, certification requirements for aircraft critical structures are much more stringent than other components where failure would not produce catastrophic consequences for the aircraft and its crew.

1.1.5 Certification Requirements

There are many requirements that need to be addressed before the progression of a structural material or process is applied to regular use on operational aircraft. The Lincoln criteria have been used as a model to transfer technology from laboratory environments to in-service applications [12]. Due to the nature of AM repairs on aircraft critical structure, the design and certification of these repairs can utilize this model.

Characterized material properties are identified as the most difficult to undertake to identify the material requirements. These properties include strength, fracture toughness, dimensional stability due to creep, and crack growth rate [12]. Whilst coupon tests are an important part of identifying these properties, it is also recognized that assembly level tests will also be required. This is particularly applicable for repair applications where the AM material will influence the material, for example the introduction of residual stress.

The predictability of structural performance is an important requirement due to the high cost of full scale fatigue test, both at the assembly and aircraft level. The ability to accurately predict structural performance to a defined level of confidence allows for the application of component and sub-component tests instead of multiple full-scale fatigue tests. This has significant implications for the aircraft sustainment costs. The ability to accurately predict the flight hours or cycles to failure for a known aircraft loading will reduce the required repair

qualification requirements, reducing the time required to repair the aircraft. By reducing the time the aircraft is unserviceable, the military capability of the aircraft is improved.

No aircraft material is in perfect condition; structural failures occur through manufacturing defects or damage that is incurred in the service life of the aircraft [13]. Due to these factors, another requirement for the repair of critical structure is to ensure the repair meets damage tolerant design requirements. Damage Tolerance is the ability of a structural component to resist failure through crack growth and fracture due to preexisting cracks [13]. Damage tolerant materials are certified with specific inspection intervals to detect the presence of cracks throughout the service life of the component. Any AM repair to these components must be able to meet the same requirements, even if the repaired life may be smaller than the original final design life for the component [14]. These requirements must be understood before AM repairs can be applied and certified to military aircraft.

To provide context on the application of these principles to the repair certification process, a recent Structures Bulletin has outlined the United States Air Force (USAF) requirements for the Durability and Damage Tolerance (DADT) certification for AM fabrication and repair [15]. Whilst the application of the Lincoln criteria would allow for successful laser clad repairs, certification methods will dictate how aircraft operators will manage the application of these repairs to in-service aircraft. This paper recognizes that the biggest challenge for the fabrication and repair of AM materials is to establish an accurate prediction of structural performance, as mentioned by Lincoln criteria [12]. The USAF requires validated crack growth analysis utilizing linear-elastic fracture mechanics (LEFM) principles for the certification of aircraft critical structural component fabrication and repair [15].

A validated DADT assessment method is required which can demonstrate alignment between test results and crack growth rate predictions. Additionally, the model will be required to account for significant factors such as complex geometries and the presence of residual stresses [15]. The development of AM material data will support this method. Whilst the utilization of coupon tests to develop crack growth rate data is common in metallic materials, additional data relevant to AM is required such as the build process, component geometry and the thermal effects of the build process [15].

Ageing aircraft, a lack of replacement components and unscheduled maintenance have a detrimental effect on on aircraft capability. AM repairs, specifically laser clad repairs, feature properties which allows it to have the potential to mitigate this effect on military aircraft. However, as detailed above, more sources of data for this method are required including developing crack growth data for varying stress ratios whilst also considering the influence of residual stress to enable certification of AM repairs to aircraft critical structure. Therefore, this research will focus on furthering the body of knowledge of damage tolerant behavior of the laser clad AM method for the application of aircraft repairs. More effective and varied repair methodologies allow military operators to also improve aircraft capability and also reduce aircraft cost of ownership.

1.2 Aim and Research Questions

This research intends to contribute to the damage tolerant effects of laser clad repairs on Ti-6Al-4V aircraft structures. This is achieved through:

- Analysis of the residual stress fields between a laser clad repair, a heat treated laser clad repair, and a baseline sample of Ti-6AL-4V
- Assessment of the damage tolerant behavior of the three aforementioned samples via marker band analysis during fatigue crack growth testing
- Contextualize the effectiveness of laser cladding, based on the residual stress fields, underlying microstrucutre, and spatial fatigue crack growth rates

1.3 Thesis Overview

This thesis contains 8 sections. Section 2 contains a review of the current literature that is applicable to this research topic and provides an overview of any relevant work that has previously been conducted. Section 3 details the manufacturing process and specification details on the Ti-6Al-4V specimens used in this research, in addition to any changes made to the specimen specification throughout this research. Section 4 contains the X-ray Synchrotron and Slitting methods used to identify and characterize specimen residual stress,

with the outcomes and comparisons of these methods allowing a comparison between clad repair specimens and clad repair specimens that have undergone a heat treatment process. Section 5 contains the results of the fatigue testing carried out on the specimens and compares the fatigue characteristics of clad repaired specimens and heat treated clad repaired specimens. Section 6 provides additional details on specimen fractography used to inform crack initiation and growth rate. Section 7 provides a discussion around the results and outcomes provided in this research with recommendations detailed in section 8.

2. LITERATURE REVIEW

2.1 Laser Cladding

2.1.1 Titanium

Titanium has numerous properties that make it well suited for aerospace applications, including aircraft primary structure. These properties include high strength, low density, creep resistance up to 550°C and excellent corrosion resistance [5][16][17]. Due to its high cost, it is only used in specific applications where its high strength benefits warrant the cost, with alloys such as Ti-6Al-4V regularly used in this application. Less common titanium alloys are usually selected only when their differing properties dictate their selection. Selection criteria for titanium alloys in high strength applications include yield or ultimate strength, fatigue crack growth rate and fracture toughness [17].

The titanium alloy Ti-6Al-4V is widely used in aerospace applications [5][16][17][18][19] [20] and therefore will be the focus for this literature review. Ti-6Al-4V is a $\alpha+\beta$ Titanium alloy that features the high strength material properties of titanium with an ease of workability, allowing for diverse fabrication and casting methods [17] for use in aerospace and other high-strength applications.

Due to the critical nature of aircraft primary structures and high material costs, the application of effective repair methods can restore damaged aircraft primary structure to service, preserving the aircraft capability and reducing aircraft cost of ownership.

2.1.2 Laser Cladding Benefits

Laser cladding as an Additive Manufacturing method offers desirable properties for an application to the repair of high strength components. The use of the high powered laser allows for a lower input of heat into the material and for lower thermal damage to substrate material that is undergoing the repair [21][22]. The laser also provides a stable and consistent energy output which allows for better consistency in the clad deposition onto the underlying component. This consistency in characterized material properties of structural materials is critical in certifying this technology as suitable for in-service applications [12]. Additionally,

this deposition method allows for a build-up of material layers directly onto the surface of the component which is a desirable property for repair or corrosion prevention applications [23]. Finally, the clad parameters have been demonstrated to have an effect on the grain structure and material properties of the clad repair [24]. Continuing research to demonstrate the ability to predict material behavior through clad parameters will allow the laser clad method to be certified for use as a repair method in cases where component replacement is not immediately available or the component is non-repairable by other means.

2.1.3 Laser Cladding

Laser cladding features powder melted by a high-powered laser to deposit the melted material on the component surface through a pre-designed deposition pattern [7][21][23] [25][26][27]. As the deposited metal cools along with the immediate lower layer of material, solidification occurs through repeated layers of the clad, with the laser process parameters influencing the repair characteristics including microstructure, surface finish, porosity and the presence of residual stress in the material [27]. This heat loss through the solidification process of the melted material experiences a high cooling rate, with the creation of a metallic bond between the the clad and substrate material [21][24] through creation of Heat Affected Zone (HAZ). This HAZ created in the melted pool bonds the substrate to clad [22] through the repeated deposition layers of melted material. Furthermore, this solidification process also partially melts clad layers already deposited on the substrate, with the cooling cycle within the clad layers creating a thermal gradient between the melt pool, cooling the clad layers and the colder substrate[25].

Selection of the clad material to pair with the substrate is critical for an effective repair which can maintain its structural integrity over a predicted service life. Large differences in physical properties, for example melting point and thermal expansion, can induce undesirable residual stresses within material. Compatibility of physical properties between these two is important to reduce residual stress [24]. Using the same material for the clad, in addition to influencing the clad mechanical properties to be as close to the substrate as possible, can be beneficial for repair certification [22][25]. However, the microstructure of the clad will

be different to the substrate as the grain morphology of laser clad Ti-6Al-4V is different to conventionally manufactured Ti-6Al-4V[25].

2.1.4 Effect of Clad Parameters on Microstructure

In order for laser clad repairs to be certified for use in aircraft high strength applications, the parameters influencing the material's microstructure must be known and established to a reliable degree, to ensure predictable material behavior of the clad repair. Laser cladding parameters include laser traverse or scan speed, laser power, laser spot size, laser profile, powder feed rate, deposition pattern and the size and shape of the deposit [5][24][27]. The cooling of the molten pool of the deposited material occurs through into the substrate, with the remaining heat lost through the atmosphere.

The grain morphology, size and texture of clad Ti-6Al-4V is predominantly controlled through the local thermal conditions at the start of the solidification process, with the post-solidification cooling rate controlling the fine-scale microstructure [25][26]. The microstructure of the deposited material forms columnar shaped grains, with their direction of growth based on the build direction during the clad process[27]. Ti-6Al-4V forms a β (BCC) phase in the initial phase of solidification [5][25] with the formation of martensite α structures during cooling. With the high cooling rate these microstructures feature small equiaxed α particles.

The laser clad parameters affecting the solidification process include laser power, laser spot shape and laser traverse speed. Research was able to determine the effect of laser clad parameters on the clad, HAZ and substrate microstructure [20][25][27]. The high cooling rate of the deposition process influences the directional growth of the grains counter to the cooling direction, leading to the development of columnar grains as the material cools. This process continues as additional layers are deposited on the material surface. A high laser power was also associated with a coarser microstructure increasing the width of the α and β laths, however an increase in laser scan speed decreases the grain size with a decrease in the α and β laths. This is due to a reduced energy density input into the substrate which leads to a more rapid cooling rate in the clad HAZ and substrate regions. Microstructure changes

during post-solidification in the HAZ can be different to the clad region, with a decrease in lath thickness in the HAZ caused by a slower laser scan speed [5].

Studies into the effects of these microstructure changes on material properties have focused on yield strength, ductility and hardness [20][25]. An increase in yield strength is observed with increasing numbers of grains, with this trend ceasing at the number of ten α phase colonies in the material for every β phase. However, changes in lamellar width did not appear to affect the material yield strength. Influences on ductility were observed to be similar to yield strength, with an increase in the number of grains increasing the ductility of the clad. Additionally, changes in the α and β lamellar structure had minimal impact on ductility.

Through control of laser clad parameters to influence clad and HAZ microstructure, similar material properties to the substrate can be achieved to reduce tensile residual stresses throughout the laser repair.

2.1.5 Laser Clad Challenges

Whilst the benefits of laser clad repairs are substantial, there are several challenges to be overcome before widespread use in high strength applications. The technology cannot yet demonstrate consistent material properties and established fatigue behavior for clad repairs has not yet been developed to allow certification of critical structure [7][23]. Additionally, the use of laser clad as a repair technology will not be a direct substitute for the parent material and will incur other defects which will require management throughout the life of the repair. Tensile residual stress are induced into the material due to solidification during clad deposition [7][22] can lead to cracking during the clad repair process or during the service life of the repair. Additionally, defects introduced during the clad deposition process can reduce fatigue life of repair by acting as locations for crack nucleation, therefore acting as a stress concentration [10]. Due to these factors, the service life of the repair is likely to be less than the previous component remaining life. Additionally, the frequency of component inspections will likely be higher post-repair. However, in cases where parts aren't available,

a future certified laser cladding repair can be used to return the aircraft to a serviceable state as identified in chapter 1.

2.1.6 Previous Work

Due to the benefits of laser clad repairs, research has been conducted to evaluate the feasibility of clad repairs on test specimens for residual stress or fatigue testing. A successful feasibility study utilized a milled groove simulating damage within a parent material with a CrNi-Steel laser clad deposition as an applied repair method [21]. The deposition strategy was able to effectively fill the machine groove within the material. Further studies evaluated the fatigue performance of High Strength steel with an application of an Aermet 100 clad repair onto a machined notch simulating damage [28]. Crack growth behavior of clad AerMet 100 was found to be comparable with conventional Aermet 100 material. Additionally, underlying residual stresses within the repair provided a benefit in reducing crack growth rate. Similar research was conducted to evaluate the influence of varying Ti-6Al-4V clad repair deposition strategies on fatigue life [10], however there were difficulties in evaluating the reduced fatigue life between the designed deposition strategies due to the presence of defects within the clad region, in addition to differing residual stresses and microstructure within the material.

2.2 Residual Stress

2.2.1 Nature of Residual Stress

Residual Stresses remain within structures and materials and are independent of applied load, meaning the applied loads have been removed [29][30]. Residual stress are non-uniform with large gradients, as they are non-zero but do not have a force resultant [29]. The presence of high residual stresses can lead to material distortion and the formation of cracks within the material [19]. Residual stresses can also combine with applied in-service loading to cause structural failure below normal predicted loads [30]. However, residual stresses near the material surface can also provide benefits by providing an optimal stress distribution within a material to counter known in-service loading, extending the fatigue life of the component

[31]. This is achieved through inhibiting crack initiation and through changing the direction of crack growth below the material surface [32]. The nature of residual stresses means they are hard to quantify post-manufacture and within the material's service life. The normal stress evaluation practices of comparing the difference between applied loads and unloaded specimen cannot be used for identifying and quantifying the residual stress [29]. There are numerous different methods to measure residual stress within a specimen, as seen in figure 2.1. These methods include the use of non-destructive and destructive methods which vary in complexity, application and cost.

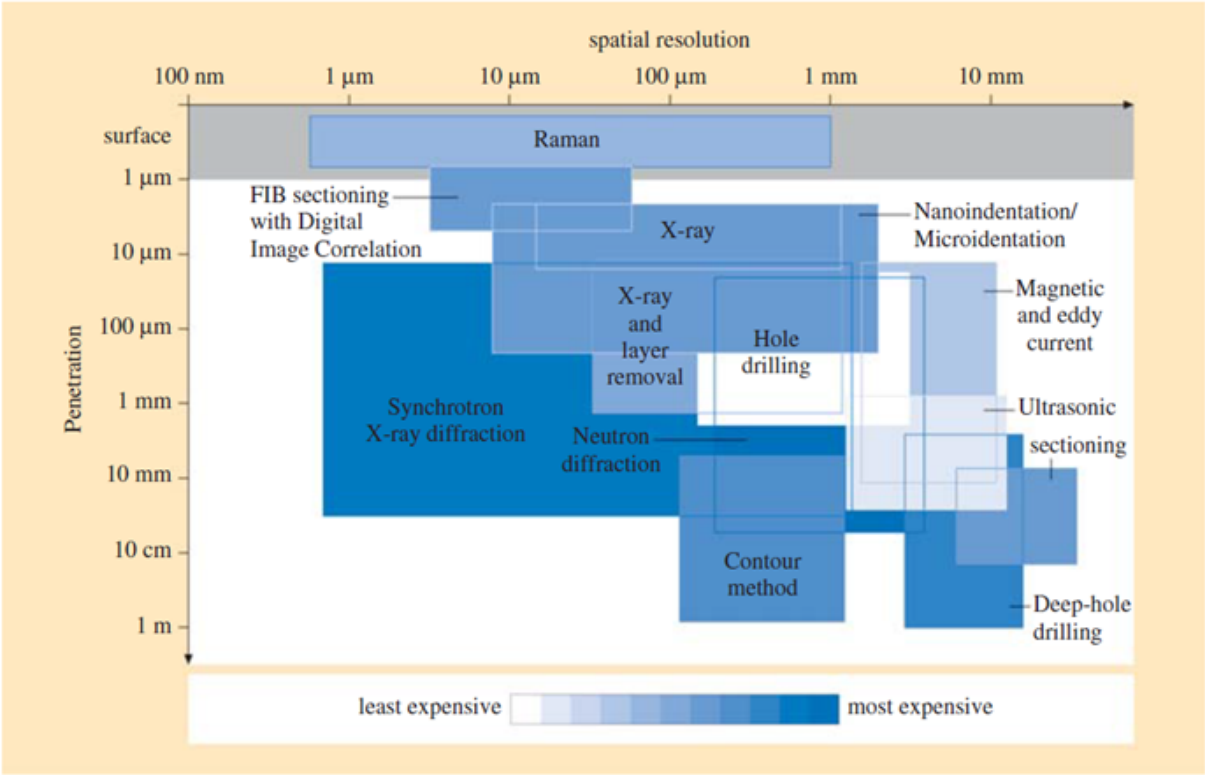

Figure 2.1. Measurement penetration vs. spatial resolution for various residual stress measurement methods [29]

Slitting is a simple and inexpensive option to destructively test residual stress in one direction. Contouring provides more information about the residual stress field within the specimen but is more complex than slitting. Notably, destructive methods such as contouring and sitting are overall cheaper and require only a simple analysis. Due to their destructive

nature, these methods would not be used to test actual repairs. However, they can be used to test repaired material coupons or representative repaired components to evaluate the suitability of repair against certification requirements.

Multiple X-ray diffraction techniques exist to provide non-destructive measurement of residual stresses. X-rays can be used to penetrate within the material and analyze residual stress, however conventional X-rays are limited in their depth of penetration into the material. High-powered Synchrotron X-rays and Neutron diffraction methods are more expensive than conventional X-ray diffraction methods, but allow higher accuracy and further penetration within the specimen. The analysis required in X-ray diffraction methods are more complex than destructive methods such as slitting and contouring.

2.2.2 X-ray Diffraction

X-ray Diffraction is a common non-destructive method to determine crystal lattice strain and associated residual stress within crystalline structures. This is achieved by using the the ability of X-rays to measure the distance between atomic planes in crystalline materials through diffraction of the X-rays within the crystalline structure, as seen in figure 2.2. The distance between crystal lattices, d_{hkl}, can be determined through the use of Bragg's Law as constructive interference will only occur when this law is satisfied:

$$n\lambda = 2d_{hkl}\sin\theta \tag{2.1}$$

where n is an integer, λ is the X-ray wavelength, d is the d_{hkl} distance between the atomic planes and θ is the Bragg angle [29]. Miller indices (h,k,l) are utilized to identify the parallel and stacked planes of atoms. Through identification of the diffraction peaks that are observed when Bragg's Law is satisfied information about the crystal structure can be obtained. The diffraction peaks can determine the d-spacing for the material, and when compared between an unloaded or loaded material can be used to determine the strain within the crystal lattice.

The synchrotron method also uses X-rays but with higher intensities and energy. Due to this, they have the ability to penetrate further into the depth of the material. The synchroton

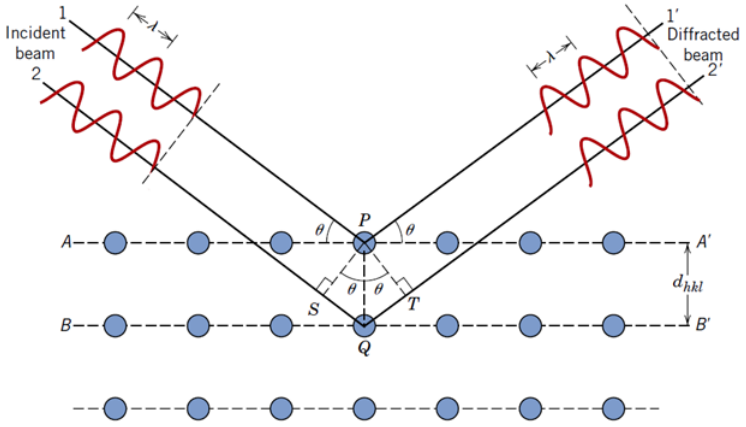

Figure 2.2. Diffraction of x-rays by planes of atoms [33]

method features Similar principles to X-ray diffraction, with the use of higher energy X-rays, allowing further penetration into materials than the X-ray method [29]. The higher energy in the synchrotron method also allows for quick measurement times and a smaller scan area, or resolution, than the X-ray method.

Measurement of Lattice Strain

The lattice elastic strain within the material, $\varepsilon^{hkl}(\eta)$, is found through using the d-space found with Bragg's law to evaluate the change in lattice spacing when compared to the strain-free lattice spacing, d_0^{hkl} [29] [30] and orientated in a theoretical loading direction dictated by η [34].

$$\varepsilon^{hkl}(\eta) = \frac{d^{hkl}(\eta) - d_0^{hkl}(\eta)}{d_0^{hkl}(\eta)} \tag{2.2}$$

An accurate determination of d_0^{hkl} is critical in an accurate lattice strain calculation as this value can vary depending on material temperature changes or changes in alloyed elements [29]. Additionally, very small changes in obtained lattice strain values can lead to very large changes in the determined residual stress, further adding to potential errors in the residual stress measurement [30].

Measurement of Stress from Lattice Strain

Calculation of the material's residual stress from the measured lattice strain relies on the relationship between stress σ and strain ε as second rank tensors[29]. Stress relies on the elastic stiffness tensor, C, whilst strain relies on the elastic compliance tensor, S. For an anisotropic material with a hexagon crystal structure, only five independent components ($S_{11}, S_{12}, S_{13}, S_{33}, S_{44}$) are required to complete the tensor [35]. Calculation of residual stress relies on a version of Hooke's law that has been adapted to account for the different grain orientations in the anisotropic material [29][34]:

$$\sigma_y^{hkl} = \frac{E^{hkl}}{(1+\nu^{hkl})}\varepsilon_{yy}^{hkl} + \frac{\nu^{hkl}E^{hkl}}{(1+\nu^{hkl})(1-2\nu^{hkl})}(\varepsilon_{xx}^{hkl} + \varepsilon_{yy}^{hkl} + \varepsilon_{zz}^{hkl}) \tag{2.3}$$

The relevant Young's Modulus and Poisson's ratio for each relevant hkl can be found by using the below equations [35]:

$$E_{hkl} = \frac{[h^2 + \frac{(h+2k)^2}{3} + (\frac{a}{c}l)^2]^2}{[S_{11}(h^2 + \frac{(h+2k)^2}{3}) + S_{33}(\frac{a}{c}l)^4 + (S_{44} + 2S_{13}(h^2 + \frac{(h+2k)^2}{3})(\frac{a}{c}l)^2]} \tag{2.4}$$

$$\nu_{hkl} = -\frac{[h^2 + \frac{(h+2k)^2}{3} + (\frac{a}{c}l)^2][S_{12}(h^2 + (\frac{(h+2k)^2}{3}) + S_{13}(\frac{a}{c}l)^2]}{[S_{11}(h^2 + \frac{(h+2k)^2}{3}) + S_{33}(\frac{a}{c}l)^4 + (S_{44} + 2S_{13})(h^2 + \frac{(h+2k)^2}{3})(\frac{a}{c}l)^2]} \tag{2.5}$$

2.2.3 Slitting

The slitting method utilizes a long slit incrementally cut on the specimen to release strain within the material, as shown in figure 2.3, which is then measured via a strain gauge [29] [36]. The incremental cut releases the residual stresses within the material at the surface height, allowing deformation to occur at the material surface. Slitting is able to effectively measure the residual stress field throughout the entire depth of the specimen. It is simpler and less expensive than contouring or X-ray diffraction methods.

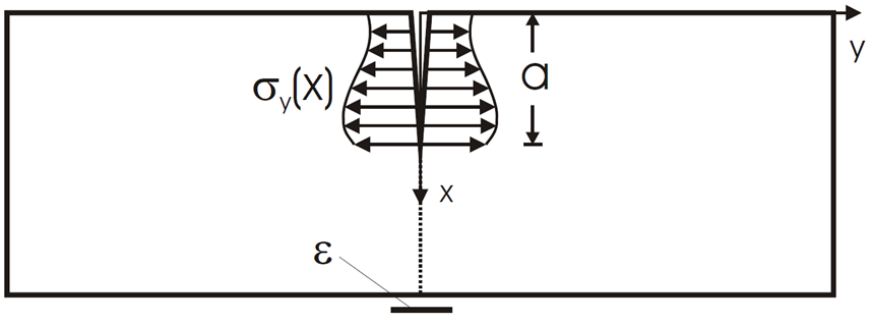

Figure 2.3. The incremental slitting method for measuring residual stress [36]

2.2.4 Contour Method

The contour method is a destructive method to measure residual stress through cutting a specimen into two pieces and directly measuring the deformation on the surface as the residual stress is re-distributed through the two pieces [29]. A finite element model uses the deformation, along with the material's stiffness and specimen geometry to provide a two dimensional cross-section map of the residual stress field normal to the cross section [37]. Using this method only the measurement of the surface deformation is needed with no required strain gauges.

The contour method was developed to measure complex residual stress fields that are not as accurately captured with other destructive methods such as slitting[37]. Additionally, it does not require complex analysis that is required from X-ray or neutron diffraction methods.

2.2.5 Comparison and Application of Methods

Previous research compared residual stress within Ti-6Al-4V using the slitting, contour and X-ray diffraction through layer removal methods [29]. Methods correlated fairly well, as detailed in figure 2.4, showing a similar stress distribution throughout the depth of the specimen from the free surface. Notably, there are deviations that are less than 100 MPa between HXRD and the destructive methods at the surface. A contributing factor leading to these deviations is higher uncertainties experienced by the destructive methods at the surface of the material.

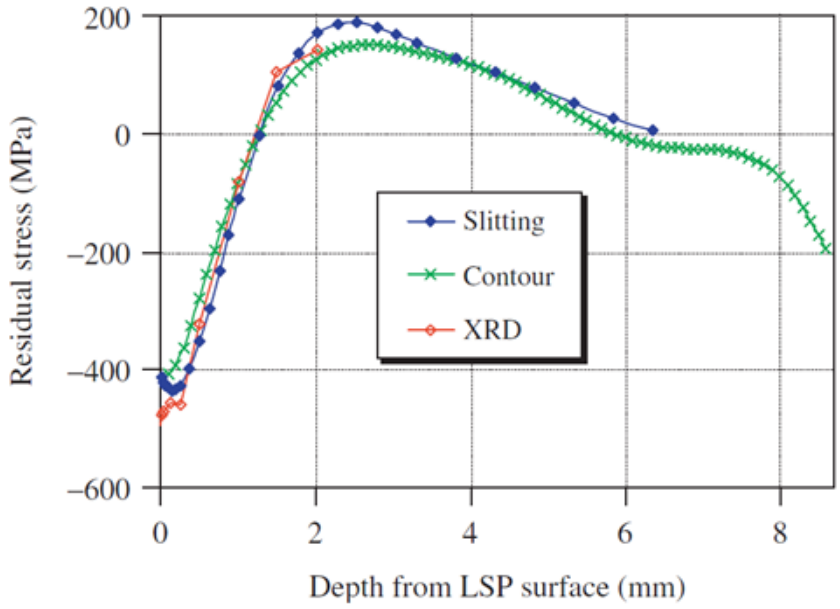

Figure 2.4. Comparison of residual stress results within specimen depth [29]

A study using Stainless Steel and Inconel 718 specimens manufactured with powder deposited through a laser, with residual stresses created within the specimens during the solidification of the molten metal [29]. Neutron diffraction and the contour methods were used to measure the residual stress, with a good correlation found between these two methods. The contour method was able to effectively capture the residual stress field within the specimens [29].

Research into laser clad repairs used the neutron diffraction method to analyze the difference between clad repair and clad repair PHT for Stainless Steel samples [28]. Residual stress magnitude of the clad repaired specimens was found to be significantly higher then the heat treated specimens both in compression at the surface and in tension a further distance within the material, as shown in in figure 2.5. This demonstrates the ability of heat treatment to relax residual stress within the material. These residual stress results were then used to determine the differences in fatigue life between the specimens. These findings will be discussed in the fatigue section of this literature review.

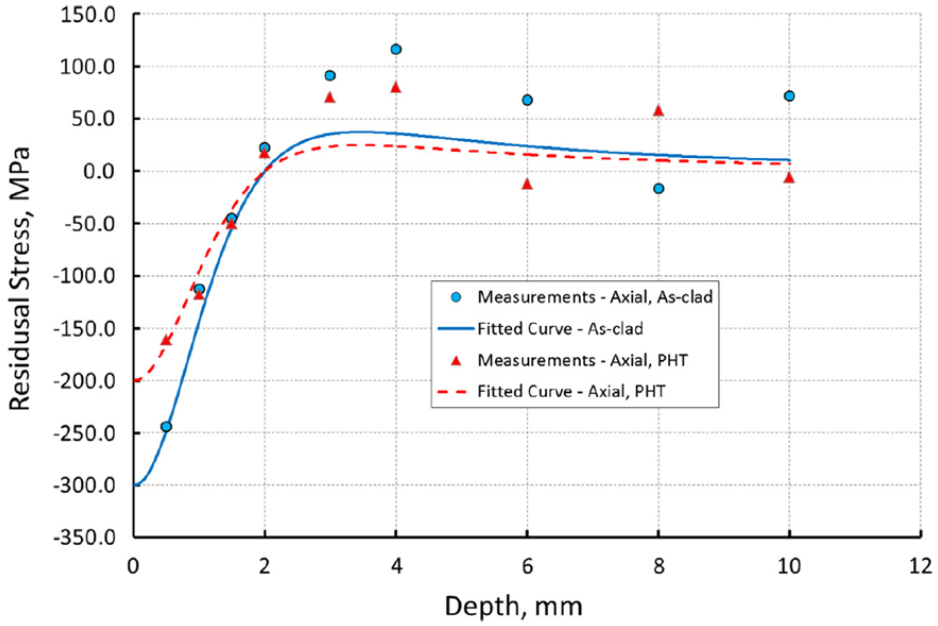

Figure 2.5. Neutron diffraction residual stress results for as-clad and as-clad PHT [28]

Research into the effect of deposition path on microstructure and fatigue properties of Ti-6Al-4V compared two patterns within the context of a simulated Ti-6Al-4V laser clad repair [10]. The contour method was used to measure the residual stress field within the substrate and clad, with neutron diffraction methods discounted due to the small size of the clad layer, at 0.6mm, with previous research indicating a correlation between neutron diffraction and the contour method [38]. LMD-1 featured a typical deposition strategy with a continuous deposition strategy, with LMD-2 featuring a 60 second pause at the end of each deposition track. This change in deposition strategy was found to influence the tensile residual stress within the clad and substrate, as shown in figure 2.6, with the LMD-2 strategy incurring 50% higher residual stresses at clad surface then the LMD-1 strategy. This is due to the changing thermal gradients experienced during the deposition process, with the pause in deposition tracks allowing more time to cool the deposition surface layer before another deposition layer is added [10]. However, the presence of the tensile residual stress continued further into the specimen depth in LMD-1 than LMD-2.

Energy Dispersive (X-ray) Diffraction (EDD) has been used to characterize the residual strain present in titanium alloys from linear friction welding. Research has compared similar

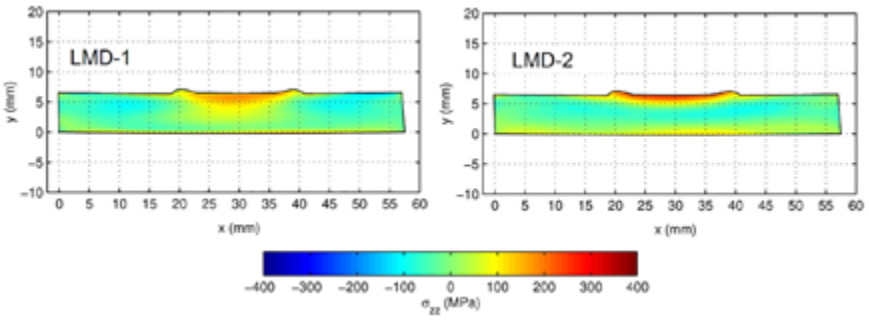

Figure 2.6. Residual stress cross section map measured using contour method for LMD-1 and LMD-2 [10]

and dissimilar material welded together, in addition to comparing samples as-welded or with a heat treatment applied after the weld process [39]. Materials welded together to form this comparison included two similar pieces of alloy Ti-6Al-4V and the dissimilar alloys Ti-5Al-5V and Ti-6Al-4V. A strain tensor map for the welded region was attained through calculating the lattice strains within each welded section through analysis of the EDD data and peak fitting using the Pseudo-Voigt function within Matlab. Key findings relating to this chapter are the symmetrical nature of the in-plane axial strain tensor and, as expected, the treated specimens exhibited significantly reduced residual strains than the as-welded specimens [39].

The EDD method was used in an attempt to characterize the residual stress within Ti-6Al-4V dog-bone specimens which featured an as-clad repair, with two configurations of clad repaired specimens and heat treated clad repaired specimens [40]. EDD measurements were conducted on both samples scanning 2.5mm through the clad and into the substrate material. However, use of a gauge scan area of 200 x 50 μm failed to produce scans of sufficient intensity to detect relevant diffraction peaks for lattice strain analysis, as detailed in figure 2.7. This gauge area was increased to 500 x 50 μm with some improvement in intensity output, however a resultant lattice strain could not be effectively determined [40]. The author concluded the gauge size provided by the EDD method was not large enough for the large grain sizes of the substrate. For materials with a large grain size, alternate methods would be required.

Most manufacturing processes can create residual stresses of some kind, with AM being no different [29]. The presence of large thermal gradients within the solidification process,

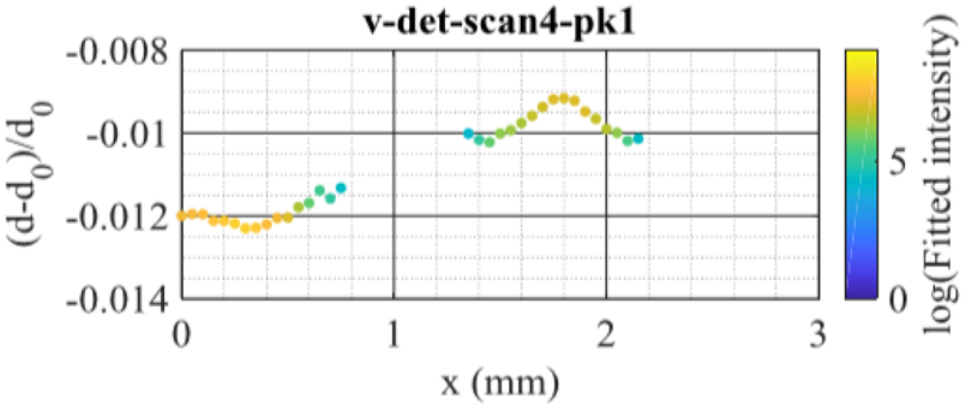

Figure 2.7. Inconsistent lattice strains for EDD application [40]

and associated material density or phase changes are mechanisms that can cause residual stress within materials. A more comprehensive analysis of the measurement and the impacts of residual stress on fatigue crack growth will provide information that is required for certification of AM repairs for critical structure.

2.3 Fatigue Crack Growth

Components fail from fracture either in a testing environment or from in-service loads due to a number of reasons. These can include plastic deformation and crack initiation leading to crack growth within the material. Fracture occurs upon exceeding the materials' allowable crack length. Residual stresses created during manufacturing or repair process can influence the material properties of the component, due to plastic deformation, varying cooling rates and/or material phase transformations [41] [42]. The interactions between the residual stress within the component and the loading stress from in-service flight loads determines the ultimate fatigue behavior of the component [41].

This body of work will utilize the Linear Elastic Fracture Mechanics (LEFM) framework to consider the crack growth within materials. This method will consider a flaw that is initially assumed or demonstrated to be present in the material which then develops a crack under loading and environmental factors. Finally, after crack growth reaches a critical size fracture occurs in the material. This behavior is identified between the Paris law, describing

the rate of crack growth, and stress intensity range, ΔK [43]. The Paris law is detailed in equation 2.6, with C and n being constants that are dictated by material properties.

$$\frac{da}{dn} = C(\Delta K)^n \tag{2.6}$$

The magnitude of K varies on the applied loading, crack shape, the mode of crack displacement and the component or test specimen geometry, F [43] [44].

$$K = F\sigma\sqrt{\pi a} \tag{2.7}$$

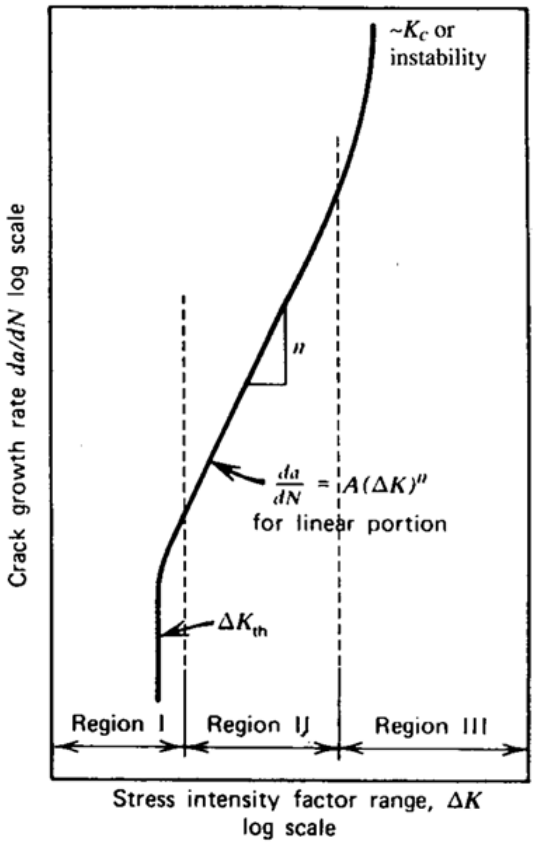

Figure 2.8. Behavior of fatigue crack growth rate [44]

There are three regions within the LEFM model as shown in figure 2.8. Region I is considered to be the initiation phase of cracks and is dictated by the presence and propagation of short cracks. Crack growth in this region is dominated by microstructural characteristics.

Crack growth through Region II is where the crack propagates in a manner dictated by the Paris Law, with minimal influence by the material's microstructure and mean stress. In Region III the crack growth rate is high and becomes unstable, leading to final fracture of the material. Behavior in this region is influenced by the material's fracture toughness, dictated by the material microstructure and environmental factors [44].

Fatigue crack growth is described as a crack tip surrounded by a plastic zone [44], which in turn is surrounded by a stress field [41]. However, if the crack propagates into a residual stress field then the crack growth behavior can be influenced by this residual stress field. Research indicated that between microstructure, presence of pores and residual stress, residual stresses within the material are the main influencing factor on the crack growth behavior [45]. However, the use of heat treatment was shown to significantly reduce the magnitude of the residual stresses with a threefold increase in the crack growth threshold value.

The effect of residual stress on fatigue crack growth rate and the stress intensity factor can be evaluated through the application of LEFM the use of Paris law with the stress intensity factor and considering the effect a residual stress field has on the crack tip. A compressive residual stress field impedes crack growth as the tip is compressed, which decreases the fatigue crack growth rate [46]. This improves the fatigue life of the material. To model the effect of residual stress at the crack tip, the stress ratio, R, can be modified by the following equation:

$$R = \frac{S^a_{min} + \sigma^{RS}_N}{S^a_{max} + \sigma^{RS}_N} \tag{2.8}$$

Utilizing this expression and a modification of the walker equation the influence of residual stress on the Stress Intensity Factor can be isolated, with S_{open}, selected as S_{min} to assume the crack is always open, representing the stress required to open the crack.

$$\Delta K_{eff} = \Delta K \frac{(1 - \frac{S_{open}}{S_{max}})}{1 - R} \tag{2.9}$$

The presence of tensile residual stress has been demonstrated to be harmful to fatigue life as it can cause surface or subsurface crack initiation or increase crack growth rate [41][42]. This is particularly evident in additive manufactured materials due to the high thermal

gradients experienced during manufacture [22]. The presence of tensile residual stress has been found to reduce fatigue life in Additive Manufactured Selective Laser Melting (SLM) materials [47][48].

The presence of compressive residual stresses at the surface or subsurface of the material can be beneficial for fatigue life as they can prevent or delay initiation and propagation of cracks [42][49] when the residual stress are stable in the regions where the highest loading is applied [41]. These desired locations are particularly applicable to the surface of the component, which is also applicable to component repairs. Additionally, residual stresses are particularly effective when applied to materials with a high tensile strength. Due to the minimization of the effects of notches and scratches, the high tensile strength can be maximized throughout the component service life [44] or operated at both room and cryogenic temperatures.

Compressive residual stresses can be introduced to the material through the application of surface techniques such as shot peening, laser shock peening and low plasticity burnishing [42][50]. Quantifying these compressive residual stresses through clad repairs or artificially induced has been difficult, with the compressive residual stresses considered to be an additional safety factor rather than counted in the calculations of component fatigue life [50]. However, understanding the influence of residual stress on fatigue life is important for not only accurately predicting total fatigue life, but to predict crack initiation and growth throughout in-service loads. This will enable certification for repairs featuring the presence of residual strength, particularly repairs that utilize AM methods.

Due to the negative effects of tensile residual stresses, re-distribution of tensile residual stresses can significantly improve the fatigue life of components. These relaxation methods can remove tensile residual stresses and, process dependent, imbed compressive residual stresses into the surface and sub-surface. Some techniques may only relax tensile residual stresses within the material [45], such as annealing, whereas peening methods can also introduce compressive residual stresses at the surface and subsurface of the component [41][42]. Annealing does not completely remove residual stresses within the material as dislocations and other defects within the crystal lattice can still contribute to the presence of residual stresses within the material.

Investigations on the influence of clad repairs and associated residual stresses on the fatigue life have been conducted on both Stainless Steel and Ti-6Al-4V materials. A study compared laser clad repairs on AISI 4340 steel using AISI 4340 and AerMet 100 powders as the clad repair simulating a repair to a high strength steel aircraft landing gear. Both as-clad and heat treated specimens were subjected to fatigue testing [22]. Whilst using the same material in the clad repair as the substrate allows for simpler evaluation for repair certification, in this case the AerMet 100 displayed better fatigue life than the AISI 4340 steel. This was mostly attributed to the poor material properties of the AISI 4340 clad. Despite a reduction of measured compressive residual stresses in the heat treated specimens, an increase in fatigue life was observed for both material types over the as-clad specimens, due to the improved material properties imparted to the steel clad and substrate [22]. The authors noted that despite the benefits of the extended fatigue life due to heat treatment, potential distortion of the repaired component and difficulties in certification would make implementation challenging.

Evaluation of laser clad repairs on AerMet 100 Stainless Steel coupons revealed a region of compressive residual stress at the surface and subsurface of the coupons which penetrated further than what would be achieved with shot peening. These repaired coupons were compared to specimens which had also undergone heat treatment designed to relax the residual stresses within the material. The fatigue life of the clad repaired coupons was shown to be significantly larger than the heat treated specimens [28]. Of note the heat treated coupons still retained considerable compressive residual stresses which aligned with the improved heat treated fatigue results over the unprepared tested specimens.

Research was conducted to evaluate the effect of laser clad deposition strategy on the microstructure and fatigue of repaired Ti-6Al-4V. Tensile residual stresses were found at the surface and sub surface of both of the specimens evaluated, with fatigue testing showing a lower the fatigue life than what would be expected from a baseline of mil-annealed Ti-6Al-4V. Whilst the deposition design featuring lower tensile residual stress values featured a shorter fatigue life, this was attributed to a greater number of defects within the specimens rather than the differing residual stress fields create by the deposition repair process [10].

The authors acknowledge that through removal of the effect of defects within the clad repair, an effective evaluation of the effect of residual stress on fatigue life could be conducted.

2.4 Marker Band Technique and Ti-6Al-4V Fractography

2.4.1 Quantitative Fractography

The use of Damage Tolerance method in aircraft certification requires knowledge of the predicted fatigue life cracks of structural aircraft components. This is determined through fatigue testing of materials, components or full-scale fatigue tests of separate aircraft structures, and continued testing to destruction of in-service components to validate predicted fatigue crack growth behavior. Quantitative Fractography (QF) is method of identifying features on a fracture surface against test or in-service loads for the purposes of measuring fatigue crack growth [51][52] [53]. Marker Bands (MB) are the main features of a fractured surface through crack growth, with curved lines originating out from the crack origin until failure occurs [43]. These features on the fracture surface are matched against the loading and environmental history of the test specimen or component to determine the fatigue crack growth history. Additionally, the natural MBs produced through fatigue crack growth may not be sufficient to allow accurate measurement. There have been several methods developed to modify the load history to allow easier or more accurate counting of MBs including overloads, underloads and Constant Amplitude (CA) loading [53].

The addition of overloads or underloads can be used to improve MB detection. The benefit of overloads is the creation of a MB pattern that can be easily determined on the fracture surface, however, care must be taken to minimize the severity of the load spectrum [53]. Additionally, the use of overloads and significant changes in load severity can result in retardation of fatigue crack growth, which affects the total life determination of the specimen or component. The use of underloads utilizes high compressive loads to create recognizable MBs on the fracture surface. Whilst the influence of underloads on fatigue crack growth behavior appears to be less then overloads, research has indicates these compressive loads can increase the measured crack growth rate, in addition to the high compressive loads posing a risk of buckling in the test specimen [53]. Finally, the use of CA MBs with a significant

difference of R values between the CA MB and the applied load R value can provide easily identifiable MBs on the fracture surface, however the application of CA MBs can have a significant influence on crack growth rate. This influence can be minimized by inserting the CA MBs with varied R values for short intervals, or narrowed intervals, amongst the regular loading of the test specimen or component [53].

QF has been used to evaluate fatigue crack growth of stainless steel specimens that featured a laser clad repair to a notch taken out of the steel. Both the HAZ, clad region material substrate were examined. In this case both an optical and Scanning Electron Microscopes (SEM) were used to conduct the QF measurements [28].

Research has demonstrated an ability to design MBs on the fracture surface of Ti-6Al-4V with larger than expected loads when compared to other common alloy materials such as Aluminum 7050 [52]. However, the MBs produced were not continuous across the entire crack growth direction, instead they were only identified across short segments. The authors suggested a smaller amount of slip planes from the the HCP crystal structure of Ti-6Al-4V contributed to fewer grains that were aligned in a manner suitable for MB formation [52]. A comparison between aluminum and titanium fracture surfaces shown in figure 2.9 illustrates the rough surface typically found in titanium fracture surfaces that can make QF applications challenging.

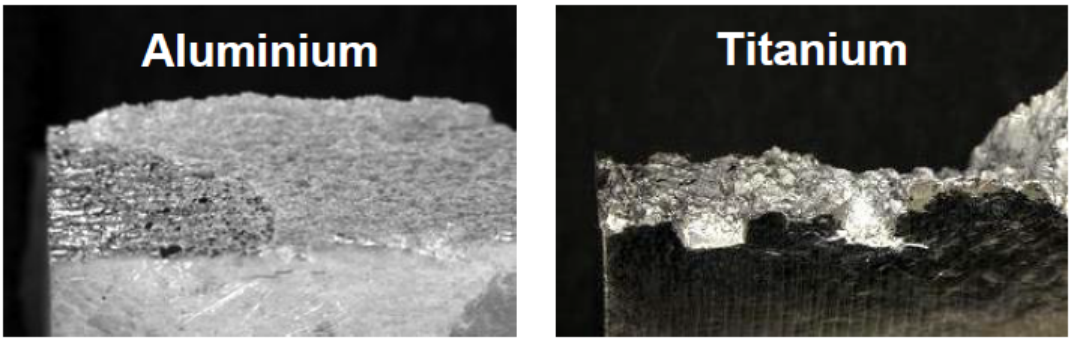

Figure 2.9. Fracture surface comparison between aluminum and titanium [52]

Recent research has been conducted on Ti-6Al-4V specimens that have experienced success in identifying and measuring fatigue crack growth rate from MBs. The specimens were subjected to a laser clad repair to determine fatigue performance between clad repaired and

repaired specimens that have undergone heat treatment. Both optical and scanning electron microscopy was used to identify the MBs on the Ti-6Al-4V with the SEM providing the best results with images of a higher quality, as seen in figure 2.10 [40].

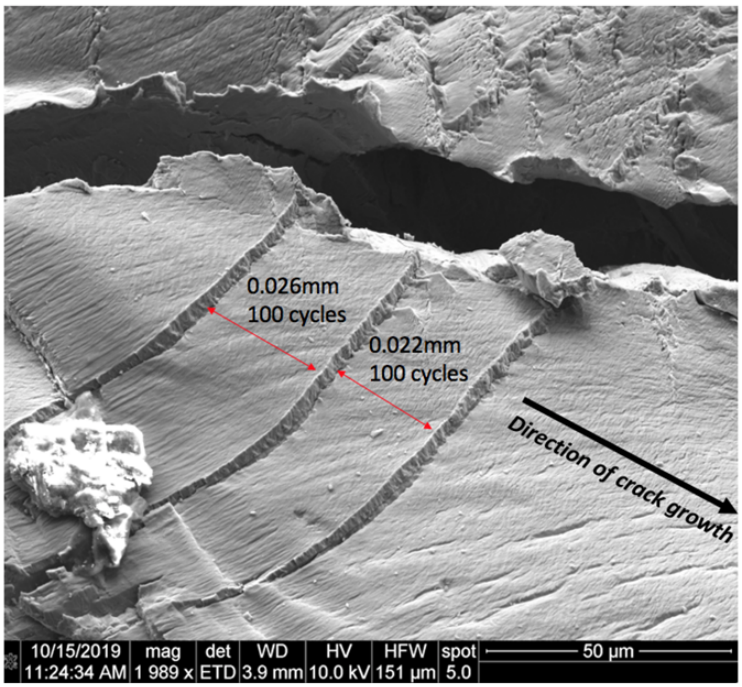

Figure 2.10. Ti-6Al-4V Marker band measurement [40]

Additionally, due to the short focal range used in the optical microscopes the changing topography of the Ti-6Al-4V fracture surface made MB identification and measurement very difficult. Some results were achieved through stacking multiple images together to form one image in relative focus, however this method did not always provide images for use in identifying and measuring MB progression. However, SEM images were able to provide a good comparison to baseline Ti-6Al-4V data from a DST Group crack growth rate simulation [40].

2.4.2 Automated Quantitative Fractography

Whilst the current QF methods have been effective in characterizing the fatigue crack growth behavior of materials, it is prone to human error and generally requires a high

skill level to provide accurate outcomes that align with test or in-service loading history. Additionally, it is a labor intensive process that can take a significant time to complete [54][55]. Current research in this area seeks to provide either assistance to QF operators in detecting MBs and other features on a fracture surface, or automating the entire process.

Several image processing methods from SEM images have been used to identify MBs generated through fatigue testing of test specimens [54]. Marker bands of a predictable and regular nature were detected with input from the operator in first identifying the direction of Marker Band progression. Whilst this process produced promising results it can be considered to be more of an assistance to the operator rather than an autonomous detection method, the authors note that future work is planned for utilization of machine learning to reduce the amount of noise and false positives generated by the image recognition software.

3. SPECIMEN DESIGN

3.1 Specimen Configurations

Dog-bone specimens were utilized to simulate a laser clad repair on a Ti-6Al-4V aviation component. The specimens were made from Ti-6Al-4V material that was provided by the Royal Australian Air Force (RAAF). Three different configurations were used for this research and are as follows:

- 'As-clad' specimens featured a machined groove with a laser clad applied to fill out the groove, simulating an applied repair,
- 'Post-clad Heat Treatment' (PHT) specimens featured the same design as the 'As-clad' but with a heat treatment applied to 480 °C for two hours, simulating a repair with a relaxation of the residual stresses that are associated with the laser clad repair process; and
- A 'Baseline' material of Ti-6Al-4V with no clad repair applied for use as a benchmark against the laser clad specimens.

The Ti-6Al-4V sheet was cut into three parts, with two selected for the clad repair application. The laser clad method was applied to the groove with excess laser clad material machined back to the original dimensions of the sheet. Each plate was then machined to produce six dog-bone specimens with a total of 18 specimens for use. A list of all specimens used in this research and the preceding body of work is shown in Table 3.1. Any specimens that are in the latter category are denoted by an asterisk.

The original specimen design, design 1, is shown in figure 3.1. The dimensions of figure, and all other figures within this chapter, are expressed in mm. This design featured a large gauge section and a clad thickness of 0.7 mm for the As-clad and PHT configuration to reflect a simulated repair depth of approximately 10%. Three notches were machined into the laser clad surface, or in the equivalent location in the baseline specimens, to provide a known crack initiation site to start quantitative fractography. This research utilizes design 1 for the measurement of residual stresses for an As-clad and PHT repair. Previous research

Table 3.1. Specimen configuration

ID	Design	Application	Type
1A	3.1	Fatigue	As-clad
1B*	3	Fatigue	Baseline
2A	3.2	Fatigue	PHT
2B*	3	Fatigue	As-clad
3A*	2	Fatigue	Baseline
3B	3.2	Fatigue	PHT
4A	3.2	Fatigue	As-clad
4B	1	RS Measurement	PHT
5A	3.2	Fatigue	Baseline
5B	1	RS Measurement	As-clad
6A*	1	Microstructure Characterization	PHT
6B*	2	Fatigue	Baseline
7A*	1	Microstructure Characterization	As-clad
7B	3.2	Fatigue	Baseline
8A*	3	Fatigue	Baseline
8B	3.2	Fatigue	PHT
9A	3.2	Fatigue	As-clad
9B*	3	Fatigue	PHT

also featured this design for microstructure characterization of each specimen category [40]. However, due to limitations in the maximum load that could be applied in fatigue testing, the remaining specimens identified for fatigue testing and crack growth rate measurement featured a revised design to reduce the specimen cross-sectional area.

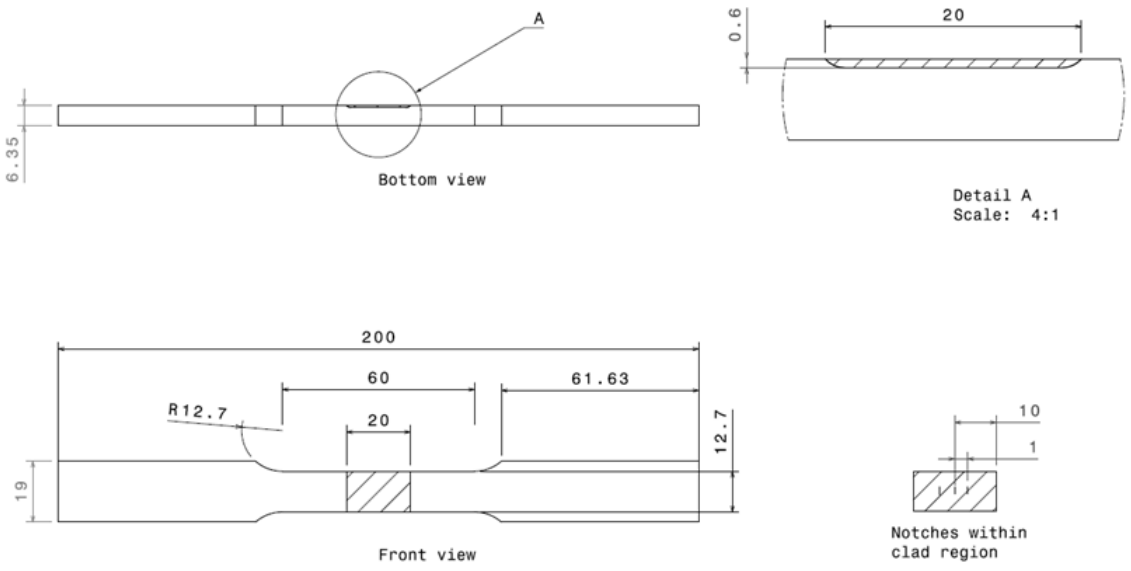

Figure 3.1. Specimen design 1

Design 2 featured in previous research featured a reduced cross-sectional area to 5.70 x 6.35, this change reflects a 50% reduction in cross section area than design 1 [40]. Two specimens were tested with this design, with one failure at the transition between the neck and gauge section and one failure occurring at the gauge section. However, these two tests did not achieve an outcome of crack initiating in any of the notches [40]. Therefore, another design revision was conducted to further promote fracture at any of the notch locations.

Design 3, detailed in figure 3.2, featured a smaller cross-sectional area than design 1 but a more gradual transition from the specimen grip area to the gauge area than design 2 to reduce the stress concentration effect that is produced by a change in dimensions[40][44]. This design was tested through previous research and will be the basis for the fatigue testing and quantitative fractography conducted in this research.

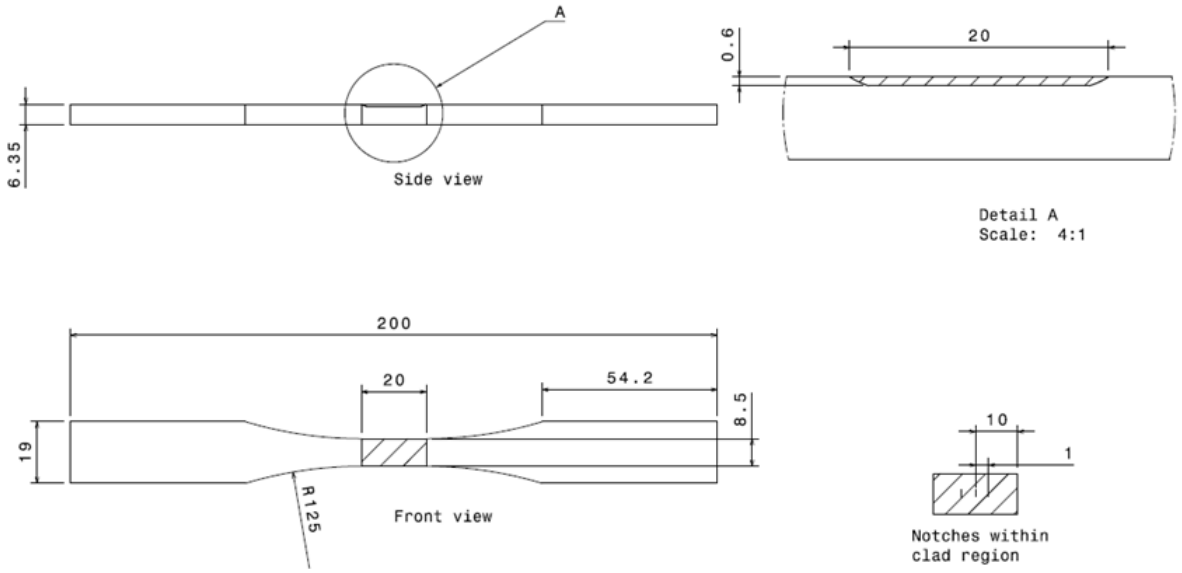

Figure 3.2. Specimen design 3

Despite the changes made in Design 3 only one sample out of four that underwent fatigue testing experienced a failure at a notch in previous research. Of the four tested, three failed in the gauge section of the sample [40]. Failure at the notch is desired as it allows visual tracking of crack progression and a known crack initiation site which makes marker band detection and tracking easier via SEM. However, a greater reliability was desired to ensure failure occurred at the notch. If the specimen design did not reliably cause failure at the notch location, it could fail in other areas of the specimen. For example, if crack initiation started at the rear of the specimen, away from the clad region, the crack growth rate in the clad region could not be measured as the clad repair would only experience unstable crack growth associated with region III prior to final failure [43].

Several options were considered in the specimen re-design. Shot-peening was considered due to its ability to embed compressive residual stresses at the surface of a material [44]. An application of shot-peen outside of the gauge section would discourage crack initiation outside of the gauge location and would minimize the probability of failures such as seen in specimen 1B [40] which saw failure at some distance from the gauge, at the transition from the gauge to the grip area. Additionally, due to an absence of crack initiation at the notches, the need for a revision of the notches themselves was apparent to further increase the stress

concentration at the free surface of the gauge section, within the clad repair. A large array of notches with a total area of 5 x 5mm was considered to provide a site of multiple stress concentrations to promote crack initiation at the clad surface.

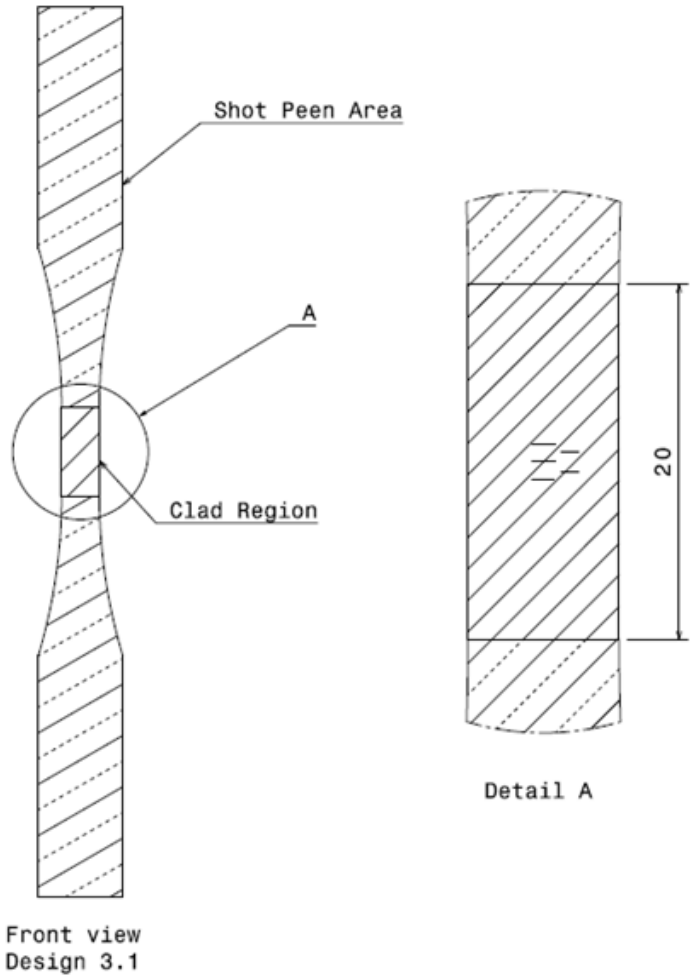

Figure 3.3. Specimen design 3.1

Ultimately, the modifications to design 3.1 included the application of the shot-peen technique to the specimen, two additional notches and a slight lengthening of the notch width and depth. All areas of the specimen surface outside of the gauge section were subject to the shot-peen technique, as detailed in figure 3.3. Shot-peening was applied to the specimen via 0.6 mm diameter S230 steel shot, conducted to the SAE standard J2277_201304. Additionally, all sharp edges on the specimens were machined with a 1mm radius, corresponding to

twice the shot diameter. However, to balance the need to scan each notch for signs of crack growth during the experiment and to expand the number of notches in the gauge section, two additional notches were added, vertically off-set from the position of the original notches, as detailed in figure 3.3.

One specimen, 1A, was modified to design 3.1 to serve as a test to confirm the effectiveness of the design in promoting crack initiation within the clad region. Ultimately this design was not successful, with failure occurring at the boundary between the gauge section and the shot-peen material at the specimen shoulder. Chapter 5 contains more details on this failure. Due to the unfavorable failure of specimen 1A, which did not feature any crack initiation at any notch, a further and final design revision was conducted. Due to failure of 1A to prevent crack initiation and failure outside of the gauge region the shot-peen area was further increased into the gauge section. Only 10 mm was left of the clad area that was free of the shot-peen application. As the additional notches associated with design 3.1 did not induce crack initiation, as seen in figure 3.8, they were discarded. Instead, a wider notch, or slot, was added in the location of the center notch, 5.5mm wide and 0.05mm deep into the clad region to further promote crack initiation and growth in the clad region as detailed in figure 3.4.

Due to the large machined slot it would be expected that failure would occur in the middle notch only. Additionally, the shot peen area was expanded into the clad region so that the transition point between the shot peen area and the clad region would not act as a stress raiser. The remaining specimens, 7 in total, were machined to the 3.2 design. Ultimately four of the 7 specimens failed at the slot with only one sample featuring a failure outside of the gauge region, rendering design 3.2 somewhat successful. These failures are described in greater detail in chapter 5.

3.2 Laser Clad

The laser clad deposition process was conducted at the Royal Melbourne Institute of Technology (RMIT). The two plates selected for the clad repair were first sandblasted and then ultrasonically cleaned. These steps improve the ability for the surface to bond with

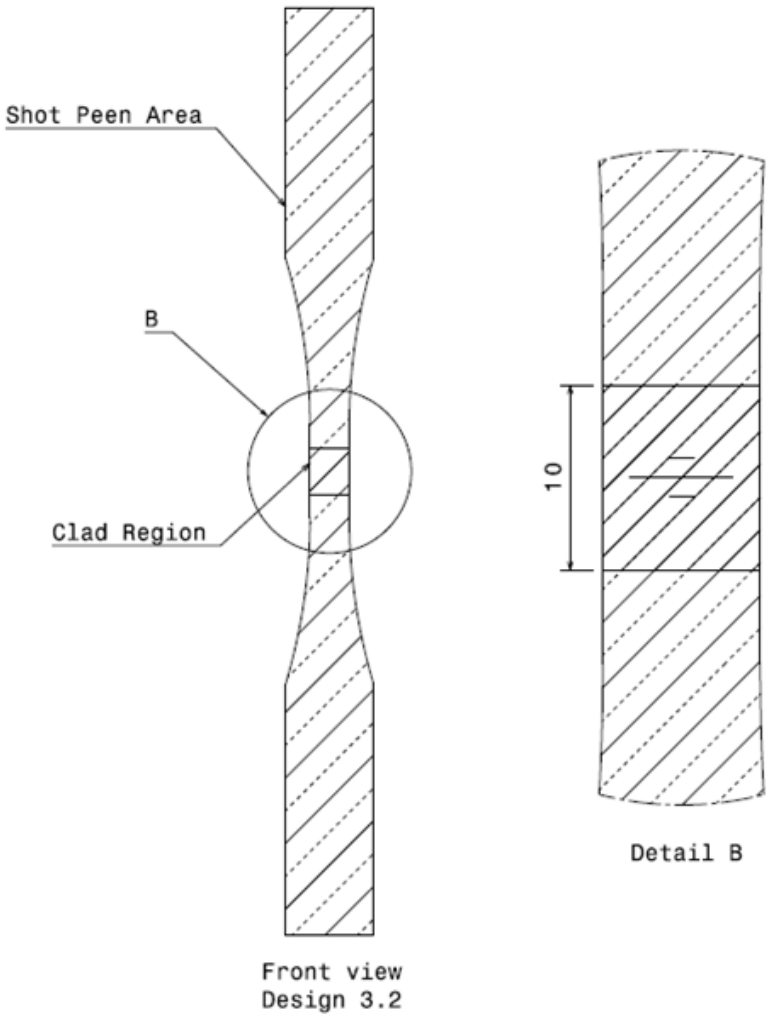

Figure 3.4. Specimen design 3.2

the clad layer and removes any surface contamination from the surface. The laser clad was conducted with a TRUMPF TruLaser Cell 7020 system with a Flapro CNC program commanding the deposition pattern, as shown in figure 3.5. The clad featured a Ti-6Al-4V TLS TECHNIK powder with Helium (10L/min) used as the carrier gas and Argon (16L/min) as the shielding gas. Laser Clad parameters are detailed in table 3.2. The continuous deposition pattern is shown in figures 3.5 and 3.6, with cooling to room temperature conducted post-deposition before moving onto the next simulated repair region on the plate. The deposition pattern required 27 passes at a stepover of 0.75mm for a total distance of 20mm.

Following completion of laser clad deposition, the clad surface was machined to ensure the original dimensions of the specimens are restored.

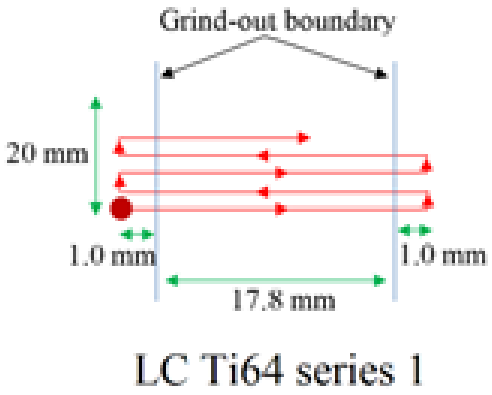

Figure 3.5. Deposition pattern [40]

Table 3.2. Laser clad parameters

Parameter	Value	Units
Laser Power	700	W
Laser Speed	600	mm/minute
Powder Flow	2.3444	g/min
Powder Size	45-90	mm

3.3 Notches

The notches associated with designs 1 and 3 were cut at MINIFAB, Melboune Australia. The notches, measuring at 50 x 30 μm were laser cut using a Coherent Industrial AVIA^{TM} Nd-YAG laser producing a 10μm Full Width Half Max (FWHM) beam at the laser focus point, 165 mm away from the objective lens [40]. A CAD drawing of the three notches was transferred to a Hewlett-Packard^{TM} graphics language, which converts these vectors to a signal processor in the laser to direct the control of mirrors within the laser to direct the laser beam. A SEM image of these notches is shown in figure 3.7.

The design 3.1 configuration featuring an additional two notches, and modification of the original three notches, was machined to specimen 1A at Defence Science and Technology

Group (DST) in Adelaide, Australia. Two additional notches were machined, offset from the vertical axis of the original notches, as shown in the optical microscope image in figure 3.8. The width of the notches is 100μm, with a depth of 50μm. These dimensions were also applied to the original three notches.

The new slot added to design 3.2 as shown in the optical microscope image in figure 3.9, applied the middle notch, was machined to the remaining specimens at DST in Adelaide, Australia. The slot width is 5.5 mm, approximately two thirds the width of the gauge section of the specimens. As this slot is applied across a large part of the free surface, its depth was reduced to 10 μm to ensure a balance is maintained between creating a sufficient stress concentration at the free surface for consistent crack initiation and allowing enough thickness in the clad region for marker bands to be produced via fatigue loading.

3.4 Heat Treatment

Heat treatment is a common method to relax residual stresses within a material, either produced through AM or, as in this case, part of an AM repair [7][28]. Additionally, relaxation of stresses within the material are one of the most common reasons for application of heat treatments post-manufacturing [17].

In this research PHT specimens were heat treated at 480 °C for two hours [40], which is within the recommended Ti-6Al-4V temperature range of 480°C - 650°C for the purposes of stress relief [17]. The duration of the heat treatment can be within one to four hours with the majority of the stress relaxation occurring within the first hour [17].

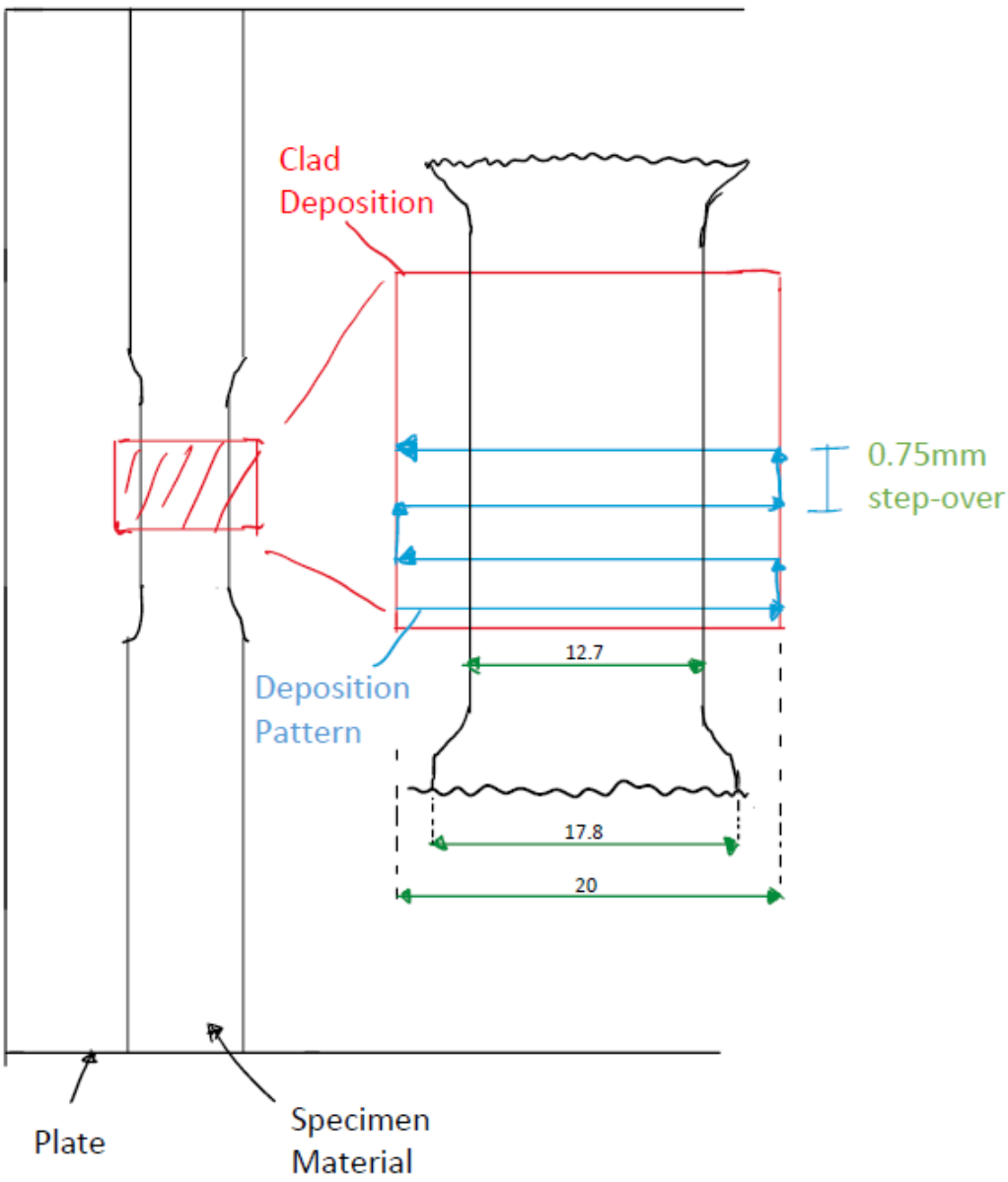

Figure 3.6. Deposition pattern

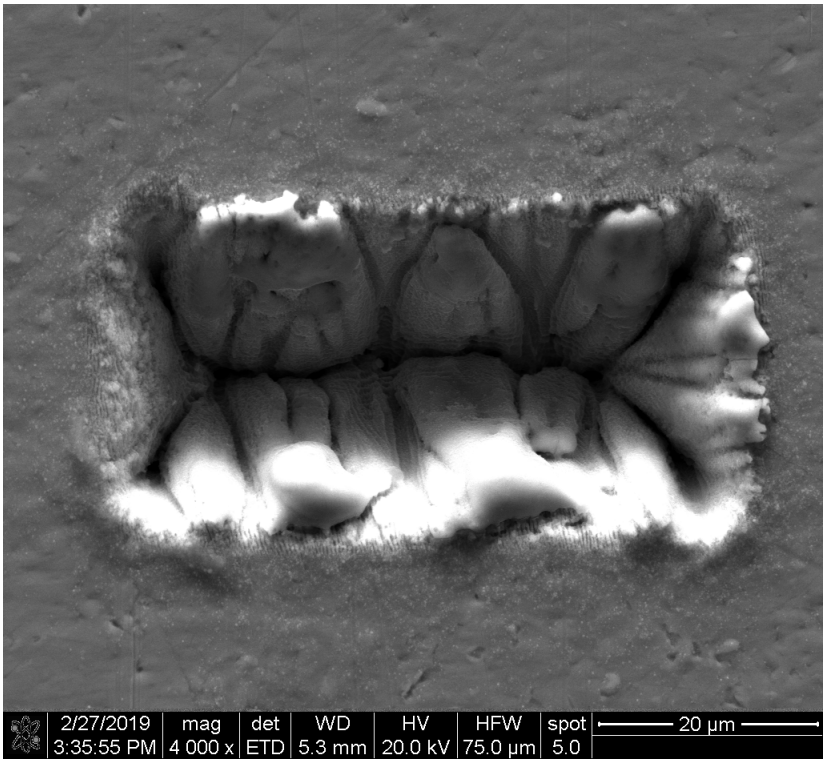

Figure 3.7. Original notch [40]

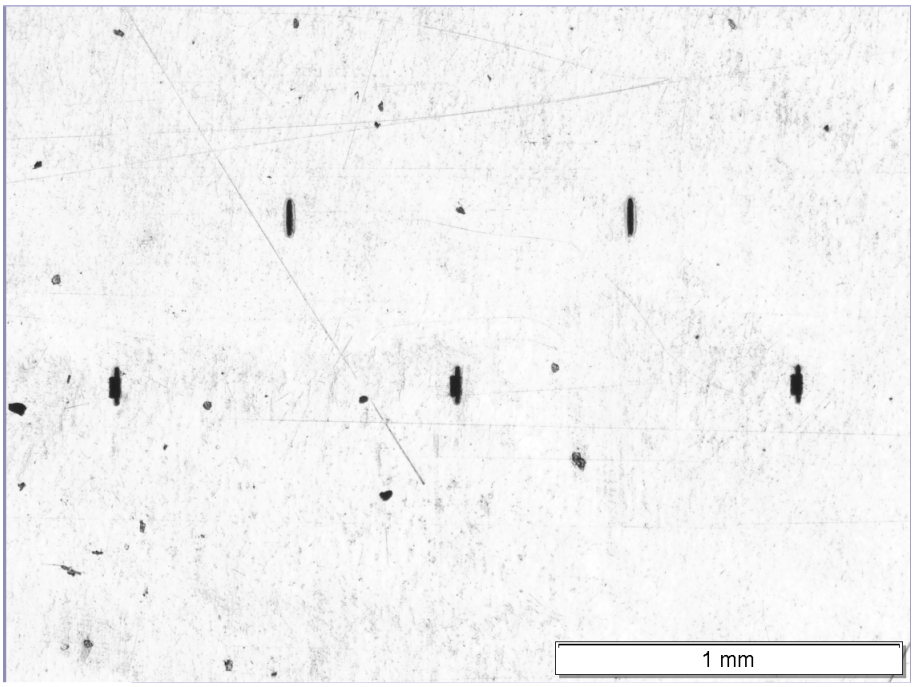

Figure 3.8. Specimen design 3.1 notches

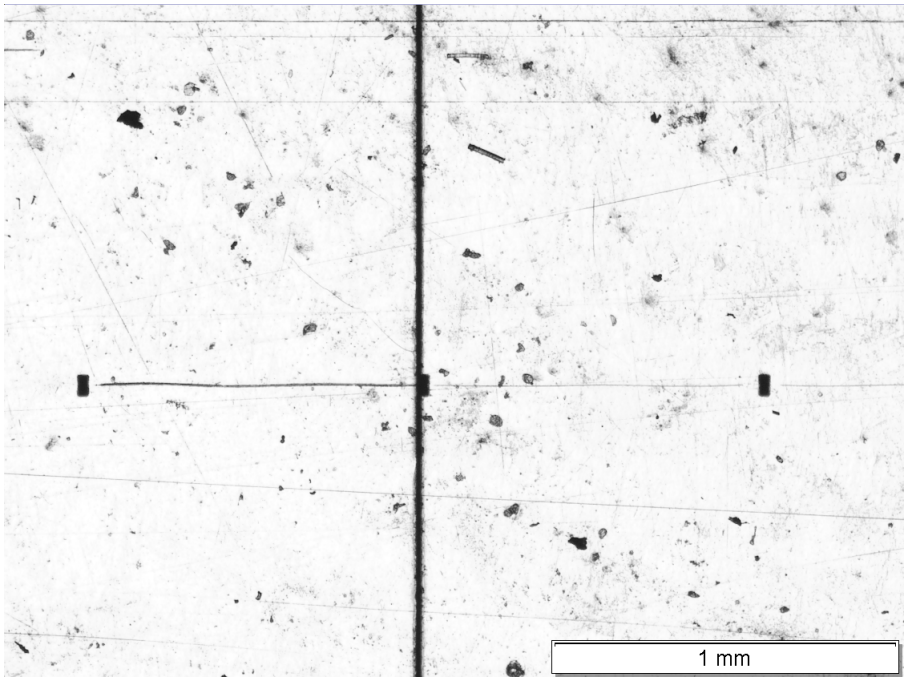

Figure 3.9. Specimen design 3.2 notches

4. RESIDUAL STRESS

The measurement of the residual stress present within the laser clad repair and surrounding substrate will significantly affect the fatigue performance and crack growth rate of the repair, in particular when conducting a comparison between the 'As-clad' specimen and the PHT specimen. An understanding of this behavior is key in further developing the predictability of structural performance of the laser clad repair, with this consideration one of the factors of the Lincoln technology criteria, which are factors that are considered essential to resolve prior to implementing materials technology onto aircraft, in particular aging aircraft [12]. Predictability is an important factor as full-scale static and damage tolerance tests within whole aircraft programs are expensive, and would not be considered a practical application for aircraft repairs.

Two specimens featuring design 1 were selected for non-destructive residual stress tests through Energy Dispersive Diffraction (EDD) scans in previous research [40]. These two specimens, 5B (As-clad) and 4B (PHT), were selected for further non-destructive and destructive inspection methods in this research to provide an understanding of the fatigue crack growth behavior between the As-clad and PHT repair methodologies. The presence of residual stress adversely affects the performance of AM repairs, with a tensile residual stress reducing the life of the repair [10][28].

4.1 X-ray Diffraction

4.1.1 Background and Objectives

The objective of the measurements conducted in this research is to use X-Ray diffraction to measure the inter-planar spacing of the material. This can then be used to characterize the lattice strain within the clad repair and underlying substrate regions. The holistic approach within this research taken to fulfill this objective is outlined in figure 4.1 for reference throughout this chapter. From the lattice strain and the application of Ti-6AL-4V material properties, the residual stress within the specimens can be calculated, allowing a comparison between the As-clad and PHT specimens and their influence on the fatigue life of the

clad repair. As stated in the literature review, Bragg's law can be utilized to evaluate the distance between crystal lattices, d_{hkl}, with identification of diffraction peaks leading to an understanding of the lattice crystal structure.

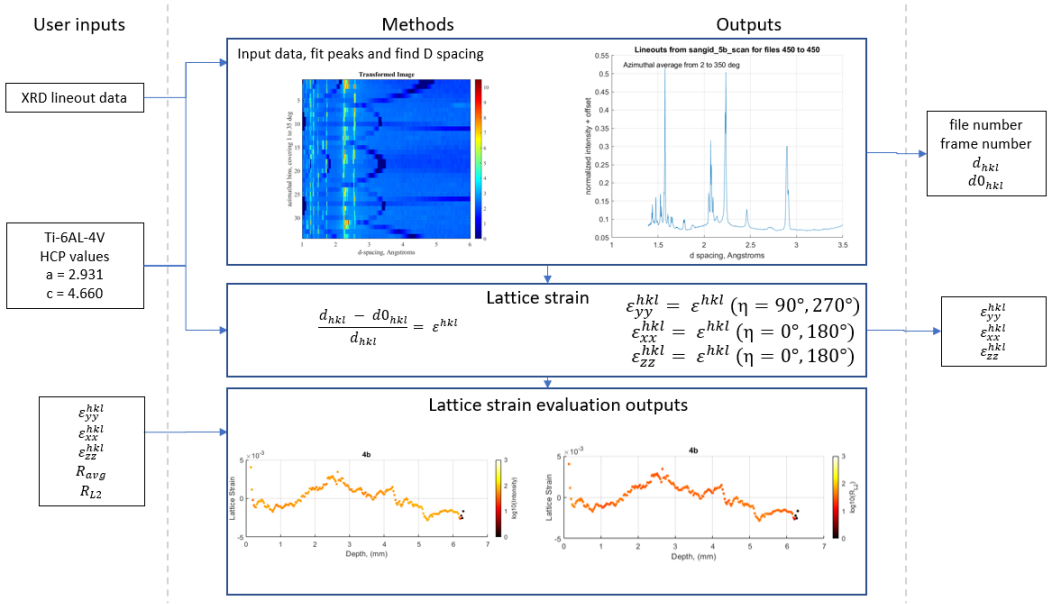

Figure 4.1. XRD method

Previous research [40] utilized EDD conducted at Argonne Lab in an attempt to gain an understanding of the residual stress within the two specimens identified in the earlier paragraph. Whilst this technique has been successful in the past research in quantifying the lattice strain and residual stress in materials [39][56], in this case there was an observed lack of resultant intensity from the diffraction patterns. A coarse grain structure was suspected as the cause of this, with this supported by BSE imaging conducted on both the As-clad and PHT repair sections of the specimens, in addition to the underlying substrate regions. Whist reducing the area of the scan size produced some improvement, a lack of consistency amongst the diffraction peaks meant that lattice strain, and therefore residual stress, could not be determined. The application of another High Energy X-ray Diffraction (HEXD) X-Ray diffraction technique with a higher resolution could provide better results, with a better resolution in the diffraction scans required due to the course microstructure within

the specimens. This research utilized HEXD experiments conducted at Argonne National Laboratory by Jun-Sang Park in June 2020.

4.1.2 Experiment Setup

The non-destructive inspection technique utilized in this research is HEXD powder diffraction analysis. As the goal of this experiment is to evaluate the residual stress within the specimens, they will not be loaded during the scans. The orientation of the specimen whilst undergoing this technique is as shown in figure 4.2, with the HEXD source originating in the z direction, causing X-ray diffraction and providing lattice spacing from the free surface through the depth of the specimen in the x direction. For this research the diffraction patterns from both specimens were captured by a Pilatus detector placed 1476mm from the specimen with a size of 2048 x 2048 pixels.

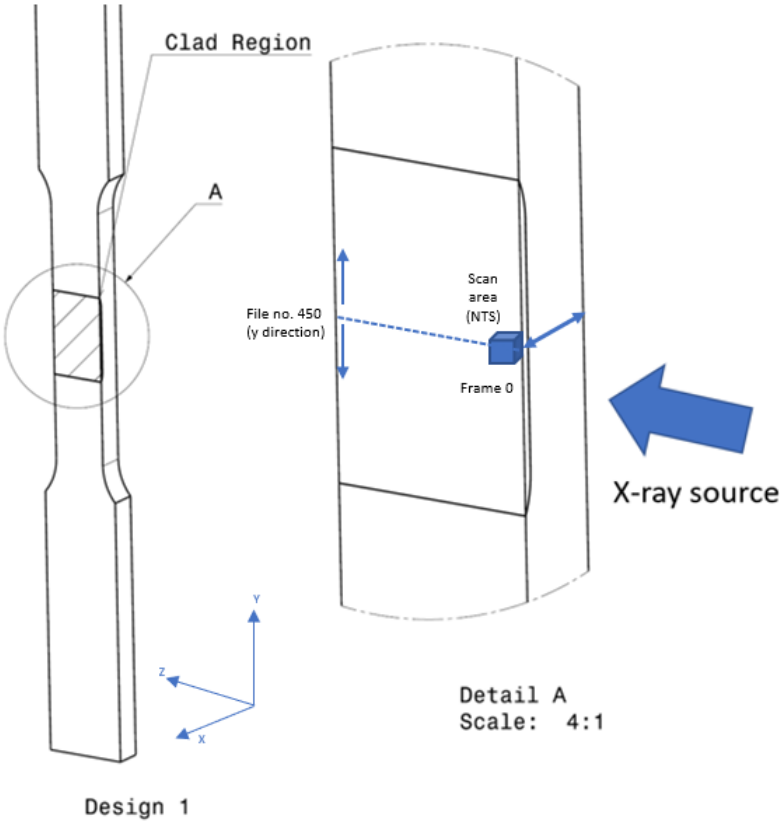

Figure 4.2. XRD scan method

Considering the research goals of these specimens, the region of interest for the HEXD scans were limited to the vicinity of the clad repair as identified in figure 3.1 and the substrate through the depth of the specimen. The area used for clamping during the fatigue test was not judged as significant for evaluating the performance of the repair and examine the influence of heat treatment post-repair, with a beam energy of 76.186 keV and size of 30 x 30 μm.

4.1.3 Post-experiment Analysis

Post-experiment analysis of the HEXD data relies on obtaining the lattice strain from the sample through a peak fitting method. A Matlab program used in previous research [57] was utilised for visualization of the {hkl} diffraction peaks of the specimen with peak fitting utilized to evaluate d_{hkl} through the use of Bragg's Law. This program was modified to accept data from the new Argonne Pilatus detector data format and to collect data through the depth of the specimen with multiple y positions.

To calibrate the equipment setup, a Ceria (CeO_2) specimen was loaded into the experiment frame, with HEXD scans conducted of the test sample. As the material properties of this specimen are known, the accuracy of the experiment can be verified [34][58]. A review of the CeO_2 diffraction peaks suggested a good level of accuracy between the theoretical and observed diffraction peaks. As another method of calibrating the scans, CeO_2 paste was also added to the Ti-6Al-4V specimens so a calibration can be conducted within the actual scans on the mounted clad repair specimens. However, this was not able to be evaluated alongside the Ti-6AL-4V specimen, with the first 8 line-outs in every scan returning unusable data.

As identified in figure 4.1, a visualization within the Matlab program of the intensity from the detector was conducted for both specimens, with the azimuth angle (η) vs d-spacing for each scan plotted as shown in figure 4.3. There were some variance observed between the As-clad and PHT specimens at different azimuth positions within the region of interest, indicating varying lattice strain within the repaired material that were captured by the detector. However, overall there were significant gaps within the data where the grains

within the material did not return a diffraction pattern with previous research utilizing Ti specimens evaluating more complete diffraction patterns [34].

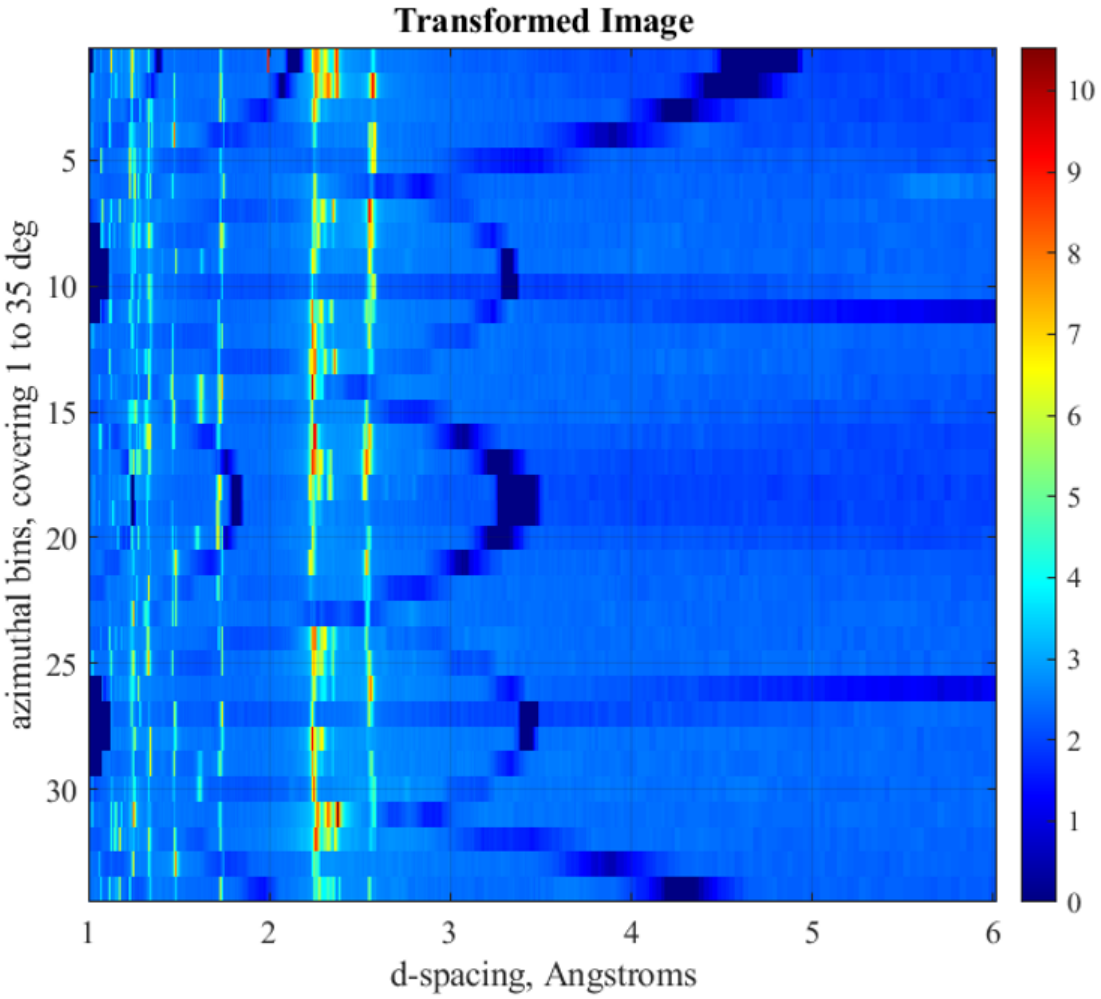

Figure 4.3. Intensity from As-clad specimen

Visualization of the diffraction rings was achieved through utilization of viewing the lineouts from each data point and comparing against the known crystallographic planes for Ti-6Al-4V. However, the diffraction rings observed were less clear and consistent than what has been detected from other research with different Ti specimens [34][58]. For each scan, summed across the entire azimuth direction, η, the diffraction peaks were available for visual analysis. An example of this is provided at figures 4.4 and 4.5 with relevant {hkl} α peaks observed, with each peak referenced against Table 4.1. Identification of d_0 for Ti-

6Al-4V is provided by the expression in equation 4.1 [33], with a and c values of 2.930 and 4.6844 utilized respectively [39]. Upon a visual review the first, third, fourth, fifth, sixth and eleventh α peaks for Ti-6AL-4V were clearly identified. Other remaining peaks were not identified clearly, with other β peak interactions and a scatter within the diffraction patterns contributing to a lack of clarity compared to what is seen in literature. Due to these initial results, post-processing of the scan data was conducted for initially the first four α peaks to limit processing time, with only the third α peak found to provide consistent results within the repair region. This behavior was similar to what was found in previous research [40]. Due to these results, the third peak was selected for further analysis only.

$$\frac{1}{d_0^2} = \frac{4}{3}\left(\frac{h^2 + hk + K^2}{a^2}\right) + \frac{l^2}{c^2} \tag{4.1}$$

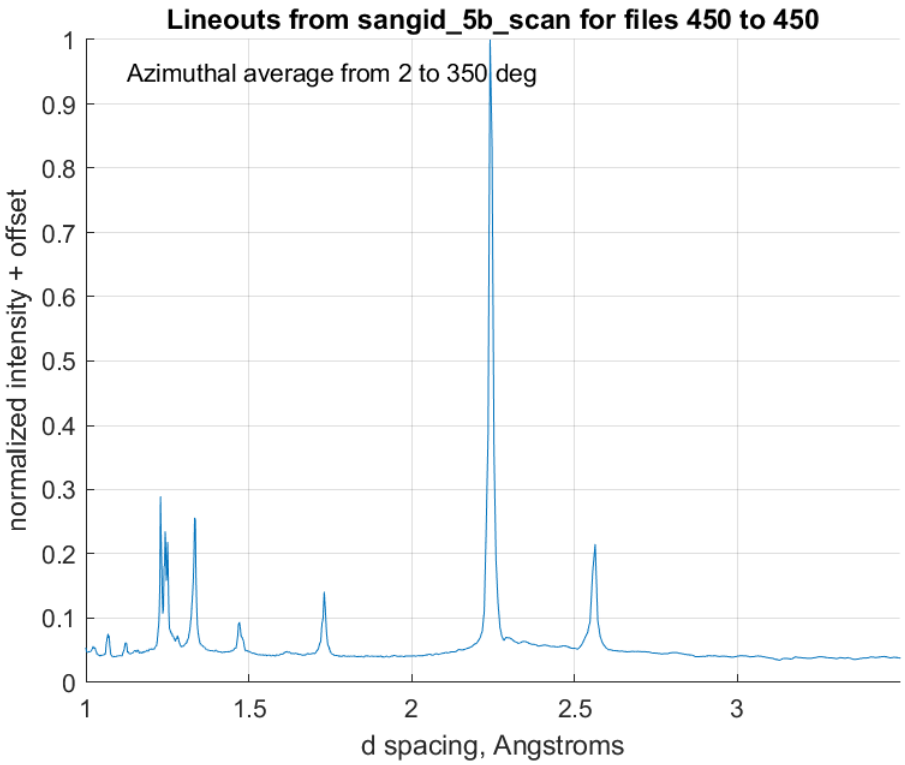

Figure 4.4. Sample Ti-6AL-4V lineout

As stated above, this analysis will only review the third Ti-6Al-4V peak with no rotation or load applied to the specimen. Equation 2.2 will be utilized with the deformed lattice

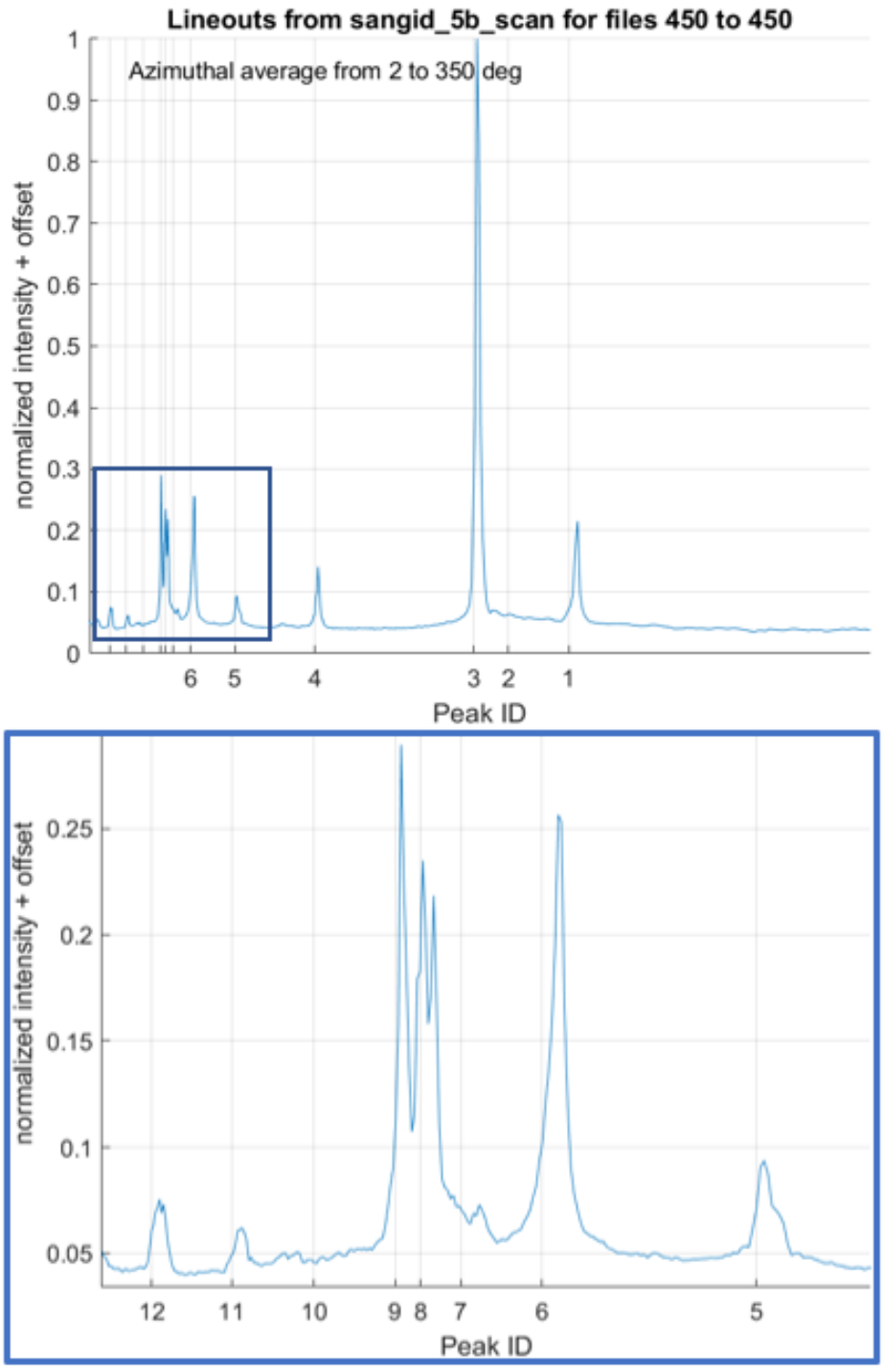

Figure 4.5. Ti-6AL-4V lineout featuring peak ID

Table 4.1. Description of Ti-6AL-4V alpha peaks

Peak	h	k	l	d0(Å)
1	0	1	0	2.54
2	0	0	2	2.34
3	0	1	1	2.23
4	0	1	2	1.72
5	1	1	0	1.47
6	0	1	3	1.33
7	0	2	0	1.27
8	1	1	2	1.24
9	0	2	1	1.23
10	0	0	4	1.17
11	2	0	2	1.12
12	1	0	4	1.06

spacing at d_{hkl} differing from the d_0 due to the presence of residual stress within the material. Previous research featured the application of summed data from the detector across a loaded and rotated specimen [57][58]. Whilst these parameters were not required for this research, their methodologies were followed to obtain lineouts from the Debye-Scherrer rings from the detector integrated over $\eta = \pm 5°$ diffraction ring positions of 90° and 270° for the loading (y) direction, with the 0° and 180° corresponding to the transverse direction relating to figure 4.2. With the range of η specified above, this corresponds to an output summing the data between the angles of 85-95° and 265-275° respectively. The output of the Matlab program exported d_{hkl} for these directions, but was also modified to include the intensity and residual values to allow further analysis.

The residual of the peak fitting was evaluated within the Matlab program by comparing the calculated, or theoretical amplitude, and the observed amplitude from the experiment data. A visual representation of this relationship is shown in figure 4.6 with raw data included from the experiment.

The residual is utilized as a measure of how the experimental data compares to the review of intensity conducted at each peak to make sure it fits the residual value, R, with good matches following from low R values. A high R value reveals the experimental data points that are being interpreted may not be a good match to the expected calculated data.

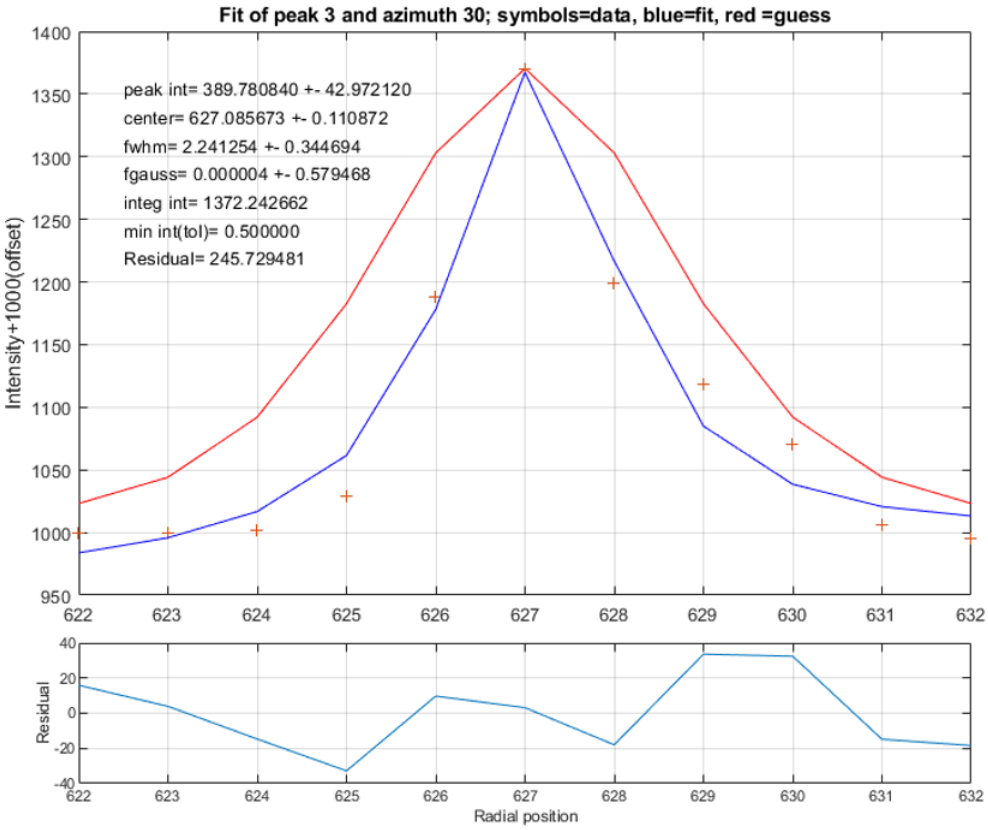

Figure 4.6. Residual example from As-clad specimen

Residual calculations that were applied in this research were conducted utilizing the Matlab mean and norm functions of the following expression:

$$R = \mid y_{calc} - y_{obs} \mid \tag{4.2}$$

4.1.4 Lattice Strain Calculations

As identified in the literature review, the lattice elastic strain within the material can be evaluated through the application of Bragg's law at equation 2.1 to evaluate the the change in lattice spacing when compared to the strain-free lattice spacing [29][59]. Whilst a significant body of work has been conducted in comparing the lattice strain of a loaded sample, and scans of the specimen taken when unloaded to obtain the strain-free lattice spacing, as this research features specimens which are not loaded a different technique will

be used. Instead the lattice strain will be evaluated against the strain-free lattice evaluated through material constants. This method was utilized to obtain the strain-free lattice for the EDD scans previously conducted on these specimens [40]. Equation 2.2 was utilized to obtain the lattice elastic strain for both specimens.

A separate Matlab script was created to take the data outputs from the previous Matlab program to evaluate the lattice strain and utilize the intensity and residual values at each data point. A filter was applied to the d_{hkl} data which featured a credible magnitude of d_{hkl} values. This result was an indication that the diffraction peak could be accurately fitted. For each data point, equation 2.2 and d_0 were utilized to calculate the lattice strain with respect to the distance from the free surface. The residual value for each data point was added to the lattice strain plots as a color bar, allowing for a visual representation of the quality of fit for each data point. As the height of the specimen corresponds to the numbered name file of each scan, an evaluation of the lattice strain at each location can be quickly completed.

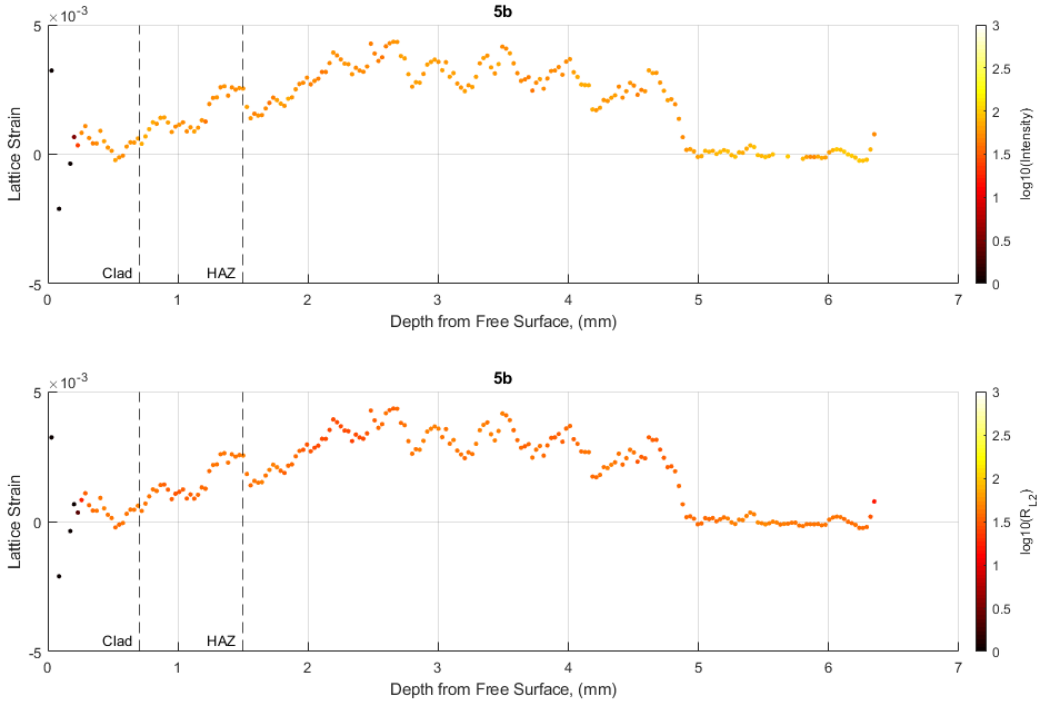

Figure 4.7. Lattice strain for As-clad specimen

The lattice strain was computed for each file, or each scan at a particular y position utilizing the axis from figure 4.2. To aid in interpretation of the lattice strain figures the peak intensity and norm residual, denoted as R_{L2}, corresponding to each data point were added as color bars to the lattice strain plots. However, when plotting the results of a scan at a single y position throughout the depth of the specimen, a significant amount of scatter was observed with no distinguishing pattern between the data points. To establish a more consistent lattice strain pattern that we would expect from the material, a sum of every lattice strain value at each depth position was taken. As observed in figures 4.7 and 4.8, this method significantly reduced the scatter of a single y position, with a smoother behavior observed in the lattice strain throughout the depth of the specimen.

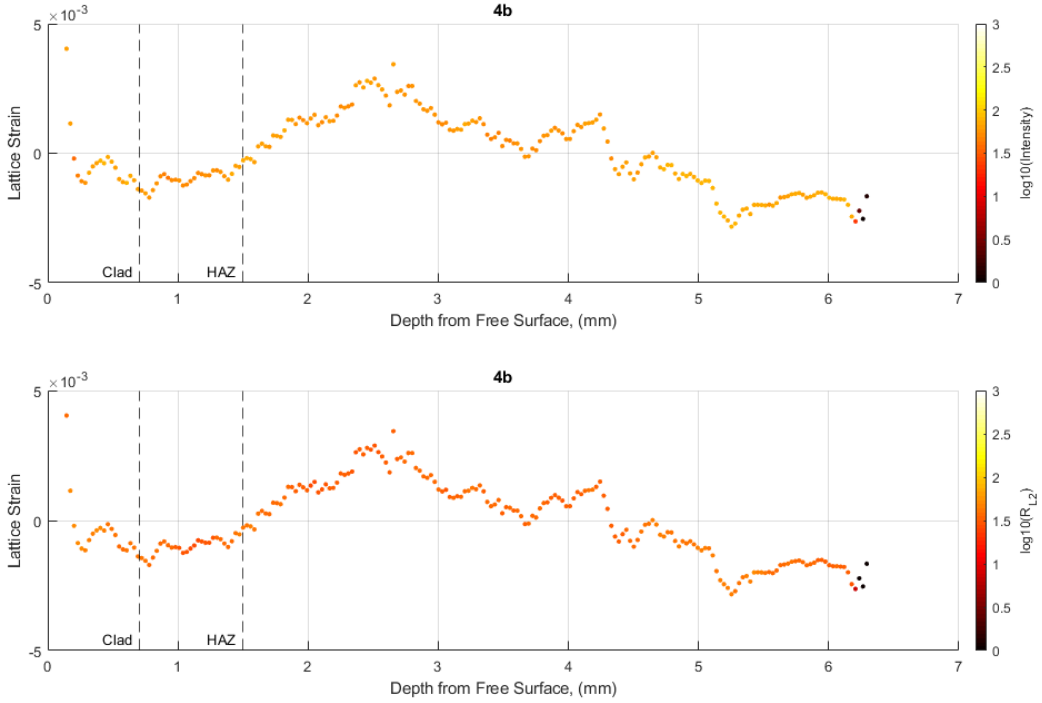

Figure 4.8. Lattice strain for PHT specimen

The magnitude of the lattice strain is observed to be higher for the 5b (As-clad) specimen in comparison to the 4b (PHT) specimen, for both the thickness of the repair (0 - 0.7mm) and into the depth of the substrate.The literature review identified some deficiencies with the accuracy of destructive inspection techniques very close to the surface of the specimen

[29]. Whilst this methodology offers a comparison between the two specimen types, the lattice strain identified in figures 4.7 and 4.8 show values that have a very low intensity and residual value, suggesting the quality of fit is low.

4.2 Slitting

4.2.1 Experiment Setup

A destructive residual stress measurement method was chosen to allow a comparison to the HEXD non-destructive method. The slitting method was chosen due to its ability to measure residual stress in one direction at very close intervals, when compared to the contour method. Whilst the contour method provides a better overall residual stress distribution, and has been used to evaluate residual stress in similar AMe repair research [10], the higher resolution of measurements available to slitting was judged to be of more benefit to this research. Utilizing the orientation of figure 4.9, this destructive method will measure the residual stress of each clad repair in the y direction through the thickness of the sample.

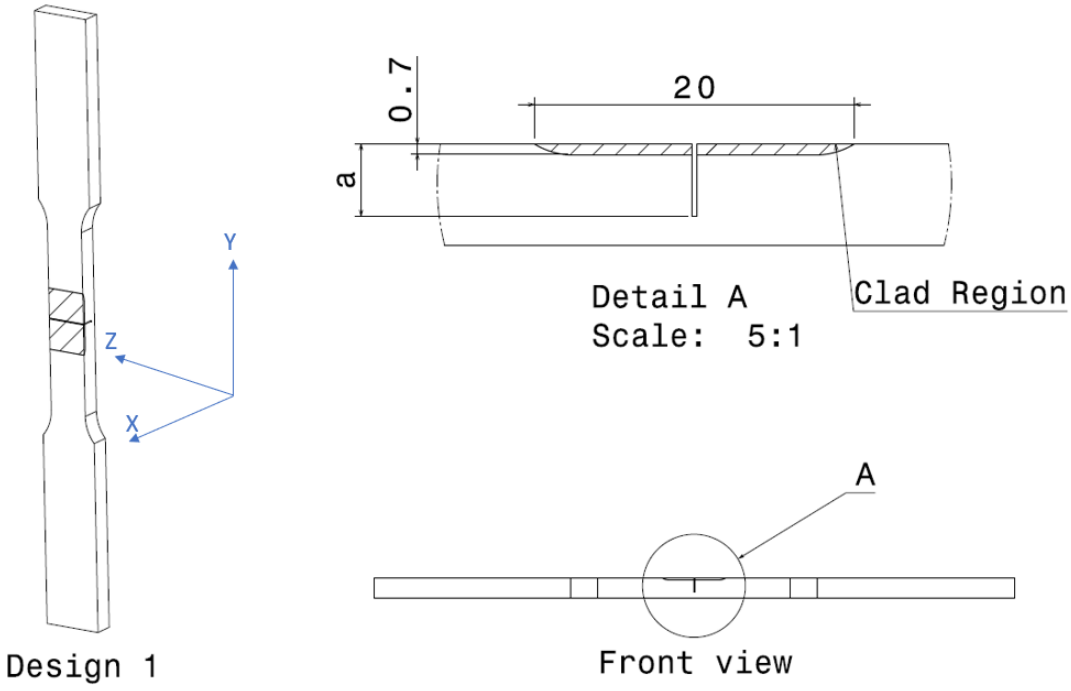

Figure 4.9. Slitting orientation

The slitting was conducted at Hill Engineering, CA, with both the 5B (As-clad) and 4B (PHT) specimens undergoing the destructive method on the completion of the HEXD scans at Argonne National Laboratory. In a similar manner to the HEXD scans, the gauge region was selected as 20mm long, with the slitting performed at the center of the gauge section, with a slight off-set from the center notches that were pre-machined into the clad material as a design 1.

The slitting method has seen extensive use in residual stress applications [29][32][36][60]. Once each specimen is fitted with a strain gauge, the incremental slit of depth a, as shown in figure 4.9 with dimensions in mm, is cut into each specimen up to 5mm into the depth of the specimen as measured from the free surface. The total depth of the cut reveals a remaining ligament of 1.35mm. The deformation caused by the release of residual stress within the material from each incremental cut is measured by the strain gauge. Once the readings from the incremental slit depth are taken, a finite element model is utilized to evaluate the residual stress through the depth of the specimen.

4.2.2 Slitting Results

The results of the slitting technique were provided by Hill Engineering and shown in figure 4.10, with the uncertainty of each measurement also displayed. The slitting technique detected residual stress in compression at the free surface and somewhat into the depth of the clad repair. This was not initially expected, as identified in the literature review, laser clad depositions feature tensile residual stress at the completion of the process. Research from RMIT featured similar specimens with a laser clad repair application utilized the contour method to detect a region of tensile residual stress at the free surface and extending into the depth of the specimen [10]. However, one of the key differences between the RMIT specimens and the specimens within this body of work is that all specimen configurations within this body of work were cut from a piece of Ti-6AL-4V material and machined after the application clad repair. The RMIT specimens were not machined post-deposition.

The slitting results highlighted differing magnitudes of residual stress between the As-clad and PHT specimens. This outcome is expected, with the application of heat treatment

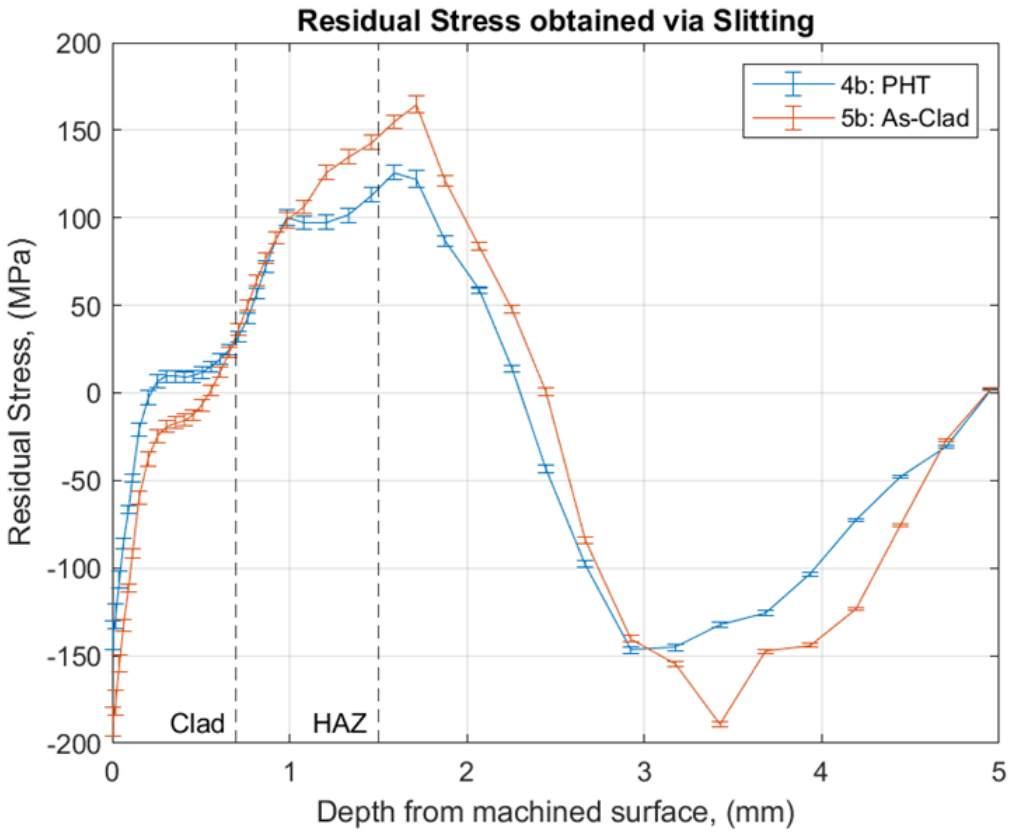

Figure 4.10. Slitting results

to the 4B reducing the magnitude of the residual stress. This behavior begins at the free surface and continues into the depth of the specimen up to the HAZ. Notably the substrate contains tensile residual stress, with this behavior reflecting an equilibrium response within the specimen.

5. FATIGUE TESTING

5.1 Experimental Setup

An MTS tensile load frame in the Advanced Computational Materials and Experimental Evaluation laboratory at Purdue University was utilized for fatigue testing of the specimens until failure. The specifications of the load frame are detailed in table 5.1. The fatigue test is utilized to cause fracture of the specimens, allowing the application of quantitative fractography to evaluate the fatigue crack growth rate of the As-clad and PHT repaired material, in addition to a baseline Ti-6AL-4V material.

Table 5.1. Fatigue test equipment

Name	Model	Rating (kN)
Load Frame	MTS 632.41B-01	50
Force transducer	MTS 661.20E-03	100
Hydraulic Grips	MTS 647.10	100
Force Alignment cell	MTS 609.10	100
Hydraulic Actuator	MTS 244.12	25

The load frame was assembled, calibrated and tested through efforts in previous research [40] in which the load cell and grips were changed. A re-calibration was conducted to examine the bending upon application of the tensile load. This calibration as conducted prior to the first test of a design 1 specimen. Re-calibration was conducted in accordance with ASTM E1012 [61] with strain gauges in a Wheatstone Bridge configuration were attached to a steel test sample, with steel chosen due to its similar mechanical properties to Titanium [40]. Deformation experienced within the specimen as it undergoes a calibration testing regime is detected through resistance changes within each strain gauge. This methodology is further detailed in ASTM guidelines [61]. Bending moments below 3.85 % were achieved through this method [40].

As discussed in the literature review, through the application of loading sequence at different stress ratio (R) values, MBs can be produced on the fracture surface [28][53]. An example loading sequence shown in figure 5.1 [40], with the M1 and M2 two sequential

and repeating groups of cycles with a higher minimum applied stress to the tensile fatigue loading.

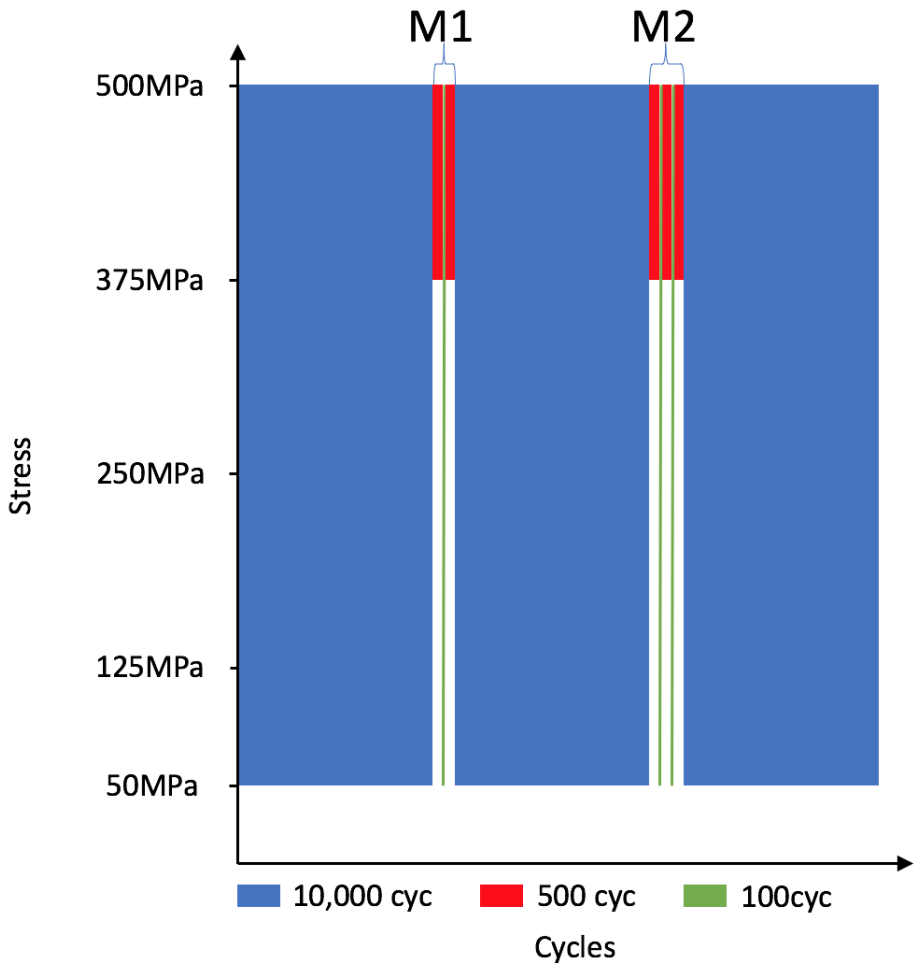

Figure 5.1. Example marker band loading sequence [40]

As the number of cycles between the different R loads is established through the fatigue test, by measuring the distance on a fracture surface between the MBss the material fatigue crack growth rate can be determined. This technique has been used in previous research by Defence Science and Technology Group (DSTG) [28], with the applied loading in this fatigue experiment based on a previous research methodology [40] as detailed in tables 5.2 and 5.3. Utilizing the 25 kN maximum load of the actuator with the cross-section of the gauge area of 8.5 x 6.35 mm produces a maximum stress of approximately 460 MPa at the specimen gauge,

which also features the location of the laser clad repair. Failure of the design 1 configuration is predicted at 99,663 cycles [40].

Table 5.2. Baseline specimen loading sequence

Segment	Cycles	Load (MPa)	R
M1	10000	46 - 460	0.1
M1	500	347.5 - 460	0.75
M1	100	46 - 460	0.1
M1	500	347.5 - 460	0.75
M2	10000	46 - 460	0.1
M2	500	347.5 - 456	0.75
M2	100	46 - 456	0.1
M2	500	347.5 - 456	0.75
M2	100	46 - 460	0.1
M2	500	347.5 - 460	0.75

Table 5.3. Clad repaired specimen loading sequence

Segment	Cycles	Load (MPa)	R
M1	5000	46 - 460	0.1
M1	500	347.5 - 460	0.75
M1	100	46 - 460	0.1
M1	500	347.5 - 460	0.75
M2	500	46 - 460	0.1
M1	5000	46 - 460	0.1
M2	500	347.5 - 460	0.75
M2	100	46 - 460	0.1
M2	500	347.5 - 460	0.75
M2	100	46 - 460	0.1
M2	500	347.5 - 460	0.75

A sensitivity and frequency analysis was also conducted through previous research [40] to determine the optimum frequency of the fatigue test. This was determined through application of a Mean Square Error (MSE) percentage between the commanded load from the load frame and measured load from a Ti-6Al-4V test specimen. A careful selection of

the test frequency is required to minimize the error between commanded and measured load, whilst also reducing the time taken for the fatigue tests to be completed.

$$MSE = \frac{1}{N}\Sigma(F_{actual} - F_{commanded})^2 \tag{5.1}$$

$$MSE\% = \frac{MSE}{F_{commanded}} \tag{5.2}$$

Tests were conducted across a number of frequencies with a sample fatigue test utilizing the one test specimen to quantify how accurately the load frame could apply the desired loads to the test specimens within the fatigue test. The results of various frequency selections were graphed against a percentage of the MSE from equation 5.2 for commanded and measured loads, with a frequency of 3 Hz selected by previous research to be the best fit between remaining error and the expected duration of the fatigue test [40].

The MTS software Multipurpose Elite (MPE) was used to control the fatigue experiment and apply the required loads in tables 5.2 and 5.3 to each specimen. Two parallel processes were utilized, as shown in figure 5.2, with the application of the constant amplitude loading at the specified frequency and a data acquisition process to record the applied force to the specimen, displacement and the number of cycles applied during the test. Whilst the number of cycles is programmed into the test, this data acquisition method is required to verify the loading sequence is correct and to capture the number of cycles until specimen failure.

An Allied Vision Manta G-201B camera with Mitutoyo 10X or 20X optical lens was used to observe and record any crack initiation and growth observed at the notches, with the setup shown in figure 5.3. The successful identification of the crack initiation location would aide in future fractography work as knowing the location of crack initiation would help in tracking the progression of MBs on the fracture surface.

To capture any crack growth at the notches, the MPE test run was programmed to run in a semi-autonomous manner with the application of an M1 or M2 cycle as shown in figure 5.1, or a combined sequence of M1 and M2 segments, to completion and then unload the specimen. Once this sequence had ended the maximum load was applied manually to the specimen through the MTS Station Manager software. At this load of 22 kN the notches

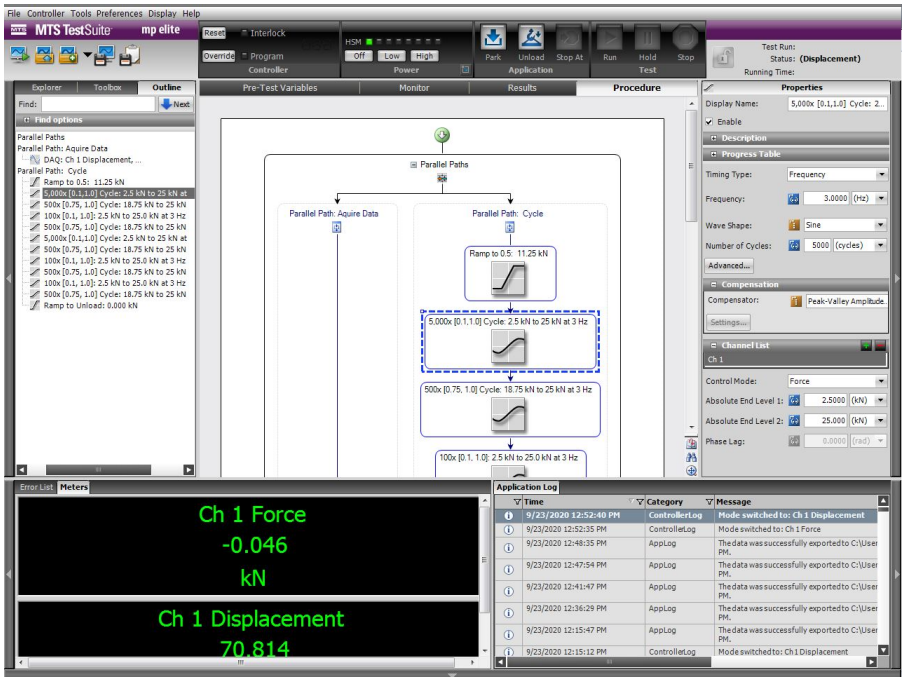

Figure 5.2. MPE software for clad specimens

were visually scanned through the camera for evidence of crack initiation or propagation. Once any relevant images had been captured, the specimen was unloaded through the MTS Station Manager software and the test was resumed in the MPE software. This process was repeated until specimen failure.

5.2 Specimen Design Revisions

Previous research had encountered problems in initiating cracks in the notch region, which allows for tracking of the crack growth within the specimen during the fatigue test [40]. Of six specimens tested, only one failed within the notch region, with four of the six failing within the gauge region which was exposed to the laser clad repair. The other two specimens failed at the transition between the gauge region and the neck of the specimen leading to the grip area. Whilst previous research was able to detect and characterize maker bands in a sample that had not failed at the notch [40], this progression did not occur in the clad region. Due to the thin thickness of the laser clad deposition, selected to model

Figure 5.3. Camera configuration with 10x optical lens

a typical repair application to an aircraft, crack initiation at the notch is required for this research to ensure the fatigue crack growth rate at the laser clad region can be measured.

Specimen 1A was re-machined to the design 3.1 specification to further encourage failure in the notch region. The loading sequence was not changed from previous research so that an effective comparison could be maintained between specimen designs and previous research results [40]. Whilst the greater number of notches increased the time taken to capture images of the notches, this did not significantly influence the time taken to complete the fatigue test overall. However, the outcome of the test of design 3.1 was ultimately not successful. Failure occurred outside of the gauge at the rear of the specimen after 562,026 cycles, on the opposite side to the laser clad area as shown in figure 5.4. Images were taken of the notches when appropriate to detect any crack initiation until specimen failure, however throughout the test there was no observed crack initiation or growth observed in either the three original notches or the two new notches.

From a visual review of the specimen, crack initiation occurred at the transition between the clad region and the remainder of the specimen which had been exposed to the shot-peen application. As this is a laser clad sample, the interactions between the residual stresses from machining the surface of the specimens post-repair and at the surface of the shot-peen surface can act as a stress concentration and source of crack initiation. As this occurred

Figure 5.4. Failure of design 3.1

away from the notches designed to cause crack initiation within the clad region, the shot peen application in design 3.1 failed to delay crack initiation away from the clad region. This failure demonstrated the need for another design revision to further encourage crack initiation in the laser clad region.

Once design 3.2 was implemented across the remaining specimens fatigue testing was completed on each specimen until failure. The same load sequence was retained as in previous tests, as the dimensions are the same as previous designs, therefore the same stress was applied to the specimen gauge. In a similar manner to the previous specimen design iterations, images were taken of the notches when appropriate to determine any crack initiation until specimen failure.

Figure 5.5. Failure of design 3.2

Of the seven remaining specimens configured to design 3.2, four featured crack initiation and failure at the notch region, a significant improvement over previous design iterations. All of these failures occurred at the middle notch, as shown in figure 5.5, with no crack initiation detected in the other two notches. Whilst the sample size between all designs is small, it appears this design provides better reliability than the previous designs. Of importance to the aims of this research, one of each specimen type (baseline, As-clad and PHT) experienced failure with crack initiation commencing within the clad region, ensuring quantitative fractography can be utilized to detect and measure marker bands in the clad region.

5.3 Fatigue Testing Results

A PHT specimen, 2A, was the first of the revised 3.2 designs to be tested. Failure occurred at 581,089 cycles, however crack initiation did not commence within the clad region. This specimen did not provide any useful fractography information. Crack initiation was visually detected on the free surface of a 7B baseline specimen, with cracks observed to be propagating on the surface until failure occurred at 231124 cycles. This progression is detailed in figure 5.6. The shape of the crack is drawn in-between applied fatigue testing cycles at figure 5.6 to show progression to failure. The image used for this figure was taken at 222,862 cycles, which was the image captured prior to specimen failure.

No cracking was detected on the free surface throughout the testing of sample 4A, an As-clad sample, however a crack developed at the slot within the clad region and propagated into the depth of the specimen. Close to failure, an elongation of the slot was observed, with fracture occurring at 143,653 cycles.

Multiple cracks were detected on the free surface of the 3B PHT specimen. However, whilst failure occurred at the slot location at 391,226 cycles, the exact eventual fracture location was not identified during the fatigue test. This failure is likely similar to 4A where the crack progressed through the depth of the specimen, commencing at the slot within the clad region. Specimens 5A, a baseline, and 8B, an As-Clad, did not feature crack initiation and failure at the notch areas and did not contribute to any valuable fractography data. 9A,

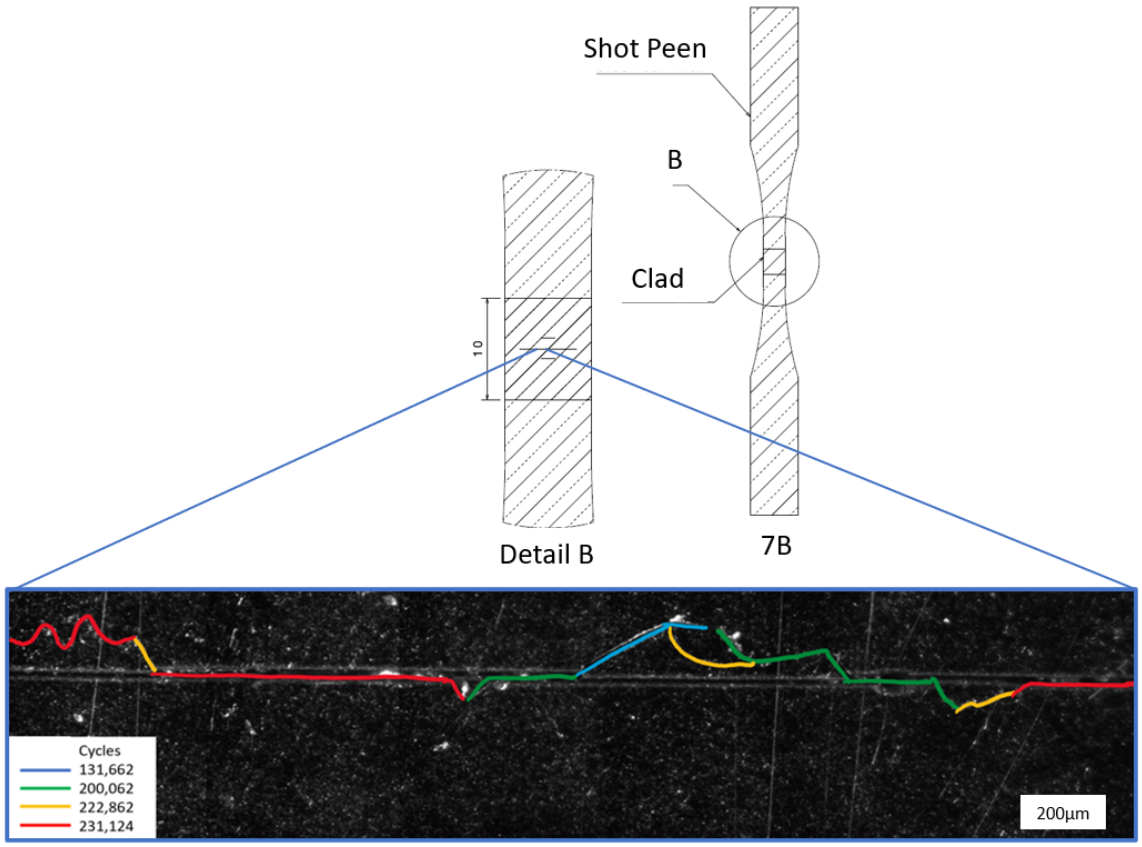

Figure 5.6. 7B baseline crack progression

a PHT sample featured a unique failure in the notch region. The right side of the sample saw significant deformation of the slot region, suggesting initiation occurred on the left side. However, no MBs were detected in this sample and as such it was not able to provide effective fractography data in support of the aims of this research.

A stress-life output of all specimens tested is presented in figure 5.7, with the total cycles to failure shown for every sample and design that underwent tensile fatigue testing. The cross-sectional area was taken at the failure location for each sample, outlining specimens such as 1B and 5A which failed in the specimen shoulder, beyond the gauge region which featured the clad repair.

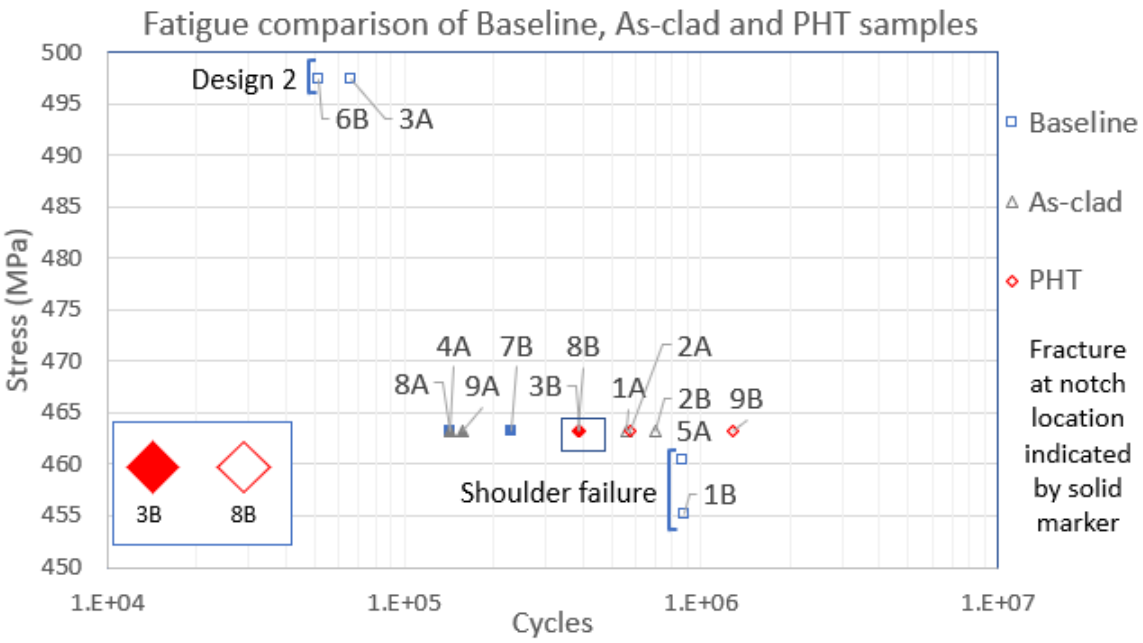

Figure 5.7. Fatigue comparison of baseline, As-clad and PHT samples

6. FRACTOGRAPHY

Fractography seeks to study the features of a fracture surface to determine the mechanisms of failure [62]. As detailed in the literature review, the application of QF can determine fatigue crack growth through measurements on the fracture surface [28][51][52][53][62]. This chapter will outline the QF method used to identify and measure the MBs on the fracture surface. The application of these measurements will characterize the fatigue crack growth rate on the fracture surface of the clad, HAZ and substrate regions of the test specimens. This will allow an evaluation of the repair performance of the As-clad vs PHT material.

6.1 Equipment

An Olympus BX51M optical microscope was initially utilized to view the fractography surface and to attempt to detect MBs, in a similar manner to previous research [40]. As detailed in the literature review, optical microscopes are a common method for viewing the fracture surface and detecting features to assist in QF [28]. However, previous research on these same specimens found the use of an optical microscope challenging due to the tortuous fracture surface of the titanium samples [40]. The short focal length of the optical microscope utilized proved difficult to detect MBs as the focus had to be continually re-adjusted when performing scans of the fracture surface. An example of this is displayed in figure 6.1, with a notch seen at the top of the image. Notably, there is a loss of focus across even this relatively flat fracture surface.

To improve the quality of the optical microscope images, previous research utilized image stacking to compile multiple images at different focal lengths to a single image, as seen in figure 6.2 [40]. This technique achieved some success in obtaining optical microscope images which could effectively show MBs on the fracture surface. However, the use of image stacking requires the location of the MBs to be already identified at high zoom. Utilizing the optical microscope to identify MBs is still severely limited by the short focal length of the optical microscope.

The application of this technique across all failed samples which did not feature crack initiation at the notch region would be particularly challenging. Searching a large portion

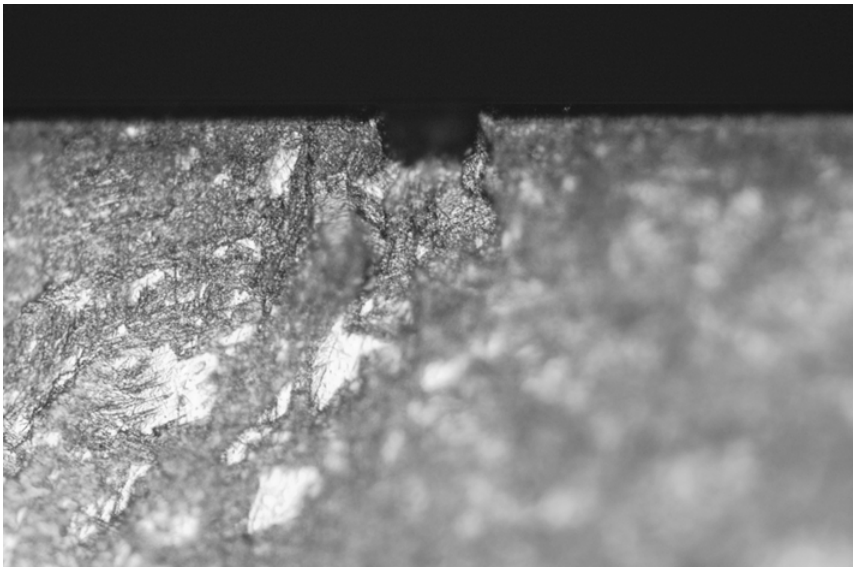

Figure 6.1. Optical microscope with a short focal length

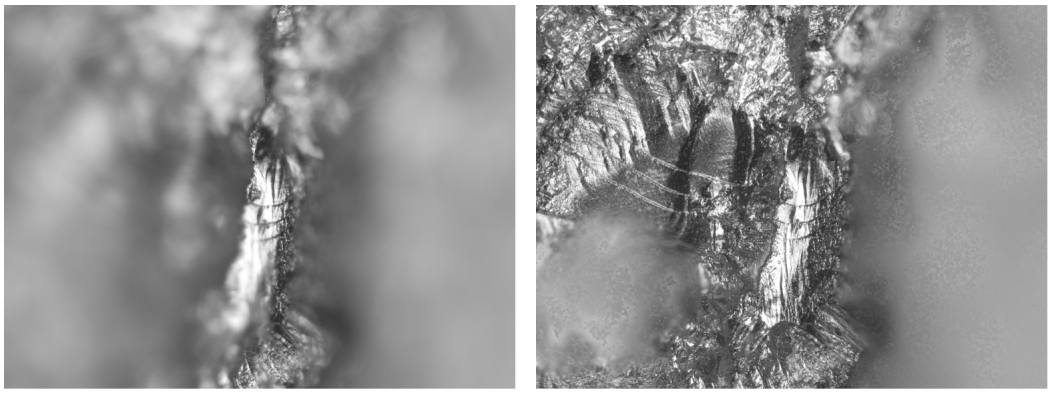

Figure 6.2. (a) live optical image (b) 100 images stacked [40]

of the fracture surface with a short focal length would be incredibly time consuming. Ultimately, the image stacking technique was considered to be too time intensive towards the goal of identifying and measuring MBss across the fracture surface.

Previous research also utilized a FEI Nova NanoSEM in identifying and measuring MBs on the fracture surface [40]. Manual scans of the fracture surface at high zoom were conducted with success achieved with identifying and measuring MBs on the fracture surface. This validated the QF technique from the literature review. However, due to inconsistent failure

locations on several samples in fatigue testing during previous research, no crack initiation occurred within the clad region propagating into the substrate.

With the improvements to the specimen design detailed in chapter three, the remaining specimens can be studied to search for an effective progression of MBs from the clad region through to the substrate. In this research, both the FEI Nova NanoSEM and Quanta 3D FEG SEM were utilized with the below settings applied as shown in Table 6.1.

Table 6.1. SEM equipment settings

Name	**Nova**	**Quanta**
Accelerating Voltage (kV)	10.0	10.0
Spot Size	5	5
Working Distance (mm)	5	10
Aperture	100	100

6.2 Fractography Surface Features

When considering the fracture surface of the specimens, figure 6.3 outlines how the orientation from the fatigue test translates into the fractography images that will be shown throughout this research. Each fracture surface which forms a half of the particular specimen is labelled “T” or “B”, corresponding to the top or bottom half of the specimen, for ease in referencing MBs on each fracture surface.

The titanium fracture surface features a tortuous topography which is consistent with the experience found in both previous research [40] and literature [52]. The slot and middle notch, features of specimens manufactured to design 3.2, were very easy to locate when failure occurred at the slot. A darker region at the top of the specimen was observed when this occurred, as shown in figure 6.4. This provided a reliable reference to commence the search for crack initiation and MBs within the clad region. For those specimens which did not feature crack initiation in these locations, locating MBs was more difficult due to a wider search area at high magnification. Due to the inconsistent nature of crack initiation from the fatigue tests, the site of crack initiation was not known at the commencement of QF.

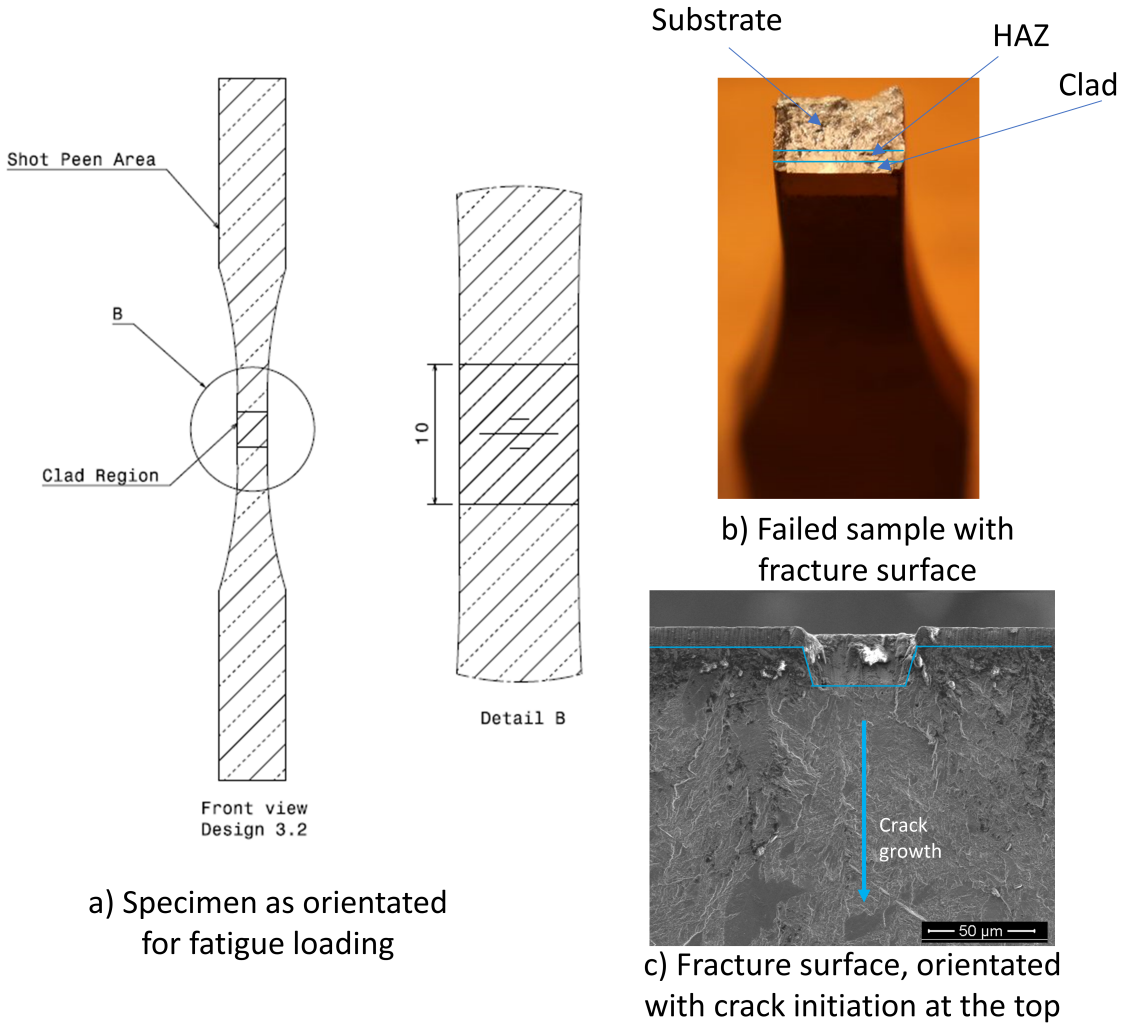

Figure 6.3. Fractography orientation

Whilst some indications could be gained visually, observation of the fracture surface under SEM was usually required to determine the crack initiation site.

The depth of the laser clad surface was measured at 0.7mm from the free surface, which matched the specification of the samples detailed in chapter 3. The transition between the laser clad material and the HAZ was clearly evident with a noticeable change from the clad region to the HAZ, with a lighter observed contrast observed in the SEM as the microstructure transitions from the fine martensitic to the lammellae structure.

The previous method of scanning a significant portion of the fracture surface to locate MBs was time consuming, particularly if the fatigue testing was unable to obtain crack

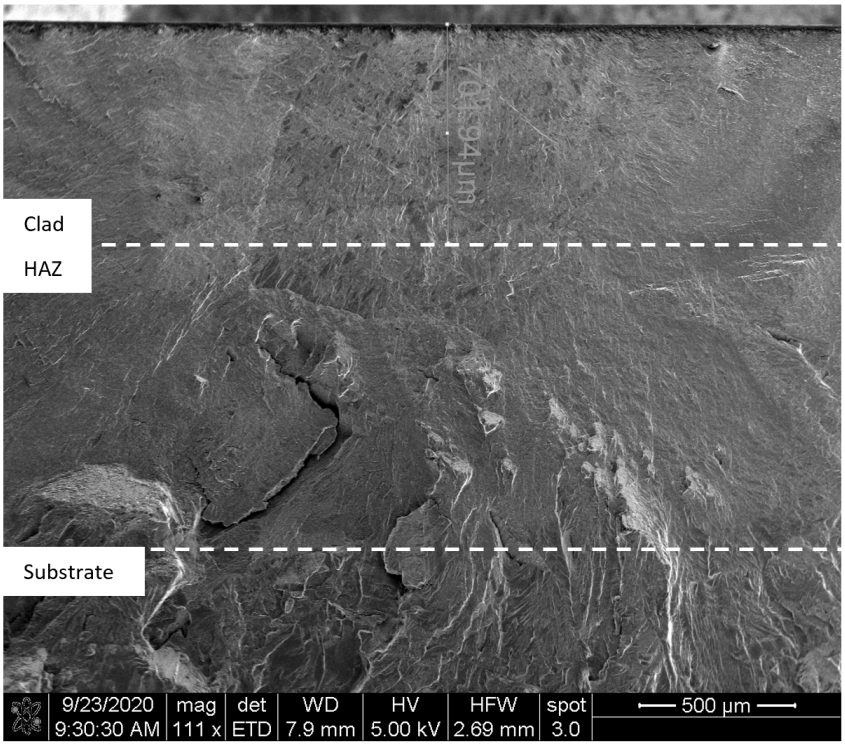

Figure 6.4. Clad, HAZ and substrate regions [40]

initiation at the notches or slot. A full scan of the majority of the fracture surface in the SEM would not be productive, with the chance of errors in detection of MBs when purely relying on continuous visual high zoom scanning. However, through the identification of common fractography features visually observed in the SEM, MB locations can be more effectively narrowed down for identification and subsequent measurement. This method was particularly useful for specimens which did not feature crack initiation in the notch region as determining the crack initiation location and then subsequent MBs is more difficult without a known initiation location. Figure 6.5 features the fractography features most often used to aide in the finding of likely MB locations.

a) Striations show the direction of fatigue crack growth. This can be used to further narrow down the crack initiation location, as any striations that are not parallel to the free surface can be back-tracked to the origin of crack initiation. b) As detailed in the literature review,MBs can be used to obtain the crack growth rate on the fracture surface. c) The different orientation of the striations in the main crack growth direction exhibit mode II

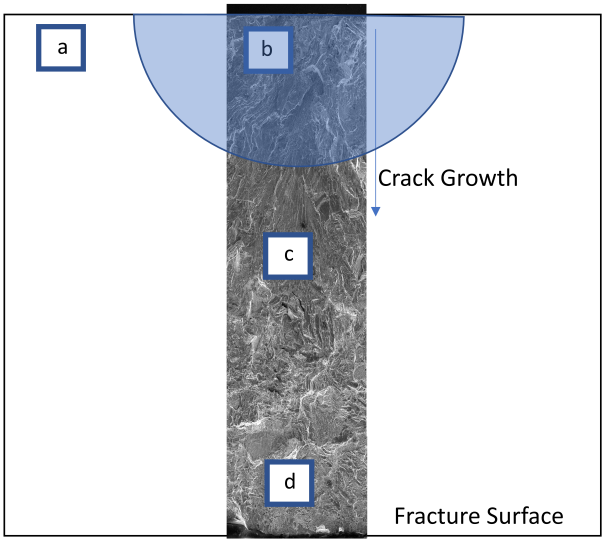

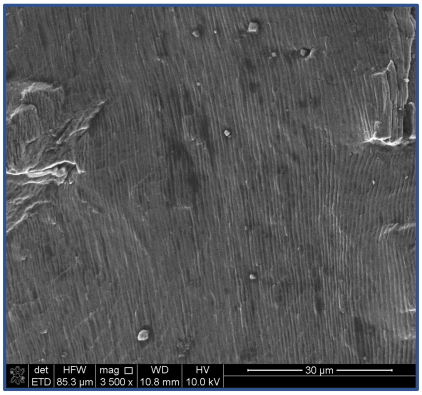

a) Striations with crack growth from initiation site

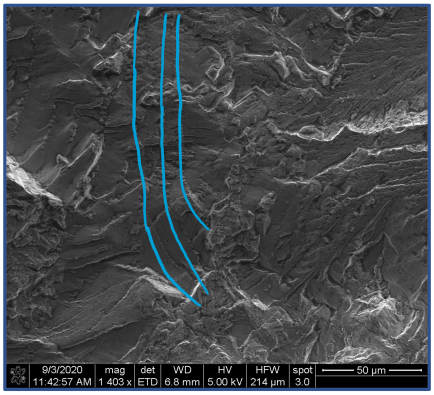

b) Marker Bands near crack initiation site

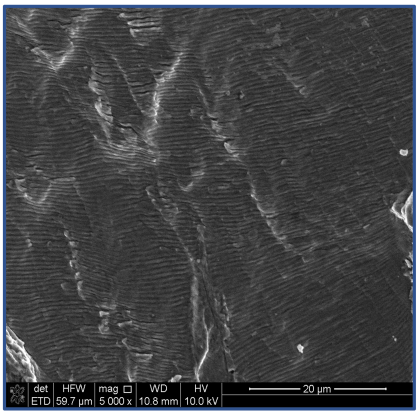

c) Striations showing crack growth away from initiation site

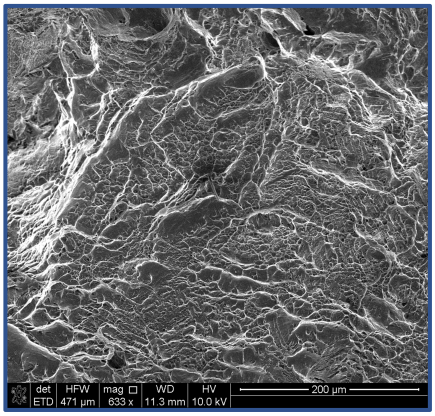

d) Dimple Rupture from fracture

Figure 6.5. Fracture surface features

crack growth, where the majority of the crack growth occurs. d) Although specimens failed through the fatigue failure mechanism, there were signs of dimple rupture on the fracture surface where the remaining material that had not experienced crack growth was overloaded, causing final failure. Dimple rupture is characterized by microvoids which nucleate at strain discontinuities such as grain boundaries, inclusions and dislocation pile-ups [33][62]. This feature on the fracture surface was used to serve as a confirmation of where the specimen ultimately failed. More importantly, crack initiation would be on the opposite side of the fracture surface, initially narrowing down the locations of crack initiation and subsequent MB progression.

6.3 Marker Band Technique

As designed, the nature of the M1 and M2 sequence detailed in tables 5.2 and 5.3 produced a pattern which, when identified and measured, can evaluate the fatigue crack growth rate at that location on the fracture surface. Figure 6.6 shows an M2 MB with three distinctive MB patterns perpendicular to the direction of crack growth. The crack growth rate is determined from visual means. Each identified MB on a sample's fracture surface had an image taken within the SEM for record keeping. The crack growth per cycle is measured by loading each MB image recorded from the SEM into Image J software. The distance between each MB, shown in figure 6.6, is evaluated through measuring the pixels within the MB image against the provided scale in the SEM image. This value is then divided by the number of cycles between each MB, as determined by the fatigue test loading sequence detailed in table 5.3. The position of the MB on the fracture surface and the distance of each MB relative to the crack initiation site, a, were determined from the SEM by moving the automated stage which the specimens were mounted to.

The stress intensity factor, ΔK_1, was calculated using equation 6.1, which represents a semicircular crack extending radially from the crack initiation site in a finite thickness specimen [44]. This is represented by the expanding blue semicircle in figure 6.7, overlaid on the fracture surface of one of one of the observed crack initiation sites. The front face correction factors, M_f and θ were selected as 1.12 and 1.571 respectively [44], with t representing the

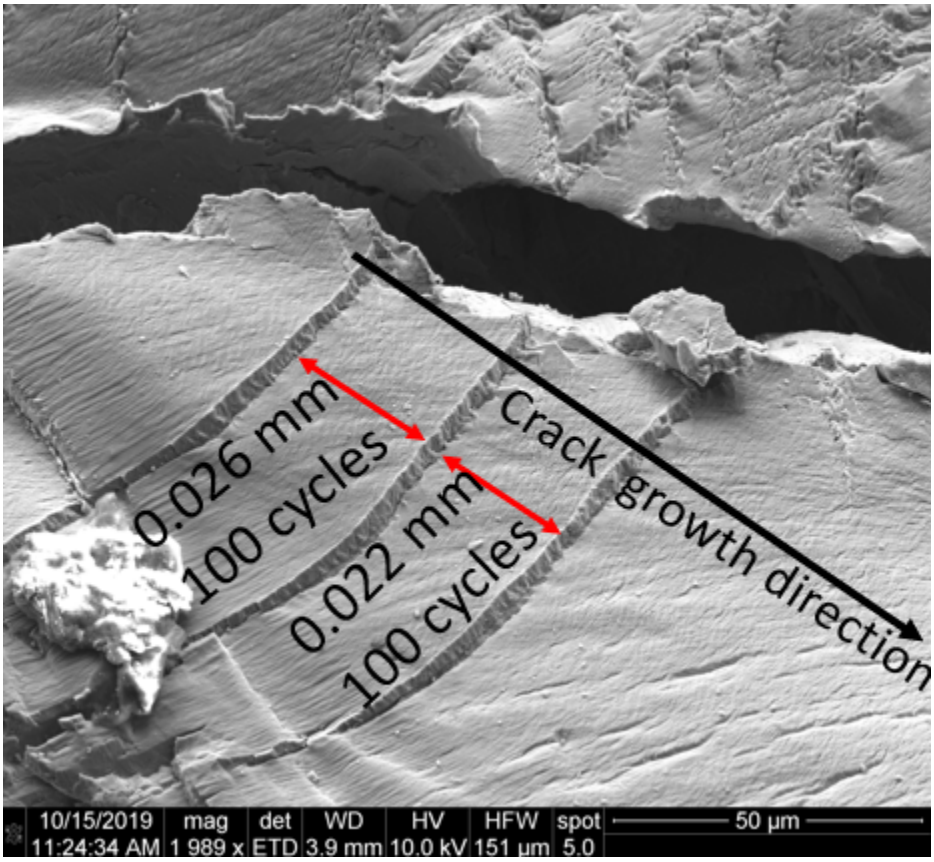

Figure 6.6. Marker band features

length of the fracture surface, ΔS known from the applied loads at Tables 5.2 and 5.3 and a representing the crack length measured from the crack initiation site.

$$\Delta K_1 = \frac{M_f \Delta S \sqrt{\pi a}}{\theta} \sqrt{sec(\frac{\pi a}{2t})} \tag{6.1}$$

As identified in the literature review, identifying MBs on the fracture surfaces of Titanium alloys is challenging. Fractography literature featuring other materials such as aluminum alloys are able to present an evaluation of crack length, a, against applied cycles, N, by counting each striation from crack initiation and matching them against the loading sequence. This method has been applied with success to both laboratory tests and in-service applications [52][53][63]. However, whilst the MB identification technique within this research was able to successfully detect MBs, striation or MB progression was not observed within these specimens. This was due to a number of factors. Firstly, the limited number

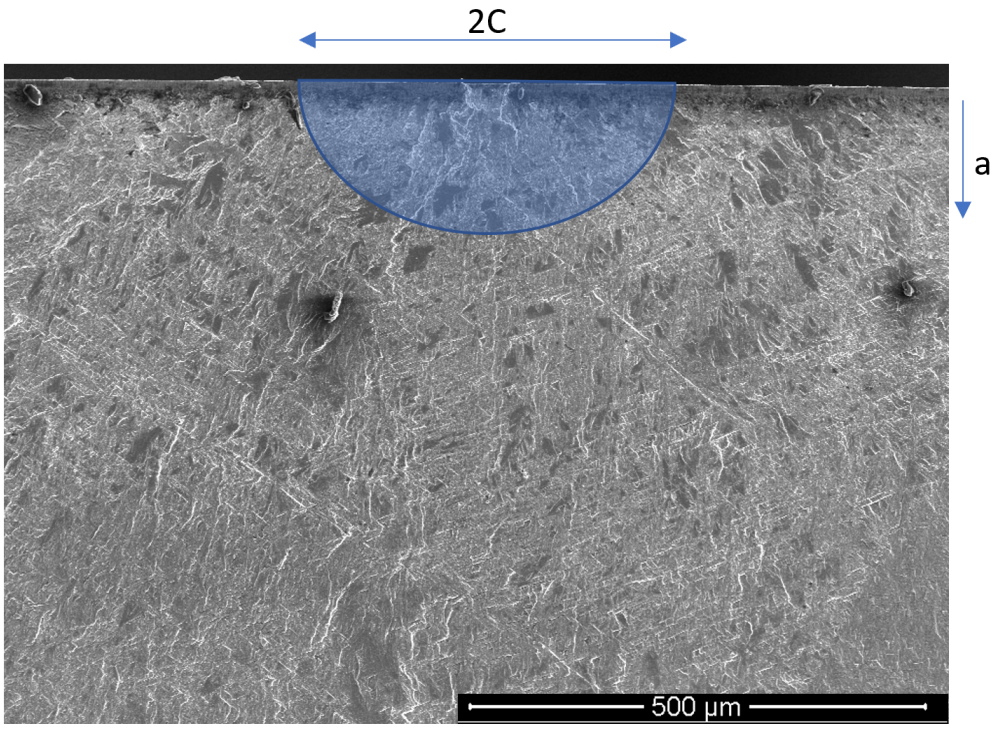

Figure 6.7. Surface semi-elliptical crack

of fatigue tests available for these specimens did not identify a reliable time when crack initiation occurred. The crack progression at figure 5.6 and the stress life plot at figure 5.7 illustrates this. Secondly, the crack initiation site for these specimens were difficult to locate [40]. Whilst the modification of the slot allowed for some success in initiating crack growth in the clad region, this did not always occur, as several specimens within research and previous research featured crack growth that did not originate at the notch or slot locations. Finally, the tortuous nature of the Ti-6Al-4V fracture surface creates difficulties in following MB progression throughout the fracture surface. This is best shown in figure 7.2, as the number of MBs detected decreases as the distance from the free surface increases.

6.4 Fractography Results

All identified MBs throughout the course of this research were plotted at figure 7.1, based on the stress concentration factor and da/dn methods previously discussed. These results are separated into the specimen categories of baseline substrate, As-clad or PHT. A

detailed definition of these specimen categories is detailed in chapter three. Additionally, the crack growth rate for a Mill-Annealed Plate of Ti-6AL-4V was taken from Metallic Materials Properties Development and Standardization (MMPDS) data used in previous research as a reference to these results. Results from previous research are shown as sample 9B to provide further context to the behavior of the [40].

Specimen 4A, an As-clad sample, failed at the slot. Observations with the optical microscope and SEM revealed a brittle failure within the clad region. Upon close inspection of the fracture surface in the SEM, crack initiation occurred close to the location of the middle notch, which was machined prior to the slot. With failure of the specimen identified at the notch area, searches quickly identified MBs within the clad region, on both fracture surfaces T and B. Identified MBs were faint and small, but detectable with the high zoom available on both SEM's. For this specimen, MBs were found within compressive residual stress region, but not within tensile region.

Specimen 3B, at PHT sample, also failed at the slot. Observations with the optical microscope and SEM revealed a brittle failure within the clad region. In a similar manner to specimen 4A, crack initiation occurred close to the location of the middle notch. With failure of the specimen identified at the notch area, searches quickly identified marker bands within the clad region, however marker bands were harder to detect on this sample compared to 4B, with less Marker Bands detected overall. Marker bands were faint and small, but still detectable within the SEM. Marker bands were found within both known tensile and compressive regions of residual stress.

Specimen 7B, a Baseline sample, failed at the slot as discussed in the fatigue chapter (figure 5.6). Observations with the optical microscope and SEM revealed a more ductile failure in comparison to the 4A and 3B samples. Upon close inspection of the fracture surface in the SEM, crack initiation occurred close to the location of the middle notch. A few good MBs were detected, with the MB from figure 6.5, the largest width MB observed in this research, originating from this sample. However, due to the tortuous nature of the fracture surface, it was very difficult to obtain a significant number of MBs, particularly when compared to the successful 4A and 3B samples. This may due to the greater number of cycles in the baseline testing sequence, as detailed in table 5.2, compared to the clad

sequence, shown in table 5.3. A greater number of cycles in this baseline sequence may create less opportunities to develop MBs on the part of the fracture surface that, based on the clad samples, contained the most MBs detected with the current equipment. Whilst there was no baseline sample residual stress data available for a comparison, as they were machined in a similar manner to the as-clad and PHT specimens, it is likely the baseline sample would be in compressive residual stress state.

Specimen 1A, a Baseline sample, experienced a more ductile failure in a similar manner to specimen 7B. The fracture surface on this sample was very tortuous, which made identification of MBs extremely difficult.

Finally, the fracture surface of the remaining specimens 2A, 5A, 8B and 9A were examined. Using the techniques detailed in this chapter, no MBs were discovered on these specimens. Whilst previous research indicated the higher cycle count of 9B may lead to a greater concentration of MBs on the fracture surface, this behavior was not observed within this research with a higher sample number. Samples with a more brittle and flat fracture surface were found to produce the most MBs, which was identified in previous research with the same specimens [40].

7. DISCUSSION

This research aimed to further the body of knowledge surrounding the influence of residual stress on the fatigue behavior of Ti-6Al-4V laser clad repairs. This was primarily achieved through analysis of the fracture surface of failed specimens, with detection of MBs allowing identification of material fatigue crack growth rate.

Slitting was demonstrated as an effective destructive residual stress method with a higher resolution available in the distance from the free surface, in comparison to the lower resolution provided by the contour method. The accuracy of this data played an important role in contextualizing the impact of residual stress on the fatigue crack growth rate characterized from MBs on the fracture surface. Due to post-deposition machining, the residual stress was higher in compression in the As-clad material in comparison with the PHT material.

The results of the HEXD non-destructive method showed the magnitude of lattice strain was higher for the As-clad material in comparison to PHT material, following the trend observed from the slitting method. The large degree of scatter present within both data sets is likely due to the large grain sizes reported in the material by previous research [40], making the application of this data within the context of residual stress problematic.

The success of identifying and tracking MBs within this research is shown in figure 7.1. Specimens 4A, 3B and 7B in particular show the success of the machined slot within design 3.2. This slot managed to produce MBs that featured crack initiation and propagation within the clad region. However, of the 7 specimens machined to design 3.2, only four featured distinctive MBs. These results show the challenge of producing distinctive MBs on a Ti-6Al-4V fracture surface that was encountered in previous research [40] and in literature [52].

The substrate material, with the exception of the 1A sample, appears to closely follow the behavior of the MMPDS Ti-6Al-4V material, providing a good baseline for this fractography method. A slight shift to the right of the MMPDS curve is likely due to the large grain size of the material [44], as reported in previous research [40]. Both of the laser clad repaired specimens, As-clad and PHT, feature a higher scatter and departure away from the MMPDS curve than the substrate material. A larger degree of scatter in these samples is

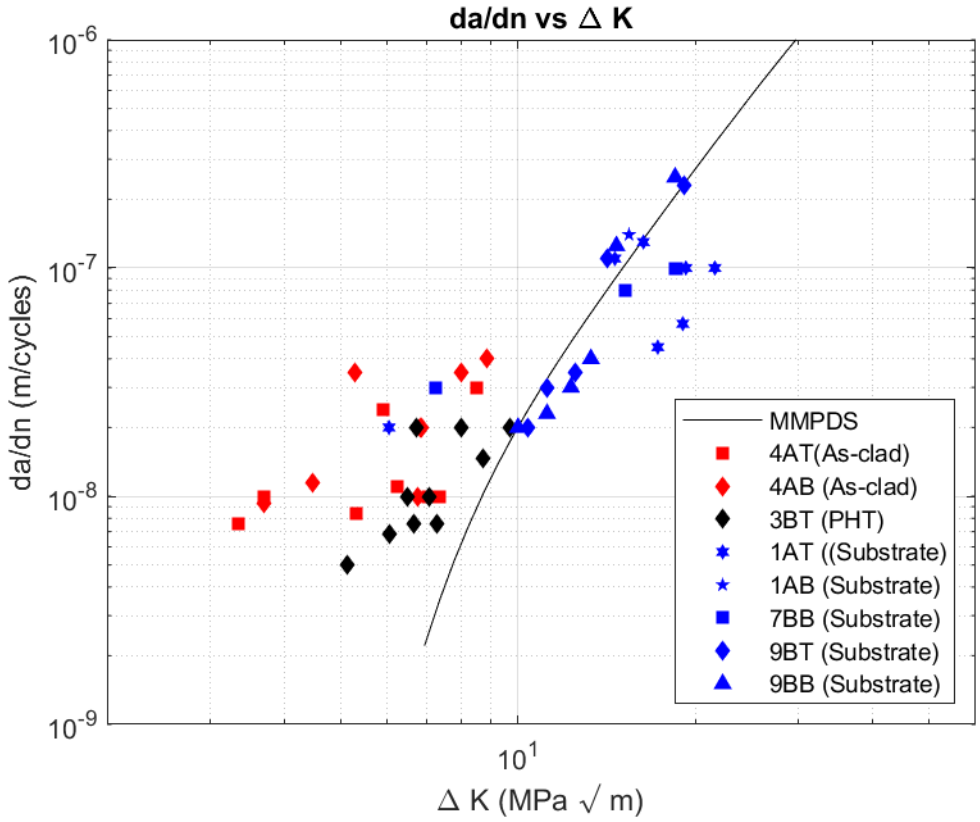

Figure 7.1. da/dN vs Δ K and MMPDS comparison

not unexpected, due to the variability in the AM process. However, this behavior in As-clad and PHT specimens can also be explained by the relatively short distances of the detected MBs from the free surface. The area on the fracture surface is typically dominated by short crack behavior, which features increased scatter than what is expected within region II of fatigue crack growth [43].

From these results it can be determined that both repair materials performed substantially worse than the substrate material. This outcome has significant implications for AM Ti-6Al-4V repairs of aircraft structure, as the performance of the repair suffers in comparison to the parent component material. Whilst AM repairs have the ability to restore a component back to a serviceable state, they may not enable it to fulfill its original design service life.

Whilst the 3B PHT specimen contained fewer identified MBs then the As-clad specimen 4A, it provided a more suitable candidate for a more detailed comparison as MBs were identified in both compression and tension residual stress states. MBs were only identified in the compression residual stress state in the As-clad specimen 4A. An outline of identified MBs on one of the 3B PHT fracture surfaces is shown in figure 7.2. The transition between compression and tension is highlighted, with the MBs identified by a sequential identification number. An asterisk denotes an interrupted MB, so the same MB that is lost among the fracture surface and regained. Despite knowing the crack initiation site due to the slot, the scarce number of MBs detected by the SEM highlights the challenges of MB detection discussed within the literature review.

The influence of residual stress on the crack growth rate of the simulated repair was next evaluated. The residual stress results from the slitting method outlined in chapter four were combined with the fractography results from figure 7.1. The accuracy in the slitting results were particularly useful in obtaining the residual stress transition point between compression and tension for both the As-clad and PHT specimens. As a baseline sample was not evaluated for residual stress using this technique, the baseline MBs were excluded from this figure and subsequent analysis. The remaining specimens are from one fracture surface of a PHT sample, and the two fracture surfaces from an As-clad sample. To isolate the influence of residual strength on this fractography data, the ΔK fractography data was adjusted to the effective threshold stress intensity value, $\Delta \mathrm{K}_{eff}$, utilizing the methods detailed in the literature review at section 2.3. The slitting data shown in figure 4.10 were utilized for σ_N^{RS}, with S_{min} and S_{max} corresponding to the minimum and maximum loads applied during the fatigue test, as detailed in Table 5.2. The outcome of this evaluation is plotted in figure 7.3, with a positive residual stress corresponding to tensile residual stress. The performance of the As-clad vs PHT repairs are still apparent in this figure, with a clear separation between the two specimen categories.

As stated in chapter 1, the aim of this research is to contextualize the effectiveness of laser cladding, based on the residual stress fields, underlying microstructure and spatial fatigue crack growth rates. Based on the observed behavior as seen in figure 7.3, this outcome presents the crack growth rate and subsequent damage tolerance of the As-clad repaired

material as significantly worse than the PHT material. Regarding the influence of residual stress, the slitting results detailed in chapter 4 of this research and the EDD results from previous research [40] have identified there is a notable, but not large, difference in residual stress between the As-clad and PHT specimens. This is particularly true within the laser clad region. If the slitting data is considered in isolation, the results of figure 7.1 appear to be counter-intuitive. The results in figure 7.3 indicate that an increased compressive residual stress leads to a higher crack growth rate (da/dN), which is the opposite of what would be expected, as detailed in section 2.3. One contributing factor to this behavior is small crack behavior. As all of the detected MBs are close to the free surface, a significant amount of variability would be expected. This behavior was also detected in the HEXD results, with the scatter observed in the HEXD lattice strain data at section 4.1.4. Additionally, due to the challenges in creating crack initiation in the clad region and MB detection. the data from figure 7.3 is only based on two failed specimens. A larger data set would provide greater clarity and enable more accurate observations on fatigue crack growth rate behavior of the laser clad repair.

In a similar manner, the influence of the changes in clad microstructure are expected to have a minimal impact to this damage tolerant behavior, as hardness testing conducted within this scope of work and previous research [40] did not identify a notable difference in hardness. Additionally, previous research identified negligible differences in grain size between the As-clad and PHT samples [40]. Any significant increases in grain size would shift the fractography results to the right in figures 7.1 and 7.3.

Notable differences between the clad repairs can also be accounted for by the implications of the residual stress influence on the crack closure mechanisms under fatigue loading. Within the region I dominant areas of fatigue crack growth in which MBs were detected, the As-clad fracture surfaces experienced compression whereas the PHT experienced tension close to the free surface before transitioning to compression. When considering the crack closure phenomenon, these two different residual stress states shift the amplitude of the applied fatigue loading, lengthening or decreasing the damaging portion of the loading cycle.

There implications of these results on the application of laser clad repairs on Ti-6Al-4V aircraft components is significant. Whilst the performance of the laser clad repair has

been demonstrated as worse than the baseline Ti-6Al-4V material, it is still available as a suitable repair method, provided the certification requirements are met. These certification requirements must be met to enable widespread application of these repairs on in-service aircraft, as detailed in chapter 1. Whilst this body of work presents material data that would assist in establishing a damage tolerance model, a significant amount of data is still required to enable any successful certification. A successful certification outcome would allow a laser clad repair application, with life limits and inspection thresholds lower than an un-repaired corresponding component due to the lower damage tolerance behaviour observed within this body of work.

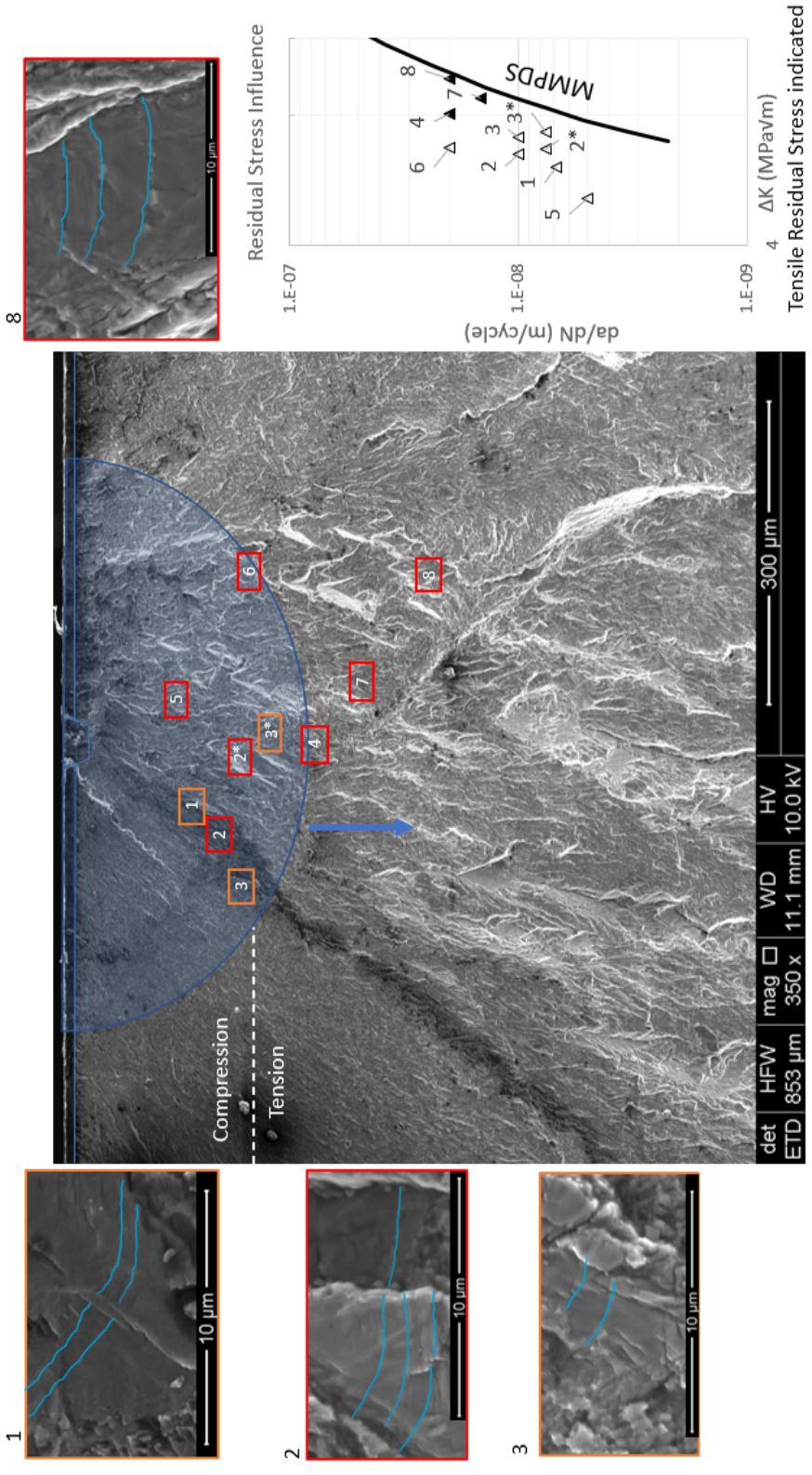

Figure 7.2. Residual stress and desired crack growth direction overlaid on the fracture surface

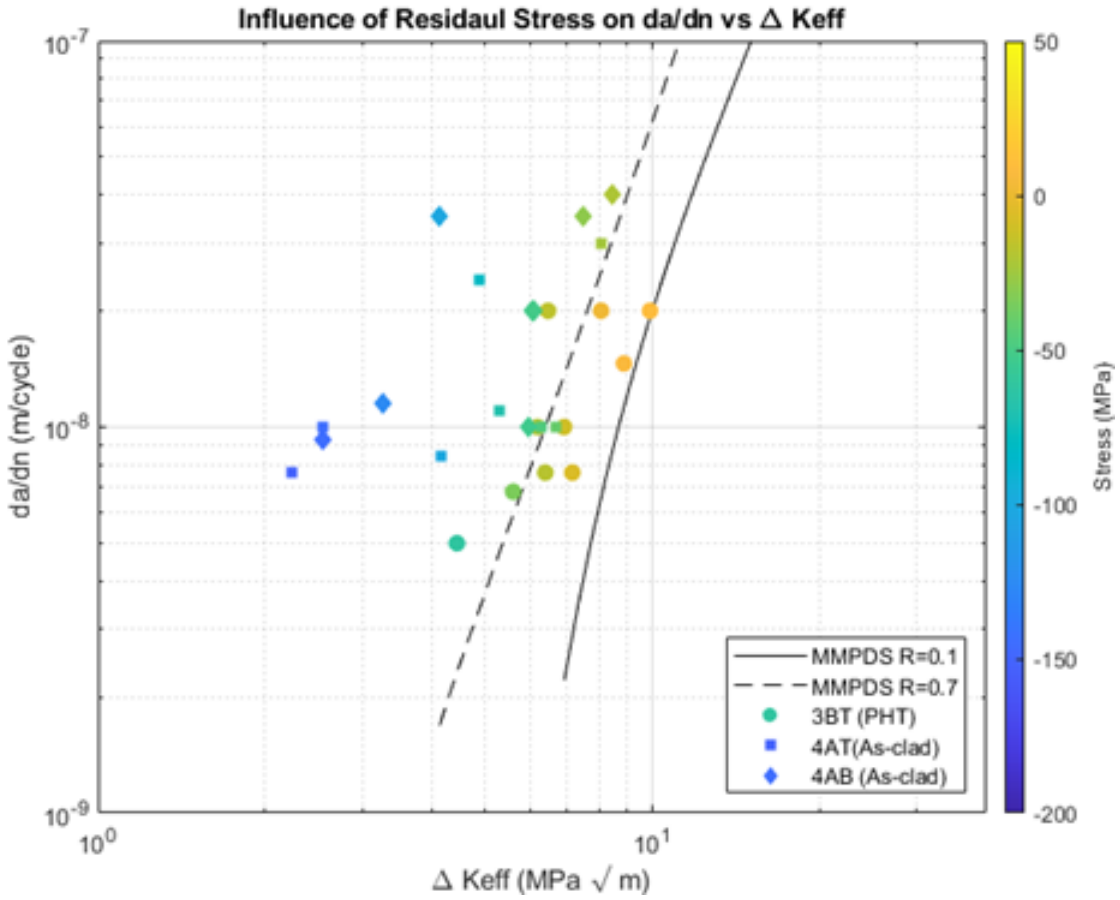

Figure 7.3. da/dN vs Δ Keff with residual stress

8. RECOMMENDATIONS

This body of work was able to improve on the techniques used for detecting and measuring MBs on a fracture surface. As discussed in chapter 7, more material data is required to assist in establishing a damage tolerance methodology for laser clad repaired materials. This principle reflects the requirements of stabilized material processes and characterized material properties of the Lincoln criteria [12]. Once these requirements are satisfied, further testing on a limited number of in-service components should be conducted to support certification efforts to accurately qualify the damage tolerance methodology against in-service loads and environmental factors.

The specimens used for fatigue evaluation of the laser clad repair were modified several times, both as part of this body of work and as part of previous research [40]. One of the recommendations from this previous research was for a re-design of the samples with a larger gauge area. The expectation would be that this change would create a more favorable fracture surface for uninterrupted MBs. This recommendation is further supported through the outcomes of this research, with only a few MBs detected within each sequential progression into the depth of the specimen. Additionally, the modification of the slit to replace the notches as a crack initiation site, as detailed in chapter 5, further decreased the path for MB progression.

The clad repair within these specimens was found to contain compressive residual stress. The presence of compressive residual stress within the clad region would be advantageous if it could be designed into a repair, and with effective testing for certification may actually extend the in-service life of the repair. However, post-processing may not be an option within the context of a military repair application. This can be due to corrosion prevention as some coatings may need to be retained on the assembly, or the geometry of the component may not allow post-deposition machining. Additionally, this methodology would not be possible for on-aircraft repairs.

Further work is needed in the progression of machine learning techniques to allow for automated quantitative fractography. The process of manual scanning of the fracture surface in the SEM is not effective for a large scale test sequence. To further improve the test data

for multiple material types, a large sample size is required to counter the scatter inherent in both the fatigue test and the varying properties of the laser clad repair. If a similar methodology is utilized within this research, it would take a significant period of time and may not be practical. The nature of AM research is fast, so an agile and fast methodology is required to rapidly characterize material properties. A greater predictability of structural performance allows for repairs to remain on aircraft for a longer period of time, increasing the capability of military aircraft.

REFERENCES

[1] T. A. P. D. Centre, *AAP 100-D The Air Power Manual*, 76. Canberra, 2013, ISBN: 9781920800901.

[2] U.S. Government Accountability Office, "Weapon System Sustainment: Aircraft Mission Capable Rates Generally Did Not Meet Goals and Cost of Sustaining Selected Weapon Systems Varied Widely," no. November, 2020. [Online]. Available: https://www.gao.gov/assets/720/710794.pdf.

[3] C. Crowley, "Meeting the Ageing Aircraft Challenge," no. October, 2004.

[4] K. Gager, "JUST DO IT … YOURSELF: Implementing 3D Printing in a Deployed Environment," *Wright Flyer*, vol. 66, p. 44, 2017.

[5] R. Cottam and M. Brandt, "Laser cladding of Ti-6Al-4V powder on Ti-6Al-4V substrate: Effect of laser cladding parameters on microstructure," *Physics Procedia*, vol. 12, no. PART 1, pp. 323–329, 2011, ISSN: 18753892. DOI: 10.1016/j.phpro.2011.03.041.

[6] D. L. Bourell and T. Wohlers, "ASM Handbook Volume 24: Additive Manufacturing," *Additive Manufacturing Processes*, vol. 24, pp. 3–10, 2020. DOI: 10.31399/asm.hb.v24.a0006555.

[7] A. Uriondo, M. Esperon-Miguez, and S. Perinpanayagam, "The present and future of additive manufacturing in the aerospace sector: A review of important aspects," *Proceedings of the Institution of Mechanical Engineers, Part G: Journal of Aerospace Engineering*, vol. 229, no. 11, pp. 2132–2147, 2015, ISSN: 20413025. DOI: 10.1177/0954410014568797.

[8] E. J. Liberman, "Additive Manufacturing (3D Printing) Aircraft Parts and Tooling at the Maintenance Group Level," no. March, 2015.

[9] R. Jones, N. Matthews, C. A. Rodopoulos, K. Cairns, and S. Pitt, "On the use of supersonic particle deposition to restore the structural integrity of damaged aircraft structures," *International Journal of Fatigue*, vol. 33, no. 9, pp. 1257–1267, 2011, ISSN: 01421123. DOI: 10.1016/j.ijfatigue.2011.03.013. [Online]. Available: http://dx.doi.org/10.1016/j.ijfatigue.2011.03.013.

[10] Y. R. Choi, S. D. Sun, Q. Liu, M. Brandt, and M. Qian, "Influence of deposition strategy on the microstructure and fatigue properties of laser metal deposited Ti-6Al-4V powder on Ti-6Al-4V substrate," *International Journal of Fatigue*, vol. 130, no. December 2018, 2020, ISSN: 01421123. DOI: 10.1016/j.ijfatigue.2019.105236.

[11] R. Green, "Additive Material Repairs The Changing Nautre of Sustainment," in *Aircraft Structural Integirty Symposium*, Melbourne, 2019.

[12] J. W. Lincoln, "Material and Process Technology Transition to Aging Aircraft," Aeronautical Systems Center, Wright Patterson Air Force Base, Tech. Rep., 2000.

[13] A. Grandt, *Fundamentals of Structural Integrity*. Hoboken, New Jersey: John WIley & Sons, 2004.

[14] S. Kundu, R. Jones, D. Peng, N. Matthews, A. Alankar, S. R. Raman, and P. Huang, "Review of requirements for the durability and damage tolerance certification of additively manufactured aircraft structural parts and AM repairs," *Materials*, vol. 13, no. 6, pp. 1–31, 2020, ISSN: 19961944. DOI: 10.3390/ma13061341.

[15] C. Babish, "Durability and Damage Tolerance Certification for Additive Manufacturing of Aircraft Structural Metallic Parts," Wright Patterson, Tech. Rep., 2019, pp. 1–8.

[16] G. Lutjering and J. Williams, *Titanium*. New York: Springer, 2003, pp. 3–41, ISBN: 9788578110796.

[17] M. J. Donachie, *Titanium A Technical Guide*. Ohio: ASM International, 2000, ISBN: 0871706865.

[18] X. Zhao, S. Li, M. Zhang, Y. Liu, T. B. Sercombe, S. Wang, Y. Hao, R. Yang, and L. E. Murr, "Comparison of the microstructures and mechanical properties of Ti-6Al-4V fabricated by selective laser melting and electron beam melting," *Materials and Design*, vol. 95, pp. 21–31, 2016, ISSN: 18734197. DOI: 10.1016/j.matdes.2015.12.135. [Online]. Available: http://dx.doi.org/10.1016/j.matdes.2015.12.135.

[19] T. Mishurova, S. Cabeza, K. Artzt, J. Haubrich, M. Klaus, C. Genzel, G. Requena, and G. Bruno, "An assessment of subsurface residual stress analysis in SLM Ti-6Al-4V," *Materials*, vol. 10, no. 4, 2017, ISSN: 19961944. DOI: 10.3390/ma10040348.

[20] M. Kasemer, R. Quey, and P. Dawson, "The influence of mechanical constraints introduced by β annealed microstructures on the yield strength and ductility of Ti-6Al-4V," *Journal of the Mechanics and Physics of Solids*, vol. 103, pp. 179–198, 2017, ISSN: 00225096. DOI: 10.1016/j.jmps.2017.03.013. [Online]. Available: http://dx.doi.org/10.1016/j.jmps.2017.03.013.

[21] B. Graf, A. Gumenyuk, and M. Rethmeier, "Laser Metal Deposition as Repair Technology for Stainless Steel and Titanium Alloys," *Physics Procedia*, vol. 39, pp. 376–381, 2012, ISSN: 18753892. DOI: 10.1016/j.phpro.2012.10.051. [Online]. Available: http://dx.doi.org/10.1016/j.phpro.2012.10.051.

[22] S. D. Sun, Q. Liu, M. Brandt, V. Luzin, R. Cottam, M. Janardhana, and G. Clark, "Effect of laser clad repair on the fatigue behaviour of ultra-high strength AISI 4340 steel," *Materials Science and Engineering A*, vol. 606, pp. 46–57, 2014, ISSN: 09215093. DOI: 10.1016/j.msea.2014.03.077. [Online]. Available: http://dx.doi.org/10.1016/j.msea.2014.03.077.

[23] N. Guo and M. C. Leu, "Additive manufacturing: Technology, applications and research needs," *Frontiers of Mechanical Engineering*, vol. 8, no. 3, pp. 215–243, 2013, ISSN: 20950233. DOI: 10.1007/s11465-013-0248-8.

[24] F. Weng, C. Chen, and H. Yu, "Research status of laser cladding on titanium and its alloys: A review," *Materials and Design*, vol. 58, pp. 412–425, 2014, ISSN: 18734197. DOI: 10.1016/j.matdes.2014.01.077. [Online]. Available: http://dx.doi.org/10.1016/j.matdes.2014.01.077.

[25] H. Paydas, A. Mertens, R. Carrus, J. Lecomte-Beckers, and J. Tchoufang Tchuindjang, "Laser cladding as repair technology for Ti-6Al-4V alloy: Influence of building strategy on microstructure and hardness," *Materials and Design*, vol. 85, pp. 497–510, 2015, ISSN: 18734197. DOI: 10.1016/j.matdes.2015.07.035. [Online]. Available: http://dx.doi.org/10.1016/j.matdes.2015.07.035.

[26] P. A. Kobryn and S. L. Semiatin, "Mechanical Properties of Laser-Deposited Ti-6Al-4V P.A. Kobryn and S.L. Semiatin Air Force Research Laboratory, AFRL/MLLMP, Wright-Patterson Air Force Base, OH 45433-7817," *International Solid Freeform Fabrication Symposium*, pp. 179–186, 2001.

[27] P. Kobryn and S. Semiatin, "Microstructure and texture evolution during solidification processing of Ti-6A1-4V," *Journal of Materials Processing Technology*, vol. 135, no. 2-3 SPEC. Pp. 330–339, 2003, ISSN: 09240136. DOI: 10.1016/S0924-0136(02)00865-8.

[28] K. F. Walker, J. M. Lourenço, S. Sun, M. Brandt, and C. H. Wang, "Quantitative fractography and modelling of fatigue crack propagation in high strength AerMet®100 steel repaired with a laser cladding process," *International Journal of Fatigue*, vol. 94, pp. 288–301, 2017, ISSN: 01421123. DOI: 10.1016/j.ijfatigue.2016.06.031. [Online]. Available: http://dx.doi.org/10.1016/j.ijfatigue.2016.06.031.

[29] G. S. Schajer, *Practical Residual Stress Measurement Methods*. 2013, pp. 1–310, ISBN: 9781118402832. DOI: 10.1002/9781118402832.

[30] P. J. Withers, M. Preuss, A. Steuwer, and J. W. Pang, "Methods for obtaining the strain-free lattice parameter when using diffraction to determine residual stress," *Journal of Applied Crystallography*, vol. 40, no. 5, pp. 891–904, 2007, ISSN: 00218898. DOI: 10.1107/S0021889807030269.

[31] W. Reimers, "Analysis of residual stress states using diffraction methods," *Acta Physica Polonica A*, vol. 96, no. 2, pp. 229–238, 1999, ISSN: 05874246. DOI: 10.12693/APhysPolA.96.229.

[32] R. Suganda, E. Sutrisno, and I. W. Wardana, *Residual Stress Measurement and the Slitting Method*, 9. 2013, vol. 53, pp. 1689–1699, ISBN: 9788578110796.

[33] W. Callister and D. Rethwisch, *Materials Science and Engineering - An Introduction*. 2010, ISBN: 9788578110796.

[34] K. Kapoor, P. Ravi, D. Naragani, J. S. Park, J. D. Almer, and M. D. Sangid, "Strain rate sensitivity, microstructure variations, and stress-assisted $\beta \rightarrow \alpha$ phase transformation investigation on the mechanical behavior of dual-phase titanium alloys," *Materials Characterization*, vol. 166, no. March, p. 110 410, 2020, ISSN: 10445803. DOI: 10.1016/j.matchar.2020.110410. [Online]. Available: https://doi.org/10.1016/j.matchar.2020.110410.

[35] J. M. Zhang, Y. Zhang, K. W. Xu, and V. Ji, "Anisotropic elasticity in hexagonal crystals," *Thin Solid Films*, vol. 515, no. 17, pp. 7020–7024, 2007, ISSN: 00406090. DOI: 10.1016/j.tsf.2007.01.045.

[36] M. B. Prime and P. Pagliaro, "Uncertainty, model error, and improving the accuracy of residual stress inverse solutions," *Proceedings of the 2006 SEM Annual Conference and Exposition on Experimental and Applied Mechanics 2006*, vol. 1, pp. 479–488, 2006.

[37] M. B. Prime, "Cross-sectional mapping of residual stresses by measuring the surface contour after a cut," *Journal of Engineering Materials and Technology, Transactions of the ASME*, vol. 123, no. 2, pp. 162–168, 2001, ISSN: 00944289. DOI: 10.1115/1.1345526.

[38] P. Rangaswamy, M. L. Griffith, M. B. Prime, T. M. Holden, R. B. Rogge, J. M. Edwards, and R. J. Sebring, "Residual stresses in LENS® components using neutron diffraction and contour method," *Materials Science and Engineering A*, vol. 399, no. 1-2, pp. 72–83, 2005, ISSN: 09215093. DOI: 10.1016/j.msea.2005.02.019.

[39] R. Bandyopadhyay, J. Rotella, D. Naragani, J. S. Park, M. Eff, and M. D. Sangid, "Residual Strain Analysis in Linear Friction Welds of Similar and Dissimilar Titanium Alloys Using Energy Dispersive X-ray Diffraction," *Metallurgical and Materials Transactions A: Physical Metallurgy and Materials Science*, vol. 50, no. 2, pp. 704–718, 2019, ISSN: 10735623. DOI: 10.1007/s11661-018-5034-0. [Online]. Available: https://doi.org/10.1007/s11661-018-5034-0.

[40] S. J. Noone, "Analysis of Laser Clad Repaired Ti-6Al-4V Fatigue Life," Ph.D. dissertation, Purdue, 2019.

[41] G. Totten, M. Howes, and T. Inoue, *Handbook of Residual Stress and Deformation of Steel - ASM International*. 2002, ISBN: 0871707292. [Online]. Available: https://www.asminternational.org/search/-/journal_content/56/10192/06700G/PUBLICATION.

[42] Y. F. Kudryavtsev, "Residual Stress," in *Springer handbook of experimental solid mechanics*, 2008, pp. 371–387, ISBN: 9780387268835.

[43] N. Dowling, *Mechanical Behaviour of Materials*. Harlow: Pearson Education Limited, 2013, ISBN: 9781626239777.

[44] R. Stephens, A. Fatemi, R. R. Stephens, and H. Fuchs, *Metal Fatigue in Engineering*, Second. John WIley & Sons, 2001, p. 452, ISBN: 0471510599.

[45] S. Leuders, M. Thöne, A. Riemer, T. Niendorf, T. Tröster, H. A. Richard, and H. J. Maier, "On the mechanical behaviour of titanium alloy TiAl6V4 manufactured by selective laser melting: Fatigue resistance and crack growth performance," *International Journal of Fatigue*, vol. 48, pp. 300–307, 2013, ISSN: 01421123. DOI: 10.1016/j.ijfatigue.2012.11.011. [Online]. Available: http://dx.doi.org/10.1016/j.ijfatigue.2012.11.011.

[46] M. D. Sangid, J. A. Stori, and P. M. Ferriera, "Process characterization of vibrostrengthening and application to fatigue enhancement of aluminum aerospace components-part II: Process visualization and modeling," *International Journal of Advanced Manufacturing Technology*, vol. 53, no. 5-8, pp. 561–575, 2011, ISSN: 02683768. DOI: 10.1007/s00170-010-2858-1.

[47] B. Vrancken, V. Cain, R. Knutsen, and J. Van Humbeeck, "Residual stress via the contour method in compact tension specimens produced via selective laser melting," *Scripta Materialia*, vol. 87, pp. 29–32, 2014, ISSN: 13596462. DOI: 10.1016/j.scriptamat.2014.05.016. [Online]. Available: http://dx.doi.org/10.1016/j.scriptamat.2014.05.016.

[48] P. Bendeich, N. Alam, M. Brandt, D. Carr, K. Short, R. Blevins, C. Curfs, O. Kirstein, G. Atkinson, T. Holden, and R. Rogge, "Residual stress measurements in laser clad repaired low pressure turbine blades for the power industry," *Materials Science and Engineering A*, vol. 437, no. 1, pp. 70–74, 2006, ISSN: 09215093. DOI: 10.1016/j.msea.2006.04.065.

[49] P. S. Song and C. C. Wen, "Crack closure and crack growth behaviour in shot peened fatigued specimen," *Engineering Fracture Mechanics*, vol. 63, no. 3, pp. 295–304, 1999, ISSN: 00137944. DOI: 10.1016/S0013-7944(99)00010-7.

[50] C. H. Wang, S. A. Barter, and Q. Liu, "A closure model to crack growth under large-scale yielding and through residual stress fields," *Journal of Engineering Materials and Technology, Transactions of the ASME*, vol. 125, no. 2, pp. 183–190, 2003, ISSN: 00944289. DOI: 10.1115/1.1493804.

[51] N. T. Goldsmith, R. J. Wanhill, and L. Molent, "Quantitative fractography of fatigue and an illustrative case study," *Engineering Failure Analysis*, vol. 96, no. October 2018, pp. 426–435, 2019, ISSN: 13506307. DOI: 10.1016/j.engfailanal.2018.10.013. [Online]. Available: https://doi.org/10.1016/j.engfailanal.2018.10.013.

[52] M. McDonald, R. Boykett, and M. Jones, "Quantitative fractography markers for determining fatigue crack growth rates in aluminium and titanium aircraft structures," *28th Congress of the International Council of the Aeronautical Sciences 2012, ICAS 2012*, vol. 6, pp. 4996–5005, 2012.

[53] S. A. Barter, L. Molent, and R. J. Wanhill, *Marker loads for quantitative fractography of fatigue cracks in aerospace alloys*, 2009. DOI: 10.1007/978-90-481-2746-7{_}2.

[54] W. Hu, A. Wiliem, B. Lovell, S. Barter, and L. Liu, "Automation of Quantitative Fractography for Determination of Fatigue Crack Growth Rates with Marker Loads," *29th ICAF Symposium – Nagoya*, no. June, pp. 7–9, 2017.

[55] I. Konovalenko, P. Maruschak, and O. Prentkovskis, "Automated method for fractographic analysis of shape and size of dimples on fracture surface of high-strength titanium alloys," *Metals*, vol. 8, no. 3, 2018, ISSN: 20754701. DOI: 10.3390/met8030161.

[56] M. Waddell, K. Walker, R. Bandyopadhyay, K. Kapoor, A. Mallory, X. Xiao, A. C. Chuang, Q. Liu, N. Phan, and M. D. Sangid, "Small fatigue crack growth behavior of Ti-6Al-4V produced via selective laser melting: In situ characterization of a 3D crack tip interactions with defects," *International Journal of Fatigue*, vol. 137, no. January, p. 105 638, 2020, ISSN: 01421123. DOI: 10.1016/j.ijfatigue.2020.105638. [Online]. Available: https://doi.org/10.1016/j.ijfatigue.2020.105638.

[57] M. D. Sangid, T. A. Book, D. Naragani, J. Rotella, P. Ravi, A. Finch, P. Kenesei, J. S. Park, H. Sharma, J. Almer, and X. Xiao, "Role of heat treatment and build orientation in the microstructure sensitive deformation characteristics of IN718 produced via SLM additive manufacturing," *Additive Manufacturing*, vol. 22, no. January, pp. 479–496, 2018, ISSN: 22148604. DOI: 10.1016/j.addma.2018.04.032. [Online]. Available: https://doi.org/10.1016/j.addma.2018.04.032.

[58] K. Kapoor, P. Ravi, R. Noraas, J.-s. Park, V. Venkatesh, and M. D. Sangid, "Modeling Ti-6al-4V using crystal plasticity to understand the effect of orientation and morphology of the α and β phases on time dependent cyclic loading," *Journal of the Mechanics and Physics of Solids*, vol. 146, no. October 2020, p. 104 192, 2021, ISSN: 0022-5096. DOI: 10.1016/j.jmps.2020.104192. [Online]. Available: https://doi.org/10.1016/j.jmps.2020.104192.

[59] B. Cullity, *Elements of X-Ray Diffraction*, 3. Addison-Wesley, 1978, pp. 110–120, ISBN: 0201011743.

[60] M. Prime, *Residual stress measurement by successive extension of a slot: A literature review*, 1997. [Online]. Available: http://www.osti.gov/servlets/purl/481857-lyCpSD/webviewable/.

[61] ASTM, "Standard practices for verification of testing frame and specimen alignment under tensile and compressive axial force application," Tech. Rep., 2013, pp. 1–18.

[62] C. A. Zapffe, L. Ercker, L. Savot, M. Jousse, T. Iii, and T. Vifracture, "ASM Handbook Volume 12: Fractography," *Fractography*, vol. 12, no. Ref 6, pp. 1–11, 2018. DOI: 10.31399/asm.hb.v12.a0001830.

[63] B. Main, L. Molent, R. Singh, and S. Barter, "Fatigue crack growth lessons from thirty-five years of the Royal Australian Air Force F/A-18 A/B Hornet Aircraft Structural Integrity Program," *International Journal of Fatigue*, vol. 133, no. December 2019, p. 105 426, 2020, ISSN: 01421123. DOI: 10.1016/j.ijfatigue.2019.105426. [Online]. Available: https://doi.org/10.1016/j.ijfatigue.2019.105426.